DOKUZ EYLÜL UNIVERSITY
GRADUATE SCHOOL OF NATURAL AND APPLIED SCIENCES

EFFECTS OF AN INTENSE LASER FIELD ON THE INTERSUBBAND TRANSITIONS AND IMPURITY BINDING ENERGY IN QUANTUM DOTS

by
Dilara GÜL KILIÇ

January, 2021
İZMİR

EFFECTS OF AN INTENSE LASER FIELD ON THE INTERSUBBAND TRANSITIONS AND IMPURITY BINDING ENERGY IN QUANTUM DOTS

A Thesis Submitted to the
Graduate School of Natural And Applied Sciences of Dokuz Eylül University
In Partial Fulfillment of the Requirements for the Degree of Doctor of Philosophy in Physics

by

Dilara GÜL KILIÇ

January, 2021
İZMİR

Ph.D. THESIS EXAMINATION RESULT FORM

We have read the thesis entitled "**EFFECTS OF AN INTENSE LASER FIELD ON THE INTERSUBBAND TRANSITIONS AND IMPURITY BINDING ENERGY IN QUANTUM DOTS**" completed by **DİLARA GÜL KILIÇ** under supervision of **PROF. DR. SERPİL ŞAKİROĞLU** and we certify that in our opinion it is fully adequate, in scope and in quality, as a thesis for the degree of Doctor of Philosophy.

....

Prof. Dr. Serpil ŞAKİROĞLU

Supervisor

....

Prof. Dr. İsmail SÖKMEN

Thesis Committee Member

....

Assoc.Prof Dr. Emine Mine ÇAPAR

Thesis Committee Member

....

Prof. Dr. Esin KASAPOĞLU

Examining Committee Member

....

Assoc.Prof Dr. Görkem OYLUMLUOĞLU

Examining Committee Member

Prof. Dr. Özgür ÖZÇELİK
Director
Graduate School of Natural and Applied Sciences

ACKNOWLEDGEMENTS

I would like to thank the following people, my PhD works would not have been possible without their supports.

Foremost, I would like to express my sincere gratitude to my supervisor Prof.Dr. Serpil ŞAKİROĞLU due to her dedicated support, guidance and scientific contribution during my thesis. Her dynamism, vision, sincerity and motivation have provided the inspiration for my academic education. She has always encouraged to my scientific works and has always been with me. I always knew that she believed in me and wanted the best for me. It is a great privilege and honor to be her PhD student.

I would like to say a special thank you to Prof. Dr. İsmail SÖKMEN for his support, insightful comments and scientific contribution. His knowledge and experience in semiconductor and computational physics enlighten for my scientific carrier. This work would not been possible without his assistance and support.

I am indebted to Prof. Dr. Doğan DEMİRHAN whom I modeled as a scientist for his support and scientific contribution. His guidance helped me in all the time for improving myself scientifically.

And also, I sincerely appreciate Doç. Dr. Emine Mine ÇAPAR, who is my thesis committee member, for valuable recommendations and contributions.

Finally, I am extremely grateful to my loving family because of showing a great amount of support and patience. Without their love, constant encouragement and endless support this thesis would not have been possible. My sincere thanks also goes to Mustafa KILIÇ who is my husband. I have always felt his belief and supporting to complete this research work.

This thesis is dedicated to my honey nephews, Bahar GÜL and Defne GÜL.

Dilara GÜL KILIÇ

EFFECTS OF AN INTENSE LASER FIELD ON THE INTERSUBBAND TRANSITIONS AND IMPURITY BINDING ENERGY IN QUANTUM DOTS

ABSTRACT

In this thesis, we focus on the effects of non-resonant, high-frequency intense laser field (ILF) on the optical response of a two-dimensional quantum dot including on-center impurity under uniform magnetic field. THz laser radiation with circular polarization has been treated within the framework of high-frequency Floquet approach. The effects of impurity types modeled by using different potentials such as Gaussian, Hydrogenic and screened Coulomb on the system are investigated. Besides, we have also examined the influence of ILF on the optical properties of a two-dimensional quantum ring described by the parabolic confinement potential and the Gaussian peak localized to the center.

Based on the compact-density matrix approach and iterative procedure, linear and third-order nonlinear optical absorption coefficients and refractive index changes and third-harmonic generation coefficient are calculated. The energy eigenvalues and wave functions of defined systems have been obtained numerically by using finite element method in one dimension which is based on Galerkin approach.

The obtained results show that the action of ILF leads to crucial changes in the electronic structure of quantum dot (ring), the impurity binding energy and consequently the behavior of optical properties. Further, the position and magnitude of the resonant peak of optical characteristics are significantly affected by magnetic field, quantum dot (ring) size, the impurity potential parameters and the system parameters.

Keywords: Quantum dot, THz laser field, impurity, optical properties, finite element method

YOĞUN LAZER ALANININ KUANTUM NOKTALARINDA ALTBANTLARARASI GEÇİŞLERE VE SAFSIZLIK BAĞLANMA ENERJİSİNE ETKİLERİ

ÖZ

Bu tezde, rezonant olmayan, yüksek frekanslı, yoğun lazer alanının (ILF), düzgün manyetik alan altında merkezi safsızlık içeren iki-boyutlu bir kuantum noktanın optik yanıtı üzerindeki etkilerine odaklandık. Dairesel polarizasyonlu THz lazer radyasyonu, yüksek-frekanslı Floquet yaklaşımı çerçevesinde ele alınmıştır. Gaussian, Hidrojenik ve screened Coulomb gibi farklı potansiyeller kullanılarak modellenen safsızlığın sistem üzerine etkileri incelenmiştir. Ayrıca, ILF'nin parabolik hapsetme potansiyeli ve merkezine lokalize Gaussian pik ile tanımlanan iki-boyutlu bir kuantum halkasının optik özellikleri üzerindeki etkisini de inceledik.

Kompakt-yoğunluk matrisi yaklaşımı ve iteratif yönteme dayanarak, lineer ve üçüncü-derece lineer olmayan optik soğurma katsayıları ve kırılma indisi değişimi ve üçüncü-harmonik üretimi katsayısı hesaplanmıştır. Galerkin yaklaşımına dayanan tek boyutta sonlu elemanlar yöntemi kullanılarak tanımlanan sistemlerin enerji özdeğerleri ve dalga fonksiyonları nümerik olarak elde edilmiştir.

Elde edilen sonuçlar, ILF uygulamasının kuantum noktanın (halkanın) elektronik yapısında, safsızlık bağlanma enerjisinde ve dolayısıyla optik özelliklerin davranışında önemli değişikliklere yol açtığını göstermektedir. Ayrıca, optik karakteristiklerin rezonant pik noktasının konumu ve büyüklüğü, manyetik alan, kuantum nokta (halka) boyutu, safsızlık potansiyel parametreleri ve sistem parametrelerinden önemli ölçüde etkilenmektedir.

Anahtar kelimeler : Kuantum nokta, THz lazer alanı, safsızlık, optik özellikler, sonlu elemanlar metodu

CONTENTS

Page

LIST OF FIGURES

CHAPTER ONE

INTRODUCTION

Advances in nanotechnology over the last decade has made it possible to fabricate low-dimensional structures with nanometer scale such as quantum well (QW), quantum wire (QWR) and quantum dot (QD) (Harrison, 2005; Knoss, 2009). The strong confinement in low-dimensional structures compared with bulk structures gives rise to intensive researches in analysing the electronic, magnetic and optical properties of these systems, both experimentally and theoretically (Chakraborty, 1999; Ganguly et al., 2017; Jacak et al., 1998; Knoss, 2009).

Among all low-dimensional structures, quantum dots are focus of special and increasing attention due to their broad potential applications in different fields. Quantum dots are structures created by the limitation of electrons to a small spatial region in three dimensions and are also called "*artificial atoms*" (Banyai & Koch, 1993; Borovitskaya & Shur, 2002; Knoss, 2009; Kouwenhoven et al., 2001; Reed et al., 1986). QDs can be achieved both two- and three-dimensions (Li et al., 2008; Lu & Xie, 2011; Mukhopadhyay & Chatterjee, 1998; Reed et al., 1988) and they are likely to be fabricated with different shapes such as spherical, cylindrical, ellipsoidal, lens shape and parabolic cylinder on account of controllable size, shape and composition (Li et al., 2016; Prasad & Silotia, 2011; Solaimani, 2020). These structures demonstrates interesting electric and optical properties due to their quantum confinement effects. As a consequence, special interest has been depicted to studies of QDs with the effects of impurity (Baskoutas et al., 2007; Bose, 1998; Chen, 2011; Ferreyra et al., 1997), anisotropy (Madhav & Chakraborty, 1994; Soltani-Vala & Barvestani, 2017), electron-phonon interaction (Khordad, 2017), external fields (Bejan, 2016a; Terzis & Baskoutas, 2005; Yuan et al., 2014) and magnetopolaron (Charrour et al., 2000; Kandemir & Cetin, 2002) on the electronic and optical properties. Similar to QDs, quantum rings (QRs) are nanostructures in which the confinement of electrons is in all spatial dimensions (Fomin, 2018; Fuhrer et al., 2001). In QRs, the discreteness of energy and charge emerges as well atomic systems because both the diameter and the ring width can be altered (Radu et al., 2014). Due to the fact that QRs exhibit the intriguing of the physical phenomena such as persistent currents and Aharonov-Bohm effect (Aharonov & Bohm, 1959; Liao & Xie, 2015; Triki et al., 2010; Yun et al., 2015), a great deal of theoretical and experimental work has been devoted (Acosta et al., 2016; Jin et al., 2013; Räsänen & Aichinger, 2009; Vinasco et al., 2019).

In addition, another topic studied intensively in QDs/QRs has become the investigation of linear and nonlinear optical properties. Controllability and tunability of the optical properties of QDs/QRs is significant for the fundamental scientific point of view due to their applications in optoelectronic devices such as high-speed electro-optical modulators, THz detectors, solar cells, semiconductor optical amplifiers and memory devices. For this reason, a great number of studies have been broadcasted to examine the optical properties of QDs/QRs in literature (Duque et al., 2013; Sakiroglu et al., 2017; Wang, 2015; Shao et al., 2011; Zeng et al., 2014). For example, Liu et al. have performed the theoretical investigation of linear and nonlinear optical absorption in a disk-shaped QD (Liu et al., 2012). The third-harmonic generation in cylindrical QDs with an applied electric field has been carried out by Shao et al. (Shao et al., 2010). Khordad and Bahramiyan have reported the influence of electron-phonon interaction on the second and third-harmonic generation in modified Gaussian QDs (Khordad & Bahramiyan, 2014). Kasapoglu et al. have presented the effects of electric and intense laser fields on the nonlinear optical properties of a cylindrical QD (Kasapoglu et al., 2015). The effects of shape on the refractive index changes by introduce a QD with a symmetry confining potential has been studied by Li et al. (Li et al., 2016). Very recently, the electron-related nonlinear optical properties of cylindrical QD with the Rose-Morse axial potential in the presence of ILF has been studied by Ungan et al. (Ungan et al., 2020)

Furthermore, studying the impurity effects in QDs is one of the most important subjects in semiconductor physics because of applications in optoelectronic devices. Thus, a large number of studies involving impurity, usually modeled by Gaussian, Coulomb and screened Coulomb potentials, have been broadcasted (Barseghyan, 2015; Vahdani & Rezaei, 2009; Varshni, 2001a). These studies show that the presence of impurity brings about obvious changes in the electronic, optical and transport properties of systems and enables to control them (Bera et al., 2016; Chen et al., 2013; Huang, 2013; Mikhail & Shafee, 2017; Sarkar et al., 2016; Xie, 2009). Consequently, it is significant to figure out deeply the effects of impurities on the semiconductor nanostructures because the presence of impurity is able to affect significantly the performance of optoelectronic devices. The pioneering work about the binding energy of the on-center donor hydrogenic impurity in spherical GaAs-(Ga,Al)As QDs has been performed by Porras-Montenegro and Perez-Merchancano (Porras-Montenegro & Perez-Merchancano, 1992). Räsänen et al. have researched the influence of impurity in a QD in GaAs/AlGaAs resonant tunneling device (Räsänen et al., 2004). The works of Halonen and his co-workers have denoted the effects of a repulsive scattering centers on the energy spectrum and optical-absorption spectra of quantum dots (Halonen et al., 1996a,b). The study of behaviors of the binding energy of cylindrical QD with the presence of a uniform electric field has been achieved by Hong et al. (Pan et al., 2011). The results have shown that the impurity potential has the effect of breaking circular symmetry and this also leads to level repulsions, lifting of degeneracy, etc. Datta et al. have researched in detailed the pattern of time evolution of eigenstates and excitation profile of a repulsive impurity doped quantum dot (Datta et al., 2010; Datta & Ghosh, 2011). The optical rectification, Aharonov-Bohm oscillation of Raman scattering and photoionization cross section in QDs and QRs with a repulsive scattering center have been extensively studied in the studies of Xie (Xie, 2013a,b, 2014).

Besides, the improvement of high-power tunable laser sources has led to the discovery of intriguing physical phenomena relevant to the intense laser field (ILF) (Brandi et al., 2001; Enders et al., 2004; Gavrila, 1992; Räsänen et al., 2007; Xu et al., 2009). Therefore, the interaction of carriers with electromagnetic radiation in QDs has become an attractive research topic among researchers (Burileanu, 2014; Laroze et al., 2016; Prasad & Silotia, 2011; Spandonide et al., 2016). For instance, the influence of ILF on the the binding energy of an on-center hydrogenic impurity of spherical QDs has been studied in detail the work of Varshni (Varshni, 2001b) A detailed investigation of the donor impurity-related energy levels and Electronic Raman Scattering in a disc-like QD with the presence of ILF has been carried out by Lu et al (Lu et al., 2011). Mora-Ramos et al. have investigated the laser dressing effects on the exciton states in GaAs-$Ga_{1-x}Al_xAs$ QDs (Mora-Ramos et al., 2012b). The effects of intense laser and static electric fields on the impurity-related electromagnetically induced transparency in a GaAs disk-like QD have been given in the report of Niculescu (Niculescu, 2017). More recently, Sari and and co-workers have examined the impurity related electron energy spectrum and intersubband optical absorption in 2D laser-driven QD (Sari et al., 2020). Investigations exhibit that the energy levels, potential profile and optical properties of QDs can be altered by tuning the strength of the THz laser radiation.

Although, to the best of our knowledge, several works have demonstrated noticeable interest to research the effects of linearly polarized laser radiation on the impurity-related QD systems, the effect of circularly THz laser field on the electronic structures and optical properties of 2DQD (QR) systems in the presence different impurity has not been investigated so far. That's why, the aim of this thesis is to investigate the effects of circularly polarized ILF on the impurity-related energy levels and optical characteristics for such systems. Firstly, we examine the influence of an on-center Gaussian impurity on the optical response and electronic structure of laser-driven parabolic QD system under uniform magnetic field. We have also explored the optical properties of a laser-driven disc-shaped QD with hydrogenic and screened Coulomb impurity. Besides, we have analyzed the effect of THz laser radiation on the linear and nonlinear optical properties of 2DQR consisting of parabolic potential with center-localized Gaussian peak subjected to external uniform magnetic field. The results of this work are presented in References (Kilic et al., 2018, 2019, 2020; Sakiroglu et al., 2018).

The organization of the present Thesis is as follows: In Chapter 2, a brief overview of QDs and their applications given. Chapter 3 introduces the theoretical background constituting the fundamental of thesis. The general formalism used in this work is presented in Chapter 4. The numerical results of examined systems are analyzed exhaustively in Chapter 5 and finally, the main findings of this Thesis are emphasized in Chapter 6.

CHAPTER TWO
QUANTUM DOTS

2.1 Overview of Quantum Dots

Research advances in the nanofabrication technologies has enabled to fabricate various kinds of low-dimensional quantum structures. In early 1970s, the experimental works on the first low-dimensional quantum structure known as Quantum Wells (QWs) have been achieved by Dingle et al. (Dingle et al., 1974). Such structures are often referred as two dimensional (2D), because the charge carriers (electrons and holes) are confined in a 2D plane. Thanks to the advancements of 2D systems, the possibility of reducing the dimensionality further to create one dimensional-Quantum Wire (QWR) and zero-dimensional Quantum Dot (QD) structures have been intensively investigated by researchers (Harrison, 2005; Knoss, 2009). Schematic drawing of confinement in zero, one, two, and three dimensions is shown as Figure 2.1 (Edvinsson, 2018).

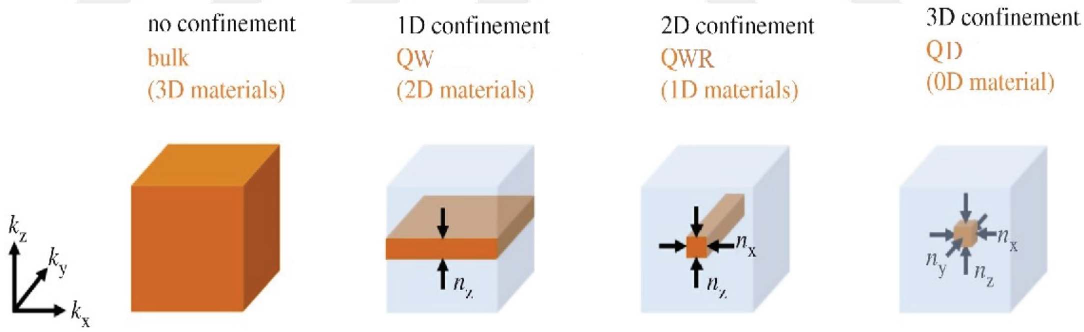

Figure 2.1 The schematic illustration for quantum structures; bulk material, quantum well, quantum wire, quantum dot

Among low-dimensional structures, QDs in which the movement of electrons is confined in all three spatial dimensions have remarkable interest due to the unique electronic and optical properties. In general, QDs are known as artificial atoms owing to the analogies to real atoms. The energy levels of QDs are quantized on account of the confinement of electrons like as an atom and the size of QDs is in the range of 1-100 nanometers (Chakraborty, 1999; Jacak et al., 1998). Improvement in growth techniques have led to the intensive empirical investigation of QDs (Cibert et al., 1986; Reed et al., 1988; Temkin et al., 1987). One of the first reports has been carried out by Ekimov and Onushchenko (Ekimov & Onushchenko, 1981). They have observed the size effects on the three-dimensional microscopic CuCl crystals grown in a transparent dielectric matrix. A few years later, Reed et al. have obtained total spatial quantization in GaAs-AIGaAs multiple QDs by a fabrication-imposed potential (Reed et al., 1986).

So as to obtain the QD structures, the two main types of fabrication techniques namely lithographic and epitaxial growth techniques can be used and listed as follows:

- *Lithographic Techniques:* Lithography is one of the main techniques in micro- and nano-fabrication technology. This technique provides the creation of sensitive and complex two-dimensional or three-dimensional structures at enormously small scales. The technique arose from a method of planographic printing on smooth surfaces of a plate or stone (Tran & Nguyen, 2017). X-ray lithography, Holographic lithography, electron beam lithography and scanning tunnelling microscope lithography are generally used lithography techniques.
- *Epitaxial Growth Techniques:* Epitaxy growth refers to the growth of a crystalline film on a substrate lattice. Epitaxy technique enables to control the high level of growth parameters due to the uniformity in the composition. (Kajdos & Stemmer, 2015; Shinoj, 2016). There are several epitaxial techniques: Molecular beam epitaxy, chemical beam epitaxy, atomic layer epitaxy and metal-organic chemical vapour deposition.

2.2 Applications of Quantum Dots in Technology

Quantum dots, which are small devices, have important technological applications due to their adjustable and controllable dimensions. Because of the unique optical and electrical properties, these structures are extensively used the different applications such as optoelectronic devices, quantum computing, biological applications, memory devices Zhang et al. (2009). We can summarize these applications as follows:

- *Optoelectronic Devices:* Optoelectronics is a specific discipline of electronics that interact with light and their application to practice. Optoelectronics is based on the quantum mechanical effects of light on electronic materials, especially semiconductors (Adams & Barbante, 2015). QDs can be implemented to a large variety of optoelectronic devices. QD solar cells, QD-lasers, QD-LED, biomarker assays, field effect transistors, LEDs and QD infrared photodetectors are only some examples.

- *Quantum Computing:* One of the important application of QDs is quantum computer (D'Amico, 2006; Imamoglu, 2003; Loss & DiVincenzo, 1998). The quantum computer is able to perform high-speed mathematical and logical operations. Furthermore, quantum information following the laws of quantum mechanics can be stored and processed (Shi et al., 2015). Unlike a classical computer, the quantum computer permits new types of information processing and solve specific problems far faster (Stern, 2000).

- *Biotechnological Applications:* Because of their photophysical properties, the QDs have replaced the traditional organic dyes (Peng & Li, 2010). When the QDs interact with light, they emit different colors according to their size. Therefore, they are used for cell targeting (Nifontova et al., 2019), embryonic stem cells (Lin et al., 2007), cancer diagnosis and cancer therapy (Chowdhury et al., 2018). Progressive researches and developments on QDs will continue to open up opportunities for using in biotechnological applications (Abbasi et al., 2016).

- *Memory Devices:* The QD structures play an important role in microelectronics and memory storage devices. High-performance and high-density memories are achieved by using QDs (Dimitrakis et al., 2013; Ishikawa, 1999). Self-organized QDs are particularly interesting because they provide a number of interesting advantages for the next generation of memories (D'Amico, 2006; Damodaran & Ghosh, 2016; Imamoglu, 2003). A memory based on self-organized QD has the advantages of a fast write speed and a long storage time (Bimberg et al., 1999; Nowozin et al., 2013). In addition, spintronics devices using magnetic QDs have become a very rapidly expanding area (Ghosh & Frota, 2013). Spintronics refers to the use of intrinsic spin of the electrons and its associated magnetic moment in devices, in addition to fundamental electronic charge (Fert, 2008). Spintronics devices will continue to present a bright future for applications such as switching, amplification, non-volatile memory storage, spin-field effect transistor and memory chips (Bhatti et al., 2017; Hirohata et al., 2020).

2.3 Impurity in Quantum Dots

Impurity effects in semiconductor QDs is one of the notable topic, which have fascinated great attention in recent years. QDs can be doped with different types and concentrations of impurities to dramatically vary its physical, thermal, electrical and optical properties (Ferreyra et al., 1997; Karabulut & Baskoutas, 2008; Porras-Montenegro & Perez-Merchancano, 1992). Therefore, it could be important the understanding of effects of impurity for optimizing the semiconductor device applications. The inclusion of an impurity in the semiconductor crystal corresponds to the effective addition of a charge carrier and a charged impurity ion to the system. The impurities included will lead to localized states in the forbidden energy gap (Holtz & Zhao, 2004). After Bastards pioneering work on the donor impurity in a semiconductor quantum well (Bastard, 1981), the study of impurities in semiconductor QDs has attracted much attention by researchers. An understanding of the electronic and optical properties of such systems, which are strongly affected by the presence of impurities, is important for the design of optoelectronic devices (Baskoutas et al., 2007; Liang et al., 2011; Saha & Ghosh, 2015). Therefore, many works have been devoted to the understanding of impurity effects on the electronic structure and optical properties of QDs using different confinement potentials (Datta et al., 2010; Rezaei et al., 2011; Xie, 2009). Generally three models are used for describing of impurity potential in nanostructures:

- *Hydrogenic Impurity:* Hydrogen-like impurity is described by Coulomb potential and this potential has a singularity at $|\mathbf{r}| \rightarrow 0$ because of the form it has (Kshevetsky & Shapilov, 2017). Due to the geometry confinement of QDs and impurity induced Coulomb potential, in general, the analytical calculation of the eigenstates is complicated or even insoluble. This is why one often adopts some approximate methods such as the variational method and the diagonalization approach. Most theoretical works focus on the ground-state or lowest excited-state binding energy (Al-Hayek & Sandouqa, 2015; Baskoutas et al., 2007; Tas & Sahin, 2012; Soltani-Vala & Barvestani, 2017), while there has been little investigation into the higher excited state binding energies of the hydrogenic donor impurity in a QD due to the limitations of the calculation method (Sadeghi, 2009; Wang et al., 2014).

- *Gaussian Impurity:* The choice of Gaussian-like potential function for describing the impurity related potential can also be justified, which conveniently avoids the Coulomb-type singularity as the center is assumed to be charged (Ghosh et al., 2020). Such a smooth potential offers a reasonable approximation (Adamowski et al., 2000; Halonen et al., 1996b; Hosseinpour et al., 2016). The Gaussian potential is described with the finite depth and range which bears a smoothly varying form (Bednarek et al., 2003; Datta & Ghosh, 2011). The Gaussian potential also has further physical implications. A real physical impurity must be of finite range and therefore modeled by an extended potential. If the potentials are extended, they can describe the effect of a tunable central gate (Ganguly & Ghosh, 2016). Gaussian potential is also used in studying the electron impurity states in bulk conductors. Advantage of such kind of potential is that it helps to bypass divergences in the sums and integrals which are present in theoretical calculations (Ermolaev & Rashba, 2008; Sarkar et al., 2016).

- *Screened Coulomb Impurity:* Coulomb and Gaussian potentials are commonly used to describe the impurity potential in QDs whereas the screened Coulomb (or the Debye-Yukawa) potential Varshni (2001a) is less preferred for impurity modeling. The screened Coulomb potential is a short-range potential and tends faster to zero than Coulomb potential at $|\mathbf{r}| \to \infty$ limit Mizutani (2001); Poszwa (2014). As a consequence, the screened Coulomb potential is used in different fields of physics such as atomic physics, nuclear physics, plasma physics, semiconductors, and quantum chemistry Brum et al. (1984); Soylu & Boztosun (2008); Taseli & Eid (1996).

2.4 Two-dimensional Quantum Dots and Rings

Among nanometer-sized structures, two-dimensional quantum dots (2DQDs) and rings (2DQRs) have found a broad range of application in nanotechnology (Boda, 2019; Chakraborty et al., 2018; Niculescu et al., 2017; Salehani et al., 2015). The electronic and optical properties of 2DQDs and 2DQRs bring about the contribution on the development in device technologies such as threshold-less lasers, ultra-dense memories, sensors, batteries, white light-emitting diodes and supercapacitors (Baghramyan et al., 2016; Prasad & Silotia, 2011; Saha & Ghosh, 2015).

In a 2DQD system, the motion of electron is much more strongly confined in the growth direction (taken as the z-direction) by application of a magnetic field and so the electron moves in the two available spatial directions (the x-y direction) (Chakraborty, 1999; Ciftja, 2013). The 2DQDs can be described as an idealization of a realistic quasi-two-dimensional system and be considered to be a reasonably good model (Mukhopadhyay & Chatterjee, 1998). Advancements in nanofabrication technology enable to controlling and tuning the size, shape and composition of 2DQDs (Jacak et al., 1998; Knoss, 2009). Thus, a great deal of works have been devoted on understanding of 2DQDs systems (Laroze et al., 2016; Li et al., 2016; Xie, 2009; Zeng et al., 2014). For example, Tarucha et al. have researched electronic states of a few electron vertical quantum dot atom and they have presented a schematic diagram of a vertical quantum dot in Figure 2.2, where two-dimensional disc-like atom is formed from a double-barrier heterostructure (Tarucha et al., 1998).

The effects of electromagnetic field intensity, the dot size and shape on the nonlinear

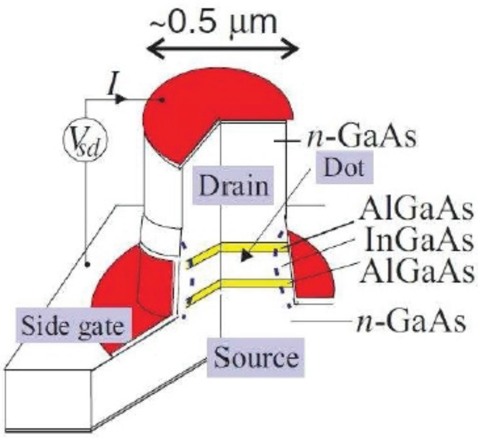

Figure 2.2 Schematic representation of the device containing a disc-shaped dot

optical properties of two-dimensional elliptic quantum dot are investigated by Rezaei and co-workers (Rezaei & Vaseghi, 2010). One of the new studies on the 2DQDs are performed by Ghosh et al (Ghosh et al., 2020). They have showed that the influence of Gaussian white noise on static quadrupole polarizability of the impurity-doped quantum dots.

Just as the QDs, quantum rings confine electrons in all three directions and are characterized by a discrete density of states (Fomin, 2018). 2DQRs, in which the thickness of QR along the growth direction is much smaller than the radial dimensions, has a special position among nanostructures due to their unique electronic, magnetic and optical properties (Duque et al., 2013). For example, they exhibit quantum interference effect such as Aharonov-Bohm which arises from the modification of the electron wave function by a vector potential or persistent current (Barseghyan et al., 2016; A. Lorke et al., 2000; Radu et al., 2014). Therefore, the energy spectra and Aharonov-Bohm oscillations for 2DQRs have become an attractive research topic among researchers. In 1994, Chakraborty and Pietiläinen have investigated the effect of electron-electron interaction on the magnetic moment of electrons in a QR (Chakraborty & Pietiläinen, 1994). Räsänen et al. a complete control of realistic single-electron QRs can be obtained using (quantum) optimal-control theory (Räsänen et al., 2007). The effects of the donor impurity position and of the magnetic field on the optical rectification of a GaAs 2DQR have been performed by Bejan (Bejan, 2017a).

CHAPTER THREE
THEORETICAL BACKGROUND

The aim of this chapter is to review the theoretical framework for a two-dimensional laser-driven quantum dot system including impurity and the nonlinear optical processes such a system. We introduce in Sec. 3.1 the underlying physical background on the laser-atom interactions and the derivation of laser-dressed form of two-dimensional potentials such as Parabolic, Gaussian, Coulomb and Screened Coulomb. The introduction of Finite Element Method is briefly given in Sec. 3.2. Finally, in Sec. 3.3, we derive the expressions of linear and nonlinear optical processes via the density matrix formalism.

3.1 The Effect of Intense Laser Field on The Low-dimensional Systems

Thanks to the development of laser technology, enormous progress in the understanding of the interaction of atoms with laser fields have been facilitated (Anisimov & Khokhlov, 2001; Batani et al., 2001). Hence, the study of light-matter interactions has become an active research topic among researchers. When the radiation laser field, which has adequate intensity, interact with atoms, new intriguing phenomena such as ionization, laser-assisted recombination and laser-assisted collisional ionization occur (Brandi et al., 2001; Gavrila, 1992; Mulser & Bauer, 2010). The laser field is classified in three regimes according to frequency: the low-frequency regime, the high-frequency regime and the intermediate regime (Batani et al., 2001). In this thesis, we have examined the effect of high-frequency intense laser field (ILF) on the low-dimensional systems.

The theory of laser-atom interactions can be tackled by using a semi-classical approach. In the semi-classical method, the laser field is considered classically whereas the atomic system is studied quantum mechanically (Mittleman, 1982). Due to the fact that the number of photons per laser mode is very large, the semi-classical method can be considered to be an appropriate approximation for ILFs (Joachain, 2014).

Let us now consider the interaction of a non-resonant monochromatic right-hand circularly polarized ILF of frequency Ω with a low-dimensional system. The corresponding time-dependent Schrödinger equation describing the system

$$\left(\frac{(\vec{p}+e\vec{A})^2}{2m^*}+V(\vec{r})\right)\psi(\vec{r},t)=i\hbar\frac{\partial\psi(\vec{r},t)}{\partial t} \tag{3.1}$$

where $\vec{p}=-i\hbar\vec{\nabla}$ is the momentum operator and $\vec{A}=\vec{A}(\vec{r},t)$ denotes the vector potential corresponding to the radiation field. By using dipole approximation neglecting the spatial dependence in the vector potential can be written as $\vec{A}(\vec{r},t)\approx\vec{A}(t)$ (Sakiroglu et al., 2017).

In the high-frequency regime, laser-atom interaction can be examined in an accelerated framework called the Kramers-Henneberger (K-H) framework (Hennebergers, 1968). Performing the K-H unitary translation transformation to Equation 3.1, the time dependence in kinetic energy term transfers to the potential energy term (Bejan & Niculescu, 2016a). The operator for the K-H transformation is written as follows

$$U=exp\left[-\frac{i}{\hbar}\left(\frac{e}{m^*}\int\vec{A}\cdot\vec{p}dt+\frac{e^2}{2m^*}\int\vec{A}^2dt\right)\right]. \tag{3.2}$$

In this Equation 3.2, the first term corresponds to a translation operator while the second term produces only a gauge transformation for the term of $\vec{A}^2$ (Lima et al., 2009a).

Applying the K-H transformation to Equation 3.1, the following simpler form can be obtained (Enders et al., 2004):

$$\left(\frac{\vec{p}^2}{2m^*}+V\left(\vec{r}+\vec{\alpha}(t)\right)\right)\varphi(\vec{r},t)=i\hbar\frac{\partial\varphi(\vec{r},t)}{\partial t} \tag{3.3}$$

where $\psi(\vec{r},t)\rightarrow\varphi(\vec{r},t)$ and the displacement vector of a classical electron from its oscillation center owing to its quiver motion in the laser field, $\vec{\alpha}(t)$ is given by $\vec{\alpha}(t)=\int^{t}\vec{A}(t')\,dt'$ (Hennebergers, 1968).

The Equation 3.3, which is space-translated form of Equation 3.1, is suitable to describe electron states. The oscillating potential, $V(\vec{r}+\vec{\alpha}(t))$, interacts with the electrons in the the K-H frame. By expanding $V(\vec{r}+\vec{\alpha}(t))$ in a Fourier-Floquet series ($\varphi(\vec{r},t)=\sum\limits_{n}\varphi_n(\vec{r})e^{-in\Omega t}$), the zeroth-order term becomes more dominant for high enough frequencies (Pont & Gavrila, 1990). The second term appearing on the left-hand side of Equation 3.3 describes the time-averaged laser-dressed potential:

$$\langle V(\vec{r},\alpha_0)\rangle = \frac{1}{T}\int_0^T V(\vec{r}+\vec{\alpha}(t))\,dt \tag{3.4}$$

where the period of the high-frequency ILF is denoted by $T=\frac{2\pi}{\Omega}$ and $\alpha_0=\frac{eA_0}{m^*\Omega}$ is termed as laser-dressing intensity parameter (Lima et al., 2009a).

The vector potential $\vec{A}(t)$ corresponding circularly polarized ILF and $\vec{\alpha}(t)$ can be written as (Pont & Gavrila, 1990):

$$\vec{A}(t) = A_0(-\sin\Omega t\ \hat{x}+\cos\Omega t\ \hat{y}) \tag{3.5}$$

$$\vec{\alpha}(t) = \alpha_0(\cos\Omega t\ \hat{x}+\sin\Omega t\ \hat{y}) \tag{3.6}$$

Here $\hat{x}$ and $\hat{y}$ designate the unit vectors orthogonal to the direction of propagation.

Afterwards, time-independent Schrödinger equation including the effects of high-frequency ILF for the zeroth Floquet component $\varphi(\vec{r})$ with corresponding quasienergy E is given to be:

$$-\frac{\hbar^2}{2m^*}\nabla^2\varphi(\vec{r})+\langle V(\vec{r},\alpha_0)\rangle\varphi(\vec{r}) = E\varphi(\vec{r}) \tag{3.7}$$

The Equation 3.7 can be solved by using various numerical calculations.

3.1.1 The laser-dressed form of Two-dimensional Parabolic Potential

The expression of two-dimensional parabolic potential is given as

$$V_H(r) = \frac{1}{2} m^* \omega_0^2 r^2 \tag{3.8}$$

where m^* is electronic effective mass and ω_0 is the confinement frequency.

By converting $u = \Omega t$, the new form of Equation 3.4 can be obtained as follows:

$$V_{dH} = \frac{1}{2\pi} \int_0^{2\pi} V(|\vec{r} + \vec{\alpha}(u)|) du \tag{3.9}$$

where r is the radial coordinate of electron ($x = r\cos\theta$ and $y = r\sin\theta$)

$$|\vec{r} + \vec{\alpha}(u)|^2 = \vec{r}^2 + \vec{\alpha}^2 + 2\vec{r} \cdot \vec{\alpha} = r^2 + \alpha_0^2 + 2r\alpha_0 \cos(u - \theta) \tag{3.10}$$

$$V_{dH} = \frac{m^*}{4\pi} \omega_0^2 \int_0^{2\pi} du \left(r^2 + \alpha_0^2 + 2r\alpha_0 \cos(u - \theta) \right) \tag{3.11}$$

$$V_{dH} = \frac{m^*}{4\pi} \omega_0^2 \left(2\pi r^2 + 2\pi\alpha_0^2 + 2r\alpha_0 \left(-\sin(u - \theta) \Big|_0^{2\pi} \right) \right) \tag{3.12}$$

$$V_{dH} = \frac{m^*}{4\pi} \omega_0^2 \left(2\pi \left(r^2 + \alpha_0^2 \right) + 2r\alpha_0 (-\sin(2\pi - \theta) - \sin(\theta)) \right) \tag{3.13}$$

Therefore, we obtain the laser-dressed form of parabolic potential

$$V_{dH}(r, \alpha_0) = \frac{1}{2} m^* \omega_0^2 \left(r^2 + \alpha_0^2 \right) \tag{3.14}$$

Here we should note that, the ILF brings about a shift in the parabolic potential.

In attempt to scale the expression of dressed parabolic potential, we choose effective Bohr radius as a length scale and effective Hartree energy $\left(E_h^* = \hbar^2 / m^* a_0^* \right)$, consequently the dimensionless form of laser-dressed parabolic potential is obtained as follows

$$\tilde{V}_{dH}(\tilde{r}, \tilde{\alpha}_0) = \frac{1}{2} \gamma_0^2 \left(\tilde{r}^2 + \tilde{\alpha}_0^2 \right) \tag{3.15}$$

where γ_0 denotes the dimensionless parameter of confinement frequency, $\gamma_0 = \frac{\hbar\omega_0}{E_h^*}$.

3.1.2 Two-dimensional Laser-dressed Gaussian Potential

The expression of two-dimensional Gaussian potential is

$$V_G(r) = -V_0 \; exp\left(-\frac{r}{r_0}\right)^2 \tag{3.16}$$

where V_0 is the depth of the potential dot, r_0 is the range of the confinement potential describing the radius of the QD, r contains x and y coordinates.

With a transformation $u = \Omega t$,

$$V_{dG} = \frac{1}{2\pi} \int_0^{2\pi} V_G(|\vec{r} + \vec{\alpha}(u)|) du \tag{3.17}$$

Using the expression for $|\vec{r} + \vec{\alpha}(u)|^2$ which is obtained in the previous section

$$V_{dG} = -\frac{V_0}{2\pi} exp\left(-\frac{r^2 + \alpha_0^2}{r_0^2}\right) \int_0^{2\pi} du \; exp\left(-\frac{2r\alpha_0}{r_0^2}\cos(u-\theta)\right) \tag{3.18}$$

$$exp(iz\cos\theta) = \sum_{n=-\infty}^{\infty} (i)^n J_n(z) \; exp(in\theta) \tag{3.19}$$

By using the Jacobi-Anger expansion (Colton & Kress, 2010) given Equation 3.19, in the equation given above with the $a = 2r\alpha_0/r_0^2$ exponential term in the integrant transforms to

$$exp(-a\cos(u-\theta)) = \sum_{n=-\infty}^{\infty} (i)^n J_n(ia) \; exp(in\,(u-\theta)) \;.$$

Let's back to integral expression

$$V_{dG} = -\frac{V_0}{2\pi} exp\left(-\frac{r^2+\alpha_0^2}{r_0^2}\right)\sum_{n=-\infty}^{\infty}(i)^n J_n(ia)\underbrace{\int_0^{2\pi} du\ exp\left(in\left(u-\theta\right)\right)}_{2\pi\delta_{n,0}\ exp(-in\theta)} \tag{3.20}$$

$$V_{dG} = -\frac{V_0}{2\pi} exp\left(-\frac{r^2+\alpha_0^2}{r_0^2}\right)2\pi J_0(ia) = -\frac{V_0}{2\pi} exp\left(-\frac{r^2+\alpha_0^2}{r_0^2}\right)2\pi I_0(a) \tag{3.21}$$

where $I_\alpha(x) = i^{-\alpha}J_\alpha(x)$ is modified Bessel function (Hanna & Rowland, 2008).

The laser-dressed Gaussian potential is obtained as follows (Durak, 2015):

$$V_{dG}(r,\alpha_0) = -V_0\ exp\left(-\frac{r^2+\alpha_0^2}{r_0^2}\right)I_0\left(\frac{2r\alpha_0}{r_0^2}\right) \tag{3.22}$$

For the dimensionless form of dressed Gaussian potential, we use effective Bohr radius and effective Hartree energy and the dimensionless form of Equation 3.22 is achieved as:

$$\tilde{V}_{dG}(\tilde{r},\tilde{\alpha}_0) = -\tilde{V}_0\ exp\left(-\frac{\tilde{r}^2+\tilde{\alpha}_0^2}{\tilde{r}_0^2}\right)I_0\left(\frac{2\tilde{r}\tilde{\alpha}_0}{\tilde{r}_0^2}\right). \tag{3.23}$$

3.1.3 Intense Laser Field Effect on Two-dimensional Coulomb Potential

The expression of two-dimensional Coulomb potential is given as

$$V_C = -\frac{e^2}{4\pi\varepsilon_0\epsilon_r r}. \tag{3.24}$$

By transforming $u = \Omega t$, the laser-dressed form of Coulomb potential can be obtained as follows:

$$V_{dC} = \frac{1}{2\pi}\int_0^{2\pi} du V(\vec{r}+\vec{\alpha}(u)) \tag{3.25}$$

$$\vec{r} = r\cos\theta\hat{x} + r\sin\theta\hat{y}$$

$$|\vec{r}+\vec{\alpha}(u)| = \sqrt{\vec{r}^2+\vec{\alpha}^2+2\vec{r}\cdot\vec{\alpha}} = \sqrt{r^2+\alpha_0^2+2r\alpha_0\cos(u-\theta)}$$

The expression of dressed Coulomb potential can be rewritten as

$$V_{dC} = \frac{1}{2\pi}\int_0^{2\pi} du V(|\vec{r}+\vec{\alpha}(u)|) = -\frac{e^2}{4\pi\varepsilon_0\epsilon_r}\frac{1}{2\pi}\int_0^{2\pi}\frac{du}{\sqrt{r^2+\alpha_0^2+2r\alpha\cos(u-\theta)}}$$

$$\begin{aligned}|\vec{r}+\vec{\alpha}(t)|^2 &= r^2+\alpha_0^2+2r\alpha_0\cos(u-\theta) = (r+\alpha_0)^2-2r\alpha_0(\underbrace{1-\cos(u-\theta)}_{2\sin^2(\frac{1}{2}(u-\theta))})\\ &= (r+\alpha_0)^2-4r\alpha_0\sin^2\left(\frac{1}{2}(u-\theta)\right)\end{aligned}$$

$$|\vec{r}+\vec{\alpha}| = (r+\alpha_0)\sqrt{1-\underbrace{\left(\frac{4r\alpha_0}{(r+\alpha_0)^2}\right)}_{m\leq 1}\sin^2\left(\frac{(u-\theta)}{2}\right)}$$

By transforming $\lambda = \frac{1}{2}(u-\theta)$,

$$V_{dC} = -\frac{e^2}{4\pi\varepsilon_0\epsilon_r}\frac{1}{(r+\alpha_0)}\frac{1}{2\pi}\int_{-\theta/2}^{\pi-\theta/2}\frac{2d\lambda}{\sqrt{1-m\sin^2\lambda}}$$

$$V_{dC} = -\frac{e^2}{4\pi\varepsilon_0\epsilon_r}\frac{1}{(r+\alpha_0)}\frac{1}{\pi}\left(\int_{-\theta/2}^{0}\frac{d\lambda}{\sqrt{1-m\sin^2\lambda}}+\int_0^{\pi-\theta/2}\frac{d\lambda}{\sqrt{1-m\sin^2\lambda}}\right) \tag{3.26}$$

By performing the appropriate λ transformations, the Equation 3.26 can be organized as follows:

$$V_{dC} = -\frac{e^2}{4\pi\varepsilon_0\epsilon_r}\frac{1}{(r+\alpha_0)}\frac{1}{\pi}\left(\int_0^{\pi/2}\frac{d\lambda}{\sqrt{1-m\sin^2\lambda}}-\int_{\pi/2}^{0}\frac{d\lambda}{\sqrt{1-m\sin^2\lambda}}\right)$$

$$= -\frac{e^2}{4\pi\varepsilon_0\epsilon_r}\frac{1}{(r+\alpha_0)}\frac{1}{\pi}\left(\int_0^{\pi/2}\frac{d\lambda}{\sqrt{1-m\sin^2\lambda}}+\int_0^{\pi/2}\frac{d\lambda}{\sqrt{1-m\sin^2\lambda}}\right)$$

$$V_{dC} = -\frac{e^2}{4\pi\varepsilon_0\epsilon_r}\frac{1}{(r+\alpha_0)}\frac{2}{\pi}\int_0^{\pi/2}\frac{d\lambda}{\sqrt{1-m\sin^2\lambda}}$$

The laser-dressed Coulomb potential is obtained as:

$$V_{dC}(r,\alpha_0) = -\frac{e^2}{4\pi\varepsilon_0\epsilon_r}\frac{2}{\pi}\frac{1}{(r+\alpha_0)}K(m) \tag{3.27}$$

where $K(m)$ is the elliptic integral of the first kind and $m = \frac{4r\alpha_0}{(r+\alpha_0)^2}$.

By means of effective Bohr radius and effective Hartree energy, nondimensionalization process is performed to facilitate numerical calculations. Accordingly dimensionless form of Equation 3.27 can be written as:

$$\tilde{V}_{dC}(\tilde{r},\tilde{\alpha}_0) = -\frac{2}{\pi}\frac{1}{(\tilde{r}+\tilde{\alpha}_0)}K(m)\,. \tag{3.28}$$

3.1.4 Screened Coulomb Potential Under Intense Laser Field

The two-dimensional Screened Coulomb potential (Varshni, 2001a) is written as

$$V_{SC} = -\frac{e^2}{4\pi\varepsilon_0\epsilon_r}\frac{e^{-\lambda r}}{r}\,, \tag{3.29}$$

where r contains x and y coordinates ($r = \sqrt{x^2+y^2}$; $\quad x = r\cos\theta$; $y = r\sin\theta$).

The Fourier transforms for two-dimensional system are defined as (Deb, 1994)

$$\frac{e^{-\lambda r}}{r} = \frac{1}{2\pi}\int d^2q\frac{e^{i\vec{q}\cdot\vec{r}}}{\sqrt{q^2+\lambda^2}}\,. \tag{3.30}$$

$$q_x = q\cos(\theta_q); \qquad q_y = q\sin(\theta_q); \qquad q = \sqrt{q_x^2+q_y^2}$$

By use of $u = \Omega t$, the laser-dressed form of Screened Coulomb potential can be obtained as follows:

$$V_{dSC}(r,\lambda;\alpha_0) = \frac{1}{2\pi}\int_0^{2\pi} du V(|\vec{r}+\vec{\alpha}(u)|) \tag{3.31}$$

$$V_{dSC}(r,\lambda;\alpha_0) = -\frac{e^2}{4\pi\varepsilon_0\epsilon_r}\frac{1}{2\pi}\int_0^{2\pi} du\left(d^2q\frac{e^{i\vec{q}\cdot(\vec{r}+\vec{\alpha}(u))}}{\sqrt{q^2+\lambda^2}}\right) \tag{3.32}$$

$$V_{dSC}(r,\lambda;\alpha_0) = -\frac{e^2}{4\pi\varepsilon_0\epsilon_r}\int_0^{\infty} dq\frac{q}{\sqrt{q^2+\lambda^2}}\underbrace{\int_0^{2\pi}\frac{d\theta_q}{2\pi}e^{iqr\cos(\theta_q-\theta)}}_{I_1}\underbrace{\int_0^{2\pi}\frac{du}{2\pi}e^{i\vec{q}\cdot\vec{\alpha}(u)}}_{I_2}$$

If we use the Jacobi-Anger expansion given Equation 3.19, the integration becomes as follows

$$\int_0^{2\pi}\frac{d\theta_q}{2\pi}e^{qr\cos(\theta_q-\theta)} = \sum_{n=-\infty}^{\infty}(i)^n J_n(qr)e^{-in\theta}\underbrace{\int_0^{2\pi}\frac{d\theta_q}{2\pi}e^{in\theta_q}}_{\delta_{n,0}} \tag{3.33}$$

$$\int_0^{2\pi}\frac{d\theta_q}{2\pi}e^{qr\cos(\theta_q-\theta)} = J_0(qr)\,.$$

Similarly, by using Jacobi-Anger expansion for I_2,the integration of I_2 is obtained as follows

$$\int_0^{2\pi}\frac{du}{2\pi}e^{q\alpha_0\cos(\theta_q-u)} = \sum_{n=-\infty}^{\infty}(i)^n J_n(q\alpha_0)e^{in\theta_q}\underbrace{\int_0^{2\pi}\frac{du}{2\pi}e^{-inu}}_{\delta_{n,0}} \tag{3.34}$$

where $\vec{q}\cdot\vec{\alpha}(u) = q\alpha_0\cos(\theta_q-u)$. Finally, we organize the equation

$$V_{dSC}(r,\lambda;\alpha_0) = -\frac{e^2}{4\pi\varepsilon_0\epsilon_r}\int_0^{\infty} dq\frac{q}{\sqrt{q^2+\lambda^2}}J_0(qr)J_0(q\alpha_0) \tag{3.35}$$

A dimensionless form of Equation 3.35 is written by using effective Bohr radius and effective Hartree energy:

$$\tilde{V}_{dSC}(\tilde{r},\tilde{\lambda};\tilde{\alpha}_0) = -\int_0^{\infty} dq\frac{q}{\sqrt{q^2+\tilde{\lambda}^2}}J_0(q\tilde{r})J_0(q\tilde{\alpha}_0)\,. \tag{3.36}$$

We should note that for $\tilde{\lambda}=0$, this equation reduces to dressed-Coulomb potential as follows:

$$\tilde{V}_{dSC}(\tilde{r},\tilde{\lambda}=0;\tilde{\alpha}_0) = -\int_0^{\infty} dq J_0(q\tilde{r})J_0(q\tilde{\alpha}_0) \tag{3.37}$$

$$\tilde{V}_{dSC}(\tilde{r}, \tilde{\lambda} = 0; \tilde{\alpha}_0) = -\frac{2}{\pi}\frac{1}{(\tilde{r}+\tilde{\alpha}_0)} K\left(\frac{4\tilde{r}\tilde{\alpha}_0}{(\tilde{r}+\tilde{\alpha}_0)^2}\right). \tag{3.38}$$

3.2 Introduction To Finite Element Method

The finite element method (FEM), which is a well established and convenient numerical technique, is used to solve the complex problems of engineering and mathematical physics (Hutton, 2003; Ram-Mohan, 2002; Reddy, 1993). In the 1940s, the FEM was firstly suggested in the field of structural engineering and then it has been extensively used by different disciplines due to the improvements in FEM (Agrawal & Rahman, 2013). FEM is a powerful tool for the approximate solutions of differential equations and enables a formalism for generating discrete (finite) algorithms (Brenner & Scott, 2007). Compared to other numerical methods, FEM has many advantages. For instances, FEM, which is a variational expansion method, bases on the basis functions which are strictly local, piecewise polynomials (Ram-Mohan, 2002). Owing to the basis function composed polynomials, the control of convergence of the method can be achieved with increment in the number of basis functions or polynomial order. Furthermore, since all of the calculations are done in real space, the method does not need Fourier transforms (Pask et al., 2001). In summarize, FEM is a successful and applicable technique with high accuracy for the various of systems which have irregular geometry or complex boundary conditions (Kwon & Bang, 1997; Ram-Mohan, 2002; Zienkiewicz et al., 2005).

In the FEM, first step is the division of the works space into subdomains. The each of subdomains is named as "global element". "Local element" is obtained by dividing the global elements into subdomains. The properties of global elements are expressed in terms of unknown values at special points referred to "node" where the elements are engaged with each other. The schematic representation of the linear discretization of the work space is demonstrated in Figure 3.1.

To obtain the solution of the system, we will need to denote some functions named as "basis functions" in the finite function space. These basis functions are defined as

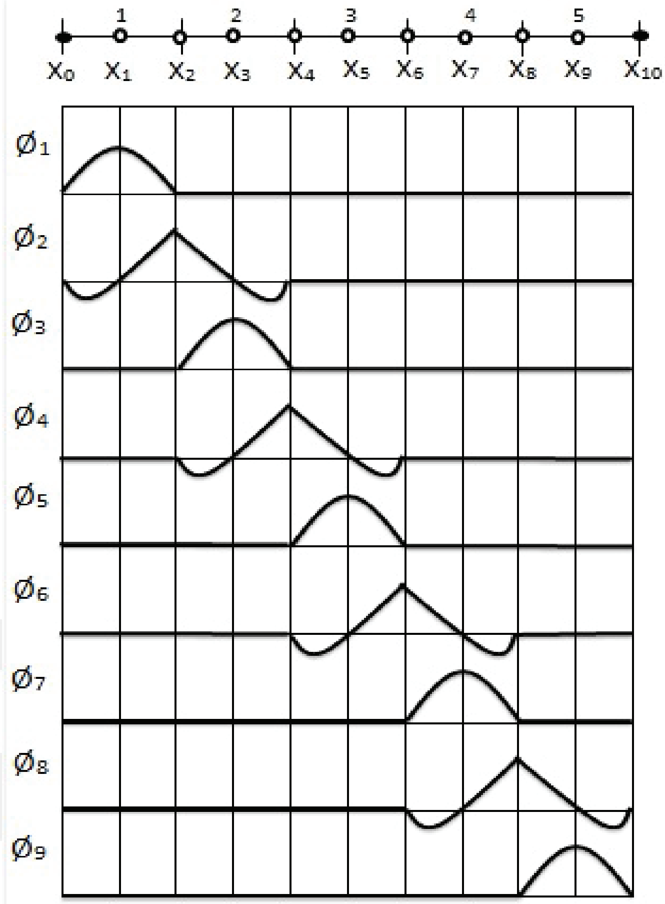

Figure 3.1 Basis functions for a work space with 3 nodes and 5 global elements

$\phi_i(x)$ $(i = 1, 2, ..., n)$. Basis functions are continuous, linear functions on each element and they must satisfy the condition:

$$\phi_i(x_j) = \begin{cases} 1 & i = j, \\ 0 & i \neq j. \end{cases} \tag{3.39}$$

where ϕ_i depicts the i-th main basis function and x_j denotes the j-th node coordinate. As a result, ϕ_i takes the value 1 at $x = x_i$ whereas the value is 0 at all other nodes. This properties of basis functions becomes significant for the approximate solution of more complex systems (Pask et al., 2001).

In the discrete work space, the approximate solution can be written as a linear sum of these basis functions:

$$\Psi(x) = \sum_{i=1}^{n} \psi_i \phi_i(x) \tag{3.40}$$

where $\Psi(x)$ is trial function and satisfies the Dirichlet boundary conditions, ψ_i refers to expansion coefficients.

3.2.1 *Solution of a Confined Quantum Mechanical System with FEM*

We assume a particle confined in a quantum mechanical system. The Hamiltonian of the system is defined as follows:

$$\mathcal{H} = -\frac{\hbar^2}{2m}\nabla^2 + V(\mathbf{r})\,. \tag{3.41}$$

where $V(\mathbf{r})$ is confinement potential.

The dimensionless form of the Hamiltonian can be obtained by using the Bohr radius and effective Hartree energy. Thus, the dimensionless of Hamiltonian and the Schrödinger equation can be written as follows:

$$\tilde{\mathcal{H}} = -\frac{1}{2}\nabla^2 + V(\mathbf{r}) \tag{3.42}$$

$$\tilde{\mathcal{H}}\Psi(\mathbf{r}) = E\Psi(\mathbf{r}) \tag{3.43}$$

where $\tilde{\mathcal{H}}$ refers to the dimensionless form of the Hamiltonian.

We firstly start from the suggestion of trial wave function for solving the Equation 3.43. The closer trial wave function is to the exact wave function, the more accurate the Equation 3.43. The Schrödinger equation including the trial function $\psi(\mathbf{r})$ instead of the exact wave function $\Psi(\mathbf{r})$ is rewritten as:

$$\tilde{\mathcal{H}}\psi(\mathbf{r}) = E\psi(\mathbf{r}) \tag{3.44}$$

For obtaining the approximate solution and find the minimum energies of system, the minimization principle is used to the system. First of all, to solve this eigenvalue problem with FEM, the work space should be divided into subregions. Hence, the wave function can be described as a complete set of the basis functions of relevant work space:

$$\psi(\mathbf{r}) = \sum_{i=1}^{N_{tot}} \psi_i \, \phi_i(\mathbf{r}) \tag{3.45}$$

where ϕ_i and N_{tot} are the basis functions and the number of total nodes in divided work space, respectively. Representation of the square, column and row matrices in FEM is shown as in Figure 3.2.

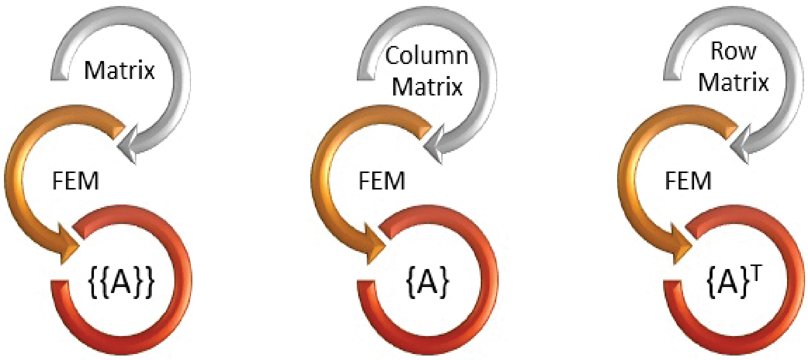

Figure 3.2 The schematic representation of Matrix notation in FEM

Then Equation 3.45 can be rewritten by using the matrix notation:

$$\psi(\mathbf{r}) = \sum_{i=1}^{N_{tot}} \psi_i \, \phi_i(\mathbf{r}) = \left\{ \begin{array}{cccc} \psi_1 & \psi_2 & \ldots & \psi_{N_{tot}} \end{array} \right\} \cdot \left\{ \begin{array}{c} \phi_1(\mathbf{r}) \\ \phi_2(\mathbf{r}) \\ \vdots \\ \phi_{N_{tot}}(\mathbf{r}) \end{array} \right\} = \{\psi\}^T \{\phi(\mathbf{r})\} \tag{3.46}$$

$$\psi(\mathbf{r}) = \{\phi(\mathbf{r})\}^T \cdot \{\psi\} \tag{3.47}$$

where

$$\{\phi(\mathbf{r})\}^T = (\phi_1(\mathbf{r}), \phi_2(\mathbf{r}), \phi_3(\mathbf{r}), \ldots \phi_{N_{tot}}(\mathbf{r})) \tag{3.48}$$

$$\{\psi\}^T = (\psi_1, \psi_2, \psi_3, \ldots, \psi_{N_{tot}}) \ . \tag{3.49}$$

and the hermitian conjugate of $\psi(\mathbf{r})$ is given as:

$$\psi^\dagger(\mathbf{r}) = \{\psi\}^\dagger \cdot \{\phi(\mathbf{r})\} \ . \tag{3.50}$$

Here "Galerkin's Method " can be used to achieve variational parameters, ψ_i (Kwon & Bang, 1997).

In "Galerkin's Method ", firstly, the Schrödinger equation including the desired wave function $\psi(\mathbf{r})$ is written. Subsequently, it is multiplied by $\psi^\dagger(\mathbf{r})$ on the left hand side and taken integral in the work space. As a conclusion, the G (Galerkian) minimized by the variational variables can be obtained as follows:

$$G = \int_\Omega \psi^\dagger(\mathbf{r})(\hat{\mathcal{H}} - E\mathbf{I})\psi(\mathbf{r}) \, d\Omega \tag{3.51}$$

where $\mathbf{I}$ is the unit matrix ($N_{tot} \times N_{tot}$). The G can be computed using the definitions of $\psi(\mathbf{r})$ and $\psi^\dagger(\mathbf{r})$ given by Equation 3.47 and 3.50 as follows:

$$G = \{\psi\}^\dagger \cdot \left[\int_\Omega \{\phi\}(\hat{\mathcal{H}} - E\mathbf{I})\{\phi\}^T d\Omega \right] \cdot \{\psi\} \ . \tag{3.52}$$

Applying the variational method in which minimizing the expression of G, the wave function is determined as follows:

$$\frac{\partial G}{\partial \psi^\dagger} = 0 \quad \Rightarrow \quad \left[\int_\Omega \{\phi\}(\hat{\mathcal{H}} - E\mathbf{I})\{\phi\}^T \, d\Omega \right] \cdot \{\psi\} = 0 \ . \tag{3.53}$$

Substituting the expression of Hamiltonian given by Equation 3.42 in Equation 3.53, we obtain:

$$\left[\int_\Omega d\Omega \left[-\frac{1}{2}\{\phi\} \cdot \nabla^2 \{\phi\}^T + \{\phi\} V(\mathbf{r}) \{\phi\}^T \right] \right] \cdot \{\psi\} = E \left[\int_\Omega d\Omega \{\phi\}\{\phi\}^T \right] \cdot \{\psi\} \ . \tag{3.54}$$

The expression of kinetic term in the Hamiltonian is written as:

$$-\int_{\Omega} \{\phi\} \cdot \nabla^2 \{\phi\}^T \, d\Omega = \int_{\Omega} \nabla\{\phi\} \cdot \nabla\{\phi\}^T \, d\Omega - \int_{\Omega} \nabla\left(\{\phi\} \cdot \nabla\{\phi\}^T\right) d\Omega \,. \tag{3.55}$$

By means of Gauss Theorem, the second term of Equation 3.55 can be transformed to a surface integral as following:

$$\int_{\Omega} \nabla(\{\phi\} \cdot \nabla\{\phi\}^T) \, d\Omega = \int_{\partial\Omega} \{\phi\}(\nabla\{\phi\}^T) \cdot d\mathbf{S} \,. \tag{3.56}$$

Taking notice of the boundary conditions, the wave function and its conjugate have to be zero on the surface of the solution space of the physical system, consequently, no contribution from surface terms enters into the kinetic term. By using Equations 3.55 and 3.56, the Equation 3.54 is rewritten as below

$$\left[\int_{\Omega} d\Omega \left[\frac{1}{2}\nabla\{\phi\} \cdot \nabla\{\phi\}^T + \{\phi\}V(\mathbf{r})\{\phi\}^T\right]\right] \cdot \{\psi\} = E\left[\int_{\Omega} d\Omega\{\phi\}\{\phi\}^T\right] \cdot \{\psi\} \,. \tag{3.57}$$

The matrix representation of Equation 3.55 is given as:

$$\{\{K\}\} \cdot \{\psi\} = E \, \{\{M\}\} \cdot \{\psi\} \tag{3.58}$$

where $\{\{K\}\}$, $\{\{M\}\}$ are "*Stiffness Matrix*" and "*Mass Matrix*", respectively. Equation 3.58 corresponds to generalized eigenvalue equation of the system and the expressions of $\{\{K\}\}$ and $\{\{M\}\}$ are defined as following:

$$\{\{K\}\} = \int_{\Omega} d\Omega \left[\frac{1}{2}\nabla\{\phi\} \cdot \nabla\{\phi\}^T + \{\phi\}V(\mathbf{r})\{\phi\}^T\right] \tag{3.59}$$

$$\{\{M\}\} = \int_{\Omega} d\Omega\{\phi\}\{\phi\}^T \,. \tag{3.60}$$

Herein, we can define the summation of the integrals over the divided work space elements instead of the integrals over the whole of work space as following:

$$\int_{\Omega} d\Omega = \sum_{e=1}^{N_{ge}} \int_{\Omega_e} d\Omega_e \tag{3.61}$$

where N_{ge} corresponds to the number of global elements. Accordingly, the redefinitions of the stiffness and mass matrices are

$$\{\{K\}\} = \sum_{e=1}^{N_{ge}} \{\{k_e\}\} \tag{3.62}$$

$$\{\{k_e\}\} = \int_{\Omega_e} d\Omega_e \left[\frac{1}{2} \nabla\{N\} \cdot \nabla\{N\}^T + \{N\} V(\mathbf{r}) \{N\}^T \right]. \tag{3.63}$$

$$\{\{k_e\}\} = \{\{k_{e,kin}\}\} + \{\{k_{e,pot}\}\}$$

$$\{\{k_{e,kin}\}\} = \int_{\Omega_e} d\Omega_e \left[\frac{1}{2} \nabla\{N\} \nabla\{N\}^T \right] \tag{3.64}$$

$$\{\{k_{e,pot}\}\} = \int_{\Omega_e} d\Omega_e \left[\{N\} V \{N\}^T \right] \tag{3.65}$$

$$\{\{M\}\} = \sum_{e=1}^{N_{ge}} \{\{m_e\}\} \tag{3.66}$$

$$\{\{m_e\}\} = \int_{\Omega_e} d\Omega_e \; \{N\}\{N\}^T \tag{3.67}$$

where $\{\{k_{e,kin}\}\}$ and $\{\{k_{e,pot}\}\}$ are the terms of kinetic energy and potential energy, respectively. $\{N\}$ indicates the basis function of global element.

In this work, for calculations, the numbers of total nodes and global element nodes are taken as N_{tot} = 1500 and N_{gen} = 10, respectively. The total of basis function is calculated as $N_{ge} \cdot N_{gen} - \left(N_{ge} - 1\right)$ where $N_{ge} = (N_{tot} - 1) / \left(N_{gen} - 1\right)$ denotes the number of global element.

3.3 Nonlinear Optics

The discovery of the laser led to the emergence of the practical applications of nonlinear optical effects (Saleh & Teich, 1991). Thus, the nonlinear optics has become an important field and extensively studied field by researchers (Rezaei & Vaseghi, 2010). Various nonlinear effects in the interaction between laser and matter are examined by the nonlinear optics (Khordad, 2017). When electromagnetic radiation interacts with solid, if the intensity of light is not high enough, the dipoles in the solid emit the same frequency as the electromagnetic radiation. Nevertheless, if the electromagnetic radiation has high-intensity, the nonlinear effects begin to seen (Wilson & Hawkes, 1998).

Thanks to the invention of the laser, the modern optics based on the stimulated radiation light source have arisen. The rapid advances in laser technology has led to the appearance of investigations about nonlinear phenomena (Powers, 2013). Afterwards, a first measurement of second-harmonic generation was observed using a quartz crystal by Franken et al. (Franken et al., 1961). In the same year, Kaiser and Garrett showed two-photon absorption in CaF_2:Eu^{2+} crystals (Kaiser & Garrett, 1961). In 1962, the observation of optical rectification coefficient (Bass et al., 1692) and third-harmonic generation (Terhune et al., 1692) was performed. Ashkin et al. observed the optically-induced inhomogeneity in the refractive index of crystals (Ashkin et al., 1966).

In linear optics, the medium is irradiated by the incident electromagnetic radiation with electric field vector $\mathbf{E}(t)$. The induced polarization $\mathbf{P}(t)$, which is described the dipole moment per unit volume, depends linearly on the amplitude of $\mathbf{E}(t)$ and the relationship between them is given as follows (Boyd, 2008):

$$\mathbf{P}(t) = \epsilon_0 \, \chi^{(1)} \, \mathbf{E}(t) \tag{3.68}$$

where ϵ_0 and $\chi^{(1)}$ are the permittivity of free space and the linear susceptibility, respectively.

In the case of nonlinear optics, this relationship can be written as

$$\mathbf{P}(t) = \epsilon_0 \left[\chi^{(1)} \cdot \mathbf{E}(t) + \chi^{(2)} \cdot \mathbf{E}^2(t) + \chi^{(3)} \cdot \mathbf{E}^3(t) + \cdots\right] \tag{3.69}$$

where $\chi^{(2)}$ and $\chi^{(3)}$ correspond to the second- and third-order nonlinear susceptibilities, respectively.

The nonlinear optical processes in material are classified by using the mathematical expression given by Equation 3.69. In attempt to obtain the linear and nonlinear susceptibilities, we consider a system which is irradiated by a monochromatic radiation field with frequency ω and the electric field vector of radiation field can be written as:

$$\mathbf{E}(t) = \tilde{\mathbf{E}} e^{i\omega t} + \tilde{\mathbf{E}} e^{-i\omega t} . \tag{3.70}$$

Substituting the expression of electric field vector given by Equation 3.70 in Equation 3.69, the polarization is rewritten as follows:

$$\mathbf{P}(t) = \epsilon_0 \left(\chi_{\omega}^{(1)} \mathbf{E} e^{i\omega t} + \chi_0^{(2)} \mathbf{E}^2 + \chi_{2\omega}^{(2)} \mathbf{E}^2 e^{2i\omega t} + \chi_{\omega}^{(3)} \mathbf{E}^2 \mathbf{E} e^{i\omega t} + \chi_{3\omega}^{(3)} \mathbf{E}^3 e^{3i\omega t} + \cdots\right) . \tag{3.71}$$

Here $\chi_{\omega}^{(1)}$ is the linear susceptibility, $\chi_0^{(2)}$ refers to the optical rectification coefficient, $\chi_{2\omega}^{(2)}$ denotes the second-harmonic generation, $\chi_{\omega}^{(3)}$ and $\chi_{3\omega}^{(3)}$ correspond to third-order susceptibility and third-harmonic generation, respectively (Boyd, 2008).

3.3.1 The Derivation of the Nonlinear Optical Susceptibilities

In this subsection, the analytical expressions of nonlinear optical susceptibilities will be derived based on density matrix formulation of quantum mechanics. In quantum mechanics, all of the physical properties of a s-state the system are defined by the wave function $\psi_s(\mathbf{r}, t)$ that satisfies the Schrödinger equation (Boyd, 2008)

$$i\hbar \frac{\partial \psi_s(\mathbf{r}, t)}{\partial t} = \hat{H} \psi_s(\mathbf{r}, t) . \tag{3.72}$$

Here $\hat{H}$ represents the Hamiltonian of system and is given as $\hat{H} = \hat{H}_0 + \hat{V}(t)$, (where $\hat{H}_0$ denotes the Hamiltonian of free atom and $\hat{V}(t)$ is the interaction energy).

The $\psi_s(\mathbf{r},t)$ wave function can be written in terms of a complete set of basis functions

$$\psi_s(\mathbf{r},t) = \sum_n C_n^s(t) u_n(\mathbf{r}) \tag{3.73}$$

where C_n^s is expansion coefficient, which corresponds the probability amplitude of an atom known to be at the n-th energy level at time t.

Substituting Equation 3.73 into Equation 3.72 we have

$$i\hbar \sum_n \frac{dC_n^s(t)}{dt} u_n(\mathbf{r}) = \sum_n C_n^s(t) \hat{H} u_n(\mathbf{r}) \tag{3.74}$$

where both side of Equation 3.74 contain the sum of all energy values of the system. For simplicity, both side of Equation 3.74 are multiplied by $u_m^*(\mathbf{r})$ and are taken integral over all space. Using the orthogonality condition given by $\int u_m^*(\mathbf{r}) u_n(\mathbf{r}) d^3r = \delta_{mn}$, the left-hand side of Equation 3.74 is reduced to a single term and the right-hand side can be rewritten by using the expression of the matrix elements of the Hamiltonian operator $\hat{H}$, which is defined by $H_{mn} = \int u_m^*(\mathbf{r}) \hat{H} u_n(\mathbf{r}) d^3r$. The rearranged Equation 3.74 is given as follows

$$i\hbar \frac{d}{dt} C_m^s(t) = \sum_n H_{mn} C_n^s(t)\,. \tag{3.75}$$

As we know from quantum mechanics, we can determine the expectation value of any observable quantity by means of the wavefunction of the system. The basic postulate of quantum mechanics implies that a Hermitian operator $\hat{A}$ corresponds to any observable quantity of A. The expectation value of A can be written as:

$$\langle A \rangle = \int \psi_s^* \, \hat{A} \, \psi_s \, d^3r \tag{3.76}$$

where this equation, which specifies a quantum-mechanical average, is denoted by $\langle A \rangle = \langle \psi_s | \hat{A} | \psi_s \rangle = \langle s | \hat{A} | s \rangle$ in Dirac notation.

The Equation 3.76 can be rewritten by using Equation 3.73

$$\langle A \rangle = \sum_{mn} C_m^{s*} C_n^s A_{mn} \tag{3.77}$$

where the matrix elements A_{mn} is determined by $A_{mn} = \langle u_m | \hat{A} | u_n \rangle = \int u_m^* \hat{A} u_n d^3 r$.

The formalism described above completely describes the time evolution of observables of system so long as the initial state and the Hamiltonian operator $\hat{H}$ for the system are known. Nevertheless, the exact state of the system is not known in some cases and so the system can be statistically identified by means of the density matrix formalism. Initially, we describe $p(s)$, which indicates the probability of system to be at the state s. Here, this quantity can be considered as a classical rather than a quantum mechanical probability and designates the lack of information regarding the quantum mechanical state of the system (Boyd, 2008). In this case, the elements of the density matrix of the system are described by

$$\rho_{nm} = \sum_{s} p(s) C_m^{s*} C_n^s = \overline{C_m^* C_n} \tag{3.78}$$

where the overbar depicts an average over all possible states of the system.

In order to calculate the expected value of any observable quantity, the density matrix can be used easily (Karabulut, 2008). For the case where the exact state of the system is not known, the expected value is achieved by averaging over all possible states of the system,

$$\overline{\langle A \rangle} = \sum_{s} p(s) \sum_{nm} C_m^{s*} C_n^s \tag{3.79}$$

By using Equation 3.78, the equation is rearranged as follows

$$\overline{\langle A \rangle} = \sum_{nm} \rho_{nm} A_{mn} \equiv tr\left(\hat{\rho} \hat{A}\right) \tag{3.80}$$

Taking the derivative of Equation 3.78 with respect to time, we obtain as

$$\dot{\rho}_{nm} = \sum_s \frac{dp(s)}{dt} C_m^{s*} C_n^s + \sum_s p(s) \left(C_m^{s*} \frac{dC_n^s}{dt} + \frac{dC_m^{s*}}{dt} C_n^s \right) . \tag{3.81}$$

Here we suppose that $p(s)$ does not vary in time and so the first term of Equation 3.81 equals to zero. The second term can calculated by using Schrödinger equation and is obtained as following

$$\dot{\rho}_{nm} = \sum_s p(s) \frac{i}{\hbar} \sum_v (C_n^s C_v^{s*} H_{vm} - C_m^{s*} C_v^s H_{nv}) \tag{3.82}$$

Substituting the expression of the density matrix given by Equation 3.78 in the above equation, the resulting expression as follows:

$$\dot{\rho}_{nm} = \frac{i}{\hbar} \left(\hat{\rho}\hat{H} - \hat{H}\hat{\rho} \right)_{nm} = \frac{1}{i\hbar} \left[\hat{H}, \hat{\rho} \right]_{nm} \tag{3.83}$$

where $\hat{H} = \hat{H}_0 + \hat{V}(t)$. Hamiltonian consists of the sum of the unperturbed Hamiltonian $\hat{H}_0$ with the interaction energy between atom and electromagnetic radiation field $\hat{V}(t)$. Equation 3.83 is the equation of motion for the density matrix known as the Liouville equation:

$$\dot{\rho}_{nm} = \frac{1}{i\hbar} \left[\hat{H}_0 + \hat{V}(t), \hat{\rho} \right]_{nm} . \tag{3.84}$$

In fact, the formalism we mentioned above does not include some interactions such as interactions between atoms. These kind of interactions can bring about an alteration in the state of the system and $dp(s)/dt$ to be nonzero. When such interactions are included in the formalism, we need to add the damping terms to the Liouville equation. The new form of Liouville equation can be written as

$$\dot{\rho}_{nm} = \frac{1}{i\hbar} \left[\hat{H}_0 + \hat{V}(t), \hat{\rho} \right]_{nm} - \Gamma_{nm} \left(\rho_{nm} - \rho_{nm}^{(eq)} \right) \tag{3.85}$$

where $\rho_{nm}^{(eq)}$ denotes the density matrix in the thermal equilibrium, Γ_{nm} is a phenomenological damping term and Γ_{nm} is assumed to equal Γ_{mn}.

In general, it is not possible to obtain the solution of Equation 3.85 analytically. Therefore, we benefit from Perturbation method, which is an approximate solution technique to obtain the solution (Boyd, 2008). Firstly, the expression of Hamiltonian is rewritten as below

$$\hat{H} = \hat{H}_0 + \hat{V}(t) \tag{3.86}$$

Here we suppose that the expected value of interaction energy between atom and electromagnetic radiation field is weaker than the expected value of unperturbed Hamiltonian. By use of the electric dipole approximation, the interaction energy is given

$$\hat{V} = -\hat{\boldsymbol{\mu}} \cdot \tilde{\mathbf{E}}(t) \tag{3.87}$$

where $\hat{\boldsymbol{\mu}} = -e\hat{\mathbf{r}}$ is the electric dipole moment operator.

By rearranging the Equation 3.85, we get the following equation:

$$\dot{\rho}_{nm} = -i\omega_{nm}\,\rho_{nm} + \frac{1}{i\hbar}\left(V_{n\nu}\rho_{\nu m} - \rho_{n\nu}V_{\nu m}\right) - \Gamma_{nm}\left(\rho_{nm} - \rho_{nm}^{(eq)}\right) \tag{3.88}$$

where ω_{nm} denotes the transition frequency.

To get the perturbation solution of Equation 3.85, the term V_{ij} in the equation is replaced with λV_{ij}. The λ is a parameter that determines the strength of perturbation, which takes a value between 0 and 1 (Boyd, 2008; Karabulut, 2008). The value of $\lambda = 1$ corresponds to the actual physical state. Here we assume that λ has a solution in terms of force series and this solution is given as

$$\rho_{nm} = \rho_{nm}^{(0)} + \lambda\rho_{nm}^{(1)} + \lambda^2\rho_{nm}^{(2)} + \ldots \tag{3.89}$$

If the Equation 3.89 is a solution of Equation 3.88, the coefficients of each power of λ must be equal to each other and thus the set of equations are achieved as below

$$\dot{\rho}_{nm}^{(0)} = -i\omega_{nm}\rho_{nm}^{(0)} - \Gamma_{nm}\left(\rho_{nm}^{(0)} - \rho_{nm}^{(eq)}\right), \tag{3.90}$$

$$\dot{\rho}_{nm}^{(1)} = -\left(i\omega_{nm} + \Gamma_{nm}\right)\rho_{nm}^{(1)} + \frac{1}{i\hbar}\left[\hat{V}, \hat{\rho}^{(0)}\right]_{nm}, \tag{3.91}$$

$$\dot{\rho}_{nm}^{(2)} = -(i\omega_{nm} + \Gamma_{nm})\rho_{nm}^{(2)} + \frac{1}{i\hbar}\left[\hat{V}, \hat{\rho}^{(1)}\right]_{nm} . \quad (3.92)$$

The steady-state solution of Equation 3.90 can be taken as:

$$\rho_{nm}^{(0)} = \rho_{nm}^{(eq)}, \quad (3.93)$$

and integrating the Equation 3.91, the following equation is obtained:

$$\rho_{nm}^{(1)}(t) = \int_{-\infty}^{t} \frac{1}{i\hbar}\left[\hat{V}(t'), \hat{\rho}^{(0)}\right]_{nm} e^{(i\omega_{nm}+\Gamma_{nm})\left(t'-t\right)} dt' . \quad (3.94)$$

In the same way, the higher order terms can be obtained and the obtained expressions are formally similar to the Equation 3.94.

As the first application of density matrix equations, the linear susceptibility for an atomic system will be calculated. The applied field can be written as

$$\tilde{\mathbf{E}}(\mathbf{t}) = \sum_{p} \mathbf{E}(\omega_p) e^{-i\omega_p t} . \quad (3.95)$$

By using the Equation 3.87, the commutator expression in equation is obtained as follows

$$\left[\hat{V}(t'), \hat{\rho}^{(0)}\right]_{nm} = -\left(\rho_{mm}^{(0)} - \rho_{nn}^{(0)}\right)\boldsymbol{\mu}_{nm} \cdot \tilde{\mathbf{E}}(t) . \quad (3.96)$$

If the Equations 3.96 and 3.95 are substituted into the Equation 3.94, we obtain

$$\begin{aligned} \rho_{nm}^{(1)}(t) &= -\frac{1}{i\hbar}\left(\rho_{mm}^{(0)} - \rho_{nn}^{(0)}\right)\boldsymbol{\mu}_{nm} \sum_{p} \mathbf{E}(\omega_p) \\ &\times \; e^{-(i\omega_{nm}+\Gamma_{nm})t} \int_{-\infty}^{t} e^{\left[i\left(\omega_{nm}-\omega_p\right)+\Gamma_{nm}\right]t'} dt' \end{aligned} \quad (3.97)$$

The integral expression in Equation 3.97 can be calculated as

$$e^{-(i\omega_{nm}+\Gamma_{nm})t} \int_{-\infty}^{t} e^{\left[i\left(\omega_{nm}-\omega_p\right)+\Gamma_{nm}\right]t'} dt^{t'} = \frac{e^{-i\omega_p t}}{i\left(\omega_{nm} - \omega_p\right) + \Gamma_{nm}} \quad (3.98)$$

Substituting the Equation 3.98 in Equation 3.97, $\rho_{nm}^{(1)}$ can be rewritten as

$$\rho_{nm}^{(1)}(t) = \frac{1}{\hbar}\left(\rho_{mm}^{(0)} - \rho_{nn}^{(0)}\right)\sum_{p} \frac{\boldsymbol{\mu}_{nm} \cdot \mathbf{E}(\omega_p) e^{-i\omega_p t}}{\left(\omega_{nm} - \omega_p\right) - i\Gamma_{nm}} \tag{3.99}$$

and then this result is used to obtain the expectation value of dipole moment:

$$\begin{aligned} \langle\hat{\boldsymbol{\mu}}(t)\rangle &= tr\left(\hat{\rho}^{(1)}\hat{\boldsymbol{\mu}}\right) = \sum_{nm} \rho_{nm}^{(1)}\boldsymbol{\mu}_{mn} \qquad (3.100) \\ &= \sum_{nm} \frac{1}{\hbar}\left(\rho_{mm}^{(0)} - \rho_{nn}^{(0)}\right)\sum_{p} \frac{\boldsymbol{\mu}_{mn}\left[\boldsymbol{\mu}_{nm} \cdot \mathbf{E}(\omega_p)\right] e^{-i\omega_p t}}{\left(\omega_{nm} - \omega_p\right) - i\Gamma_{nm}} . \end{aligned}$$

We can write the expression $\langle\hat{\boldsymbol{\mu}}(t)\rangle$ as a frequency component:

$$\langle\hat{\boldsymbol{\mu}}(t)\rangle = \sum_{p} \langle\boldsymbol{\mu}(\omega_p)\rangle e^{-i\omega_p t} \tag{3.101}$$

by using Equation 3.68, the linear susceptibility tensor is given as below:

$$\mathbf{P}(\omega_p) = N\langle\boldsymbol{\mu}(\omega_p)\rangle = \varepsilon_0 \boldsymbol{\chi}^{(1)}(\omega_p) \cdot \mathbf{E}(\omega_p) \tag{3.102}$$

$$\boldsymbol{\chi}^{(1)}(\omega_p) = \frac{N}{\epsilon_0 \hbar}\sum_{nm}\left(\rho_{mm}^{(0)} - \rho_{nn}^{(0)}\right)\frac{\boldsymbol{\mu}_{mn}\boldsymbol{\mu}_{nm}}{\left(\omega_{nm} - \omega_p\right) - i\Gamma_{nm}} \tag{3.103}$$

The Cartesian component form of Equation 3.103 can be given as

$$\chi_{ij}^{(1)}(\omega_p) = \frac{N}{\epsilon_0 \hbar}\sum_{nm}\left(\rho_{mm}^{(0)} - \rho_{nn}^{(0)}\right)\frac{\mu_{mn}^{i}\mu_{nm}^{j}}{\left(\omega_{nm} - \omega_p\right) - i\Gamma_{nm}} \tag{3.104}$$

The evaluations of the second- and third-order nonlinear susceptibilities are similar to the calculation in the linear susceptibility. Consequently, the second-order nonlinear susceptibility can be expressed below as (Boyd, 2008):

$$
\begin{aligned}
\chi^{(2)}_{ijk}(\omega_p+\omega_q,\omega_q,\omega_p) &= \frac{N}{2\epsilon_0\hbar^2} \\
&\times \sum_{mnv}\left(\rho^{(0)}_{mm}-\rho^{(0)}_{vv}\right)\left(\frac{\mu^i_{mn}\mu^j_{nv}\mu^k_{vm}}{\left[\left(\omega_{nm}-\omega_p-\omega_q\right)-i\Gamma_{nm}\right]\left[\left(\omega_{vm}-\omega_p\right)-i\Gamma_{vm}\right]}\right. \\
&+ \left.\frac{\mu^i_{mn}\mu^k_{nv}\mu^j_{vm}}{\left[\left(\omega_{nm}-\omega_p-\omega_q\right)-i\Gamma_{nm}\right]\left[\left(\omega_{vm}-\omega_q\right)-i\Gamma_{vm}\right]}\right) \\
&- \left(\rho^{(0)}_{vv}-\rho^{(0)}_{nn}\right)\left(\frac{\mu^i_{mn}\mu^j_{vm}\mu^k_{nv}}{\left[\left(\omega_{nm}-\omega_p-\omega_q\right)-i\Gamma_{nm}\right]\left[\left(\omega_{nv}-\omega_p\right)-i\Gamma_{nv}\right]}\right. \\
&+ \left.\frac{\mu^i_{mn}\mu^k_{vm}\mu^j_{nv}}{\left[\left(\omega_{nm}-\omega_p-\omega_q\right)-i\Gamma_{nm}\right]\left[\left(\omega_{nv}-\omega_q\right)-i\Gamma_{nv}\right]}\right)
\end{aligned}
\tag{3.105}
$$

and the third-order susceptibility (Boyd, 2008; Karabulut, 2008) is given by

$$
\chi^{(3)}_{kjih}(\omega_p+\omega_q+\omega_r,\omega_r,\omega_q,\omega_p) = \frac{N}{\epsilon_0\hbar^3}\mathcal{P}_I\sum_{nmvl} \tag{3.106}
$$

$$
\begin{aligned}
&\frac{\left(\rho^{(0)}_{mm}-\rho^{(0)}_{ll}\right)\mu^k_{mn}\mu^j_{nv}\mu^i_{vl}\mu^h_{lm}}{\left[\left(\omega_{nm}-\omega_p-\omega_q-\omega_r\right)-i\Gamma_{nm}\right]\left[\left(\omega_{vm}-\omega_p-\omega_q\right)-i\Gamma_{vm}\right]\left[\left(\omega_{lm}-\omega_p\right)-i\Gamma_{lm}\right]} \\
&-\frac{\left(\rho^{(0)}_{ll}-\rho^{(0)}_{vv}\right)\mu^k_{mn}\mu^j_{nv}\mu^i_{lm}\mu^h_{vl}}{\left[\left(\omega_{nm}-\omega_p-\omega_q-\omega_r\right)-i\Gamma_{nm}\right]\left[\left(\omega_{vm}-\omega_p-\omega_q\right)-i\Gamma_{vm}\right]\left[\left(\omega_{vl}-\omega_p\right)-i\Gamma_{vl}\right]} \\
&-\frac{\left(\rho^{(0)}_{vv}-\rho^{(0)}_{ll}\right)\mu^k_{mn}\mu^j_{vm}\mu^i_{nl}\mu^h_{lv}}{\left[\left(\omega_{nm}-\omega_p-\omega_q-\omega_r\right)-i\Gamma_{nm}\right]\left[\left(\omega_{nv}-\omega_p-\omega_q\right)-i\Gamma_{nv}\right]\left[\left(\omega_{lv}-\omega_p\right)-i\Gamma_{lv}\right]} \\
&+\frac{\left(\rho^{(0)}_{ll}-\rho^{(0)}_{nn}\right)\mu^k_{mn}\mu^j_{vm}\mu^i_{lv}\mu^h_{nl}}{\left[\left(\omega_{nm}-\omega_p-\omega_q-\omega_r\right)-i\Gamma_{nm}\right]\left[\left(\omega_{nv}-\omega_p-\omega_q\right)-i\Gamma_{nv}\right]\left[\left(\omega_{nl}-\omega_p\right)-i\Gamma_{nl}\right]}
\end{aligned}
$$

where N is atomic number density. $\mathcal{P}_I$ denotes permutation operator, which defines the input frequencies ω_p,ω_q and ω_r averaged over all possible permutations. Here, the cartesian indices h, i, j are permuted at the same time (Boyd, 2008).

Next subsection, the third-harmonic generation coefficient, the linear and nonlinear absorption coefficients and refractive index changes are calculated through the agency of Equations 3.104, 3.105 and 3.106.

3.3.2 *The Absorption Coefficients and Refractive Index Changes*

The rapid developments in nanotechnology lead to a need of materials with high values of nonlinear optical parameters as the nonlinear absorption coefficient and refractive index changes, for instance (Boyd, 2008; Hosseinpour et al., 2016). The absorption coefficient (AC) indicates the amount of light penetration into a material whereas the refractive index (RI) is a measure of the bending of a light in case of passing from one medium into another (Hecht, 2001). Both absorption coefficient and refractive index change depend on light intensity (Boyd, 2008).

The relation between absorption coefficient and susceptibility is given

$$\alpha(\omega) = \omega\sqrt{\frac{\mu}{\epsilon_r}} Im(\,\chi(\omega)\,) \tag{3.107}$$

and by using Equations 3.104 and 3.106, the expressions of the linear and third-order absorption coefficients can be written as (Liu et al., 2012):

$$\alpha^{(1)}(\omega) = \omega\sqrt{\frac{\mu}{\epsilon_r}} \frac{\sigma_s |M_{10}|^2 \hbar\Gamma_0}{(E_{10}-\hbar\omega)^2+(\hbar\Gamma_0)^2} \tag{3.108}$$

$$\begin{aligned} \alpha^{(3)}(\omega, I) &= -\omega\sqrt{\frac{\mu}{\epsilon_r}} \left(\frac{I}{2n_r\epsilon_0 c}\right) \frac{\sigma_s \hbar\Gamma_0 |M_{10}|^2}{[(E_{10}-\hbar\omega)^2+(\hbar\Gamma_0)^2]^2} \\ &\times \left\{ 4|M_{10}^2| - |M_{11}-M_{00}|^2 \times \frac{\left[3E_{10}^2 - 4\varepsilon_{10}\hbar\omega + \hbar^2(\omega^2-\Gamma_0^2)\right]}{E_{10}^2+(\hbar\Gamma_0)^2} \right\}. \end{aligned} \tag{3.109}$$

Similarly, the linear and the third-order nonlinear refractive index changes are derived as (Rezaei & Vaseghi, 2010):

$$\frac{\Delta n^{(1)}(\omega)}{n_r} = \frac{1}{2n_r^2\epsilon_0} |M_{10}|^2 \sigma_s \left[\frac{\varepsilon_{10}-\hbar\omega}{(\varepsilon_{10}-\hbar\omega)^2+(\hbar\Gamma_0)^2}\right] \tag{3.110}$$

$$\begin{aligned}\frac{\Delta n^{(3)}(\omega,I)}{n_r} &= -\frac{\mu c}{4n_r^3\epsilon_0}|M_{10}|^2\frac{\sigma_s I}{[(E_{10}-\hbar\omega)^2+(\hbar\Gamma_0)^2]^2} \\ &\times\left[4(\varepsilon_{10}-\hbar\omega)|M_{10}|^2-\frac{(M_{11}-M_{00})^2}{E_{10}^2+(\hbar\Gamma_0)^2}\{(E_{10}-\hbar\omega)\right. \\ &\left.\times\left[E_{10}(E_{10}-\hbar\omega)-(\hbar\Gamma_0)^2\right]-(\hbar\Gamma_0)^2(2E_{10}-\hbar\omega)\}\right]\end{aligned} \tag{3.111}$$

and hereby total absorption coefficients and refractive index changes can be written below

$$\begin{aligned}\alpha(\omega,I) &= \alpha^{(1)}(\omega)+\alpha^{(3)}(\omega,I) \\ \Delta n(\omega,I)/n_r &= \frac{\Delta n^{(1)}(\omega)}{n_r}+\frac{\Delta n^{(3)}(\omega,I)}{n_r}\end{aligned} \tag{3.112}$$

where μ, ϵ_r and n_r indicate the permeability of the system, the real part of the permittivity and the refractive index of medium, respectively. c is the speed of the light and σ_s is the electronic density (Kilic et al., 2018). The incident optical intensity defined as I. The energy difference between the states represents E_{10} and the off-diagonal matrix elements of the dipole moment are $M_{ij} = |\langle\psi_i|er\cos\phi|\psi_j\rangle|$ $(i, j = 0, 1)$. The term $\Gamma_0 = 1/T_0$ corresponds to damping term associated with the lifetime of the electrons due to intersubband scattering (Kilic et al., 2017).

3.3.3 Third-Harmonic Generation

One of the most important optical properties in semiconductor nanostructures is the third-harmonic generation (THG) (Shao et al., 2011; Wang, 2015; Zhang et al., 2009). The third order nonlinear processes enable to expand the coherent light sources to shorter wavelengths, which creates an advantageous situation for optoelectronic devices to operate at shorter wavelengths (Maikhuri et al., 2015). This process brings about to the creation of a wave at frequency 3ω in response to an applied wave at frequency ω as shown in Figure 3.3 (Powers, 2013).

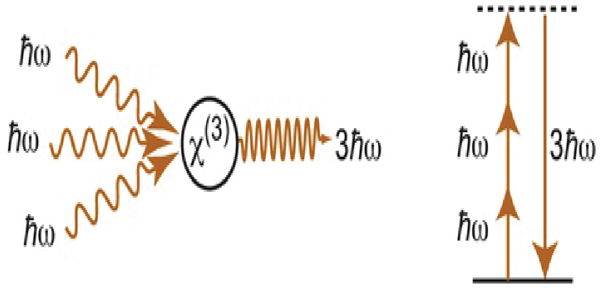

Figure 3.3 A schematic representation of third-harmonic generation process

By using Equation 3.106 expanded for a four-level system, the analytical expression of the THG coefficient can be achieved as following (Mohammadi et al., 2016):

$$\chi^{(3)}_{3\omega} = \frac{\rho}{\epsilon_0} \frac{M_{01}M_{12}M_{23}M_{30}}{(\hbar\omega - E_{10} - \mathrm{i}\hbar\Gamma_0)(2\hbar\omega - E_{20} - \mathrm{i}\hbar\Gamma_0/2)(3\hbar\omega - E_{30} - \mathrm{i}\hbar E_0/3)}, \tag{3.113}$$

where the electronic density is denoted by ρ. The off-diagonal matrix elements of the dipole moment depicts $M_{ij} = |\langle\psi_j|er\cos\phi|\psi_i\rangle|$(i, j = 0,1,2,3) and the corresponding parameters for transition energies are displayed by $E_{k0} = E_k - E_0$ (k = 1,2,3) (Sakiroglu et al., 2018).

CHAPTER FOUR

FORMALISM

In this chapter, we briefly introduce the general formalism used in this work for a two-dimensional laser-driven quantum dot system with different impurity types considering the effect of static magnetic field.

4.1 The General Formalism of a Laser-Driven Quantum Dot with Impurity

We consider a system in which one electron moving confined in a laser-driven QD with on-center impurity and subjected a static magnetic field along the z-axis.

Firstly, the Hamiltonian for such a system can be written as follows

$$H = \frac{1}{2m^*}\left(\vec{p} + e\vec{A}\right)^2 + V_{dConf}(|\vec{r}|) + V_{dImp}(|\vec{r}|) \tag{4.1}$$

where m^*, e, $\vec{A}$ are the electron effective mass, charge and the vector potential of the magnetic field. $V_{dConf}(|\vec{r}|, \alpha_0)$ and $V_{dImp}(|\vec{r}|, \alpha_0)$ are the laser-dressed confinement and impurity potential, respectively.

For the solution such a system subjected to an uniform external magnetic field , the time-independent Schrödinger equation is written again

$$H\varphi(r,\phi,z) = E\varphi(r,\phi,z) \tag{4.2}$$

$$\left(\frac{1}{2m^*}\left(\vec{p} + e\vec{A}\right)^2 + V_{dConf}(r,\alpha_0) + V_{dImp}(r,\alpha_0)\right)\varphi(r,\phi,z) = E\varphi(r,\phi,z) \tag{4.3}$$

$$-\frac{\hbar^2}{2m^*}\nabla^2\varphi - \frac{ie\hbar}{2m^*}\left(\vec{\nabla}\cdot(\vec{A}\varphi) + \vec{A}\cdot(\vec{\nabla}\varphi)\right) + \frac{e^2A^2}{2m^*}\varphi + \left(V_{dConf}(r,\alpha_0) + V_{dImp}(r,\alpha_0)\right)\varphi = E\varphi \tag{4.4}$$

$$\vec{\nabla}\cdot(\vec{A}\varphi) = (\vec{\nabla}\cdot\vec{A})\varphi + \vec{A}\cdot(\vec{\nabla}\varphi)$$

$$-\frac{\hbar^2}{2m^*}\nabla^2\varphi-\frac{ie\hbar}{2m^*}\left(2\vec{A}\cdot(\vec{\nabla}\varphi)+(\vec{\nabla}\cdot\vec{A})\varphi\right)+\frac{e^2A^2}{2m^*}\varphi+\left(V_{dConf}(r,\alpha_0)+V_{dImp}(r,\alpha_0)\right)\varphi=E\varphi \tag{4.5}$$

where $\vec{A}$ must satisfy the relations $\vec{\nabla}\cdot\vec{A}=0$ and $\vec{B}=\vec{\nabla}\times\vec{A}$ where $\vec{B}$ is the external magnetic field. With the symmetric gauge, $\vec{A}(r)=(\vec{A}_r=0,\vec{A}_\phi=Br/2,\vec{A}_z=0)$

$$\left(-\frac{\hbar^2}{2m^*}\nabla^2-\frac{ie\hbar}{2m^*}B\frac{\partial}{\partial\varphi}+\frac{e^2B^2r^2}{8m^*}+\left(V_{dConf}(r,\alpha_0)+V_{dImp}(r,\alpha_0)\right)\right)\varphi=E\varphi \tag{4.6}$$

By remembering, $\mathbf{L}_z=(\mathbf{r}\times\mathbf{p})_z$ is the z-component of the angular momentum $L_z=\frac{\hbar}{i}\frac{\partial}{\partial\phi}$

$$\left(-\frac{\hbar^2}{2m^*}\nabla^2+\frac{eB}{2m^*}L_z+\frac{e^2B^2r^2}{8m^*}+\left(V_{dConf}(r,\alpha_0)+V_{dImp}(r,\alpha_0)\right)\right)\varphi=E\varphi \tag{4.7}$$

Laplace operator in cylindrical coordinates:

$$\nabla^2=\frac{1}{r}\frac{\partial}{\partial r}\left(r\frac{\partial}{\partial r}\right)+\frac{1}{r^2}\frac{\partial^2}{\partial\phi^2}+\frac{\partial^2}{\partial z^2} \tag{4.8}$$

We assume that one electron is much more strongly confined in one direction (taken as the z direction) than in the other two directions and so electron merely moves in the (x,y) plane and this expression in the equation for $z=0$ becomes

$$\left(-\frac{\hbar^2}{2m^*}\left(\frac{1}{r}\frac{\partial}{\partial r}\left(r\frac{\partial}{\partial r}\right)+\frac{1}{r^2}\frac{\partial^2}{\partial\phi^2}\right)+\frac{eB}{2m^*}L_z+\frac{e^2B^2r^2}{8m^*}+\left(V_{dConf}(r,\alpha_0)+V_{dImp}(r,\alpha_0)\right)\right)\varphi=E\varphi \tag{4.9}$$

The wave function $\varphi(r,\phi,0)$ can be written as

$$\varphi(r,\phi,0)=R(r)\Phi(\phi) \tag{4.10}$$

where using $L_z\Phi(\phi)=m\hbar\Phi(\phi)$ and $\Phi(\phi)=e^{im\phi}/\sqrt{2\pi}$, then for the radial part we obtain

$$\left(-\frac{\hbar^2}{2m^*}\left(\frac{1}{r}\frac{d}{dr}\left(r\frac{d}{dr}\right)-\frac{m^2}{r^2}\right)+\frac{eB}{2m^*}m\hbar+\frac{e^2B^2r^2}{8m^*}+\left(V_{dConf}(r,\alpha_0)+V_{dImp}(r,\alpha_0)\right)\right)R(r)$$

$$=\quad E\,R(r) \tag{4.11}$$

To scale the Schrödinger equation, we select $\tilde{r} = r/a_0^*$, $\tilde{E} = E/E_h^*$, $\tilde{V}_{dConf} = V_{dConf}/E_h^*$, $\tilde{V}_{dImp} = V_{dImp}/E_h^*$ and we introduce $\omega_c = eB/m^*$ and $\gamma_c = \hbar\omega_c/E_h^*$. Using the above arrangements, we get

$$\left(-\frac{1}{2}\left(\frac{d^2}{dr^2} + \frac{1}{r}\frac{d}{dr} - \frac{m^2}{r^2}\right) + \frac{m\gamma_c}{2} + \frac{1}{8}\gamma_c^2 r^2 + V_{dConf}(r,\alpha_0) + V_{dImp}(r,\alpha_0)\right) R(r) = E\,R(r) \tag{4.12}$$

where we removed "~" for simplicity.

The Schrödinger equation becomes

$$\left(-\frac{1}{2}\frac{1}{r}\left(\frac{d}{dr}r\frac{d}{dr}\right) + \frac{m^2}{2r^2} + \frac{m\gamma_c}{2} + \frac{1}{8}\gamma_c^2 r^2 + V_{dConf}(r,\alpha_0) + V_{dImp}(r,\alpha_0)\right) R(r) = E\,R(r) \tag{4.13}$$

By using FEM in one dimension, we have carried out numerical solution of Equation 4.13

It should be noted here that we did not include the influence of ILF on the diamagnetic term in the Equation 4.11. Because, we have assumed a system including ILF-modulated potentials that is exposed to a static magnetic field. However, the recent article published by Vinasco et al. (Vinasco et al., 2019) has investigated that the effect of ILF on the diamagnetic term. Inclusion of this effect brings a contribution of $V_{dB} = e^2B^2\alpha_0^2/8m^*$ that can be a subject of further work.

CHAPTER FIVE
NUMERICAL RESULTS

In this chapter, we present the numerical results of the influences of ILF on the electronic and optical properties of 2DQD system considering different impurity types such as Gaussian, Hydrogenic and Screened Coulomb. Here, it should be noted that the notation of each section is different for the presented results.

5.1 Impurity-related optical properties of a laser-driven quantum dot

5.1.1 Introduction

In the past decades, owing to their potential applications in microelectronic and optoelectronic devices, the low-dimensional structures such as quantum wells, quantum wires and quantum dots (QDs) have been extremely investigated. QDs, where the motion of the charge carriers is restricted in all directions, have the formation of atomic-like discrete energy levels (subbands) which are adaptable for a specific need by changing the size, shape and compositional materials of the dot (Kilic et al. (2018) and references therein). A number of research concerning the linear and nonlinear optical absorption coefficients and relative changes in refractive index have been broadcasted reporting the large dipole matrix elements and the small energy separation between subbands in QDs (Gambhir et al., 2013; Li et al., 2016; G. Liu, 2012). Intersubband related optical properties in a parabolic cylinder quantum dot have been obtained in Ref (Vahdani & Rezaei, 2010). The nonlinear optical absorption coefficients and refractive index changes in an asymmetric semiconductor quantum dot structure under a strong probe field excitation have been studied by Paspalakis et al. (Paspalakis et al., 2013). Cakir et al. have investigated the linear and nonlinear absorption coefficients of spherical quantum dot inside external magnetic field (Cakir et al., 2017).

Impurities or donor scattering centers, which gives rise to a change in the electronic and optical properties of QDs, play a vital role in semiconductor devices (Bejan, 2016b; Yuan et al., 2014). Since the understanding of effects of impurity is a very useful task because of optimizing the performance of the optoelectronic devices (Shojaei & Vala, 2015). Therefore, many number of studies on their effects have been reported (Kasapoglu et al., 2011; Lu & Xie, 2011; Räsänen et al., 2004). In an attempt to describing of impurity potential in QDs, generally two models are used: hydrogenic impurity and Gaussian impurity. While there are lots of investigations on the hydrogenic impurity, few studies with Gaussian impurity are situated in literature (Hosseinpour et al., 2016). Baskoutas et al. have examined the effects of impurities and external electric field on the electronic structure and nonlinear optical rectification in a quantum dot (Baskoutas et al., 2007). The nonlinear optical rectification coefficient of quantum dots and rings with a repulsive scattering center has been reported by (Xie, 2013b). The donor impurity-related optical absorption coefficients and refractive index changes in a rectangular GaAs quantum dot in the presence of electric field are studied by Sheng et al. (Sheng et al., 2016). Bera et al. have researched the modulation of electro-optic effect and the third-order nonlinear optical susceptibility of impurity doped quantum dot in presence of noise (Bera et al., 2016). The effects of the Kratzer potential, external electric and magnetic fields upon the electronic structure of a spherical quantum dot with hydrogenic impurity (Dehyar et al., 2016). The effect of impurities on linear and nonlinear absorption coefficient and refractive index of the spherical quantum dot four-level M-model the phenomenon of electromagnetically induced transparency have been examined by Damiri and Askari (Damiri & Askari, 2017). Mikhail and Shafee have investigated the optical absorption in a disc-shaped quantum dot in the presence of an impurity (Mikhail & Shafee, 2017).

On the other hand, intensive research has been conducted reporting the significant effects of intense high-frequency laser field (ILF) on electronic states and optical properties of GaAs-based semiconductor bulk and related QDs (Kilic et al. (2018) and references therein). The ability to adjust the energy spectrum to produce the desired optical transitions is one of the most important result of the laser beam action. The effects of intense laser radiation on the binding energy of on- and off- center hydrogenic impurities in a parabolic quantum dot subjected to an intense high-frequency laser field has been studied by Santander et al. (Gonzalez-Santander et al., 2013). Burileanu has researched the influence of electric and laser fields on the behavior of the binding energy and photoionization cross-section of a donor impurity in spherical quantum dot (Burileanu, 2014). Safarpour et al. have investigated the optical properties of a spherical quantum dot confined in a cylindrical nanowire subjected to laser radiation field (Safarpour et al., 2014).

As far as we know, the effect of the presence of an on-center Gaussian impurity on the optical properties of a laser-driven parabolic quantum dot system under an uniform external magnetic field has not been investigated so far. Hereby, we will focus on the linear and nonlinear optical absorption coefficients and refractive index changes in the two-dimensional parabolic quantum dot exposed to a non-resonant, high-frequency intense laser field. The paper is organized as follows: In Sec. 5.1.2, the theoretical model is described. Sec. 5.1.3 exposes the numerical results.

5.1.2 Theory

We consider an electron confined in a two-dimensional parabolic quantum dot under the influence of a static magnetic field by taking into account the presence of an on-center, attractive Gaussian impurity. We subject the system to the action of an intense laser field, represented by a right hand circularly polarized plane wave of frequency Ω. Within the framework of the high-frequency Floquet theory, the electron motion in quantum dot is specified by the time-averaged laser-dressed potential, $\langle V_d(\mathbf{r},\alpha_0)\rangle = \frac{1}{T}\int_0^T V(\mathbf{r}+\boldsymbol{\alpha}(t))dt$, where $T = 2\pi/\Omega$ is the period of a high-frequency, non-resonant intense laser field. The vector $\boldsymbol{\alpha}(t)$ is related to the vector potential of the radiation through, $\boldsymbol{\alpha}(t) = \int^t \boldsymbol{A}(t')dt'$, so we have $\boldsymbol{\alpha}(t) = \alpha_0(\hat{x}\cos\Omega t + \hat{y}\sin\Omega t)$, where $\hat{x}$ and $\hat{y}$ define the unit vectors orthogonal to the direction of propagation. $\alpha_0 = eA_0/m^*\Omega$ is called the laser-dressing parameter which stands for the excursion amplitude of the particle in its quiver motion in the laser field (Pont & Gavrila, 1990) .

Via the adopted approach for the inclusion of ILF-effects whose details are available in elsewhere (Barseghyan et al., 2017; Enders et al., 2004; Kilic et al., 2017), the analytical expressions for the laser-dressed form of parabolic potential and Gaussian impurity (Durak, 2015; Halonen et al., 1996b) are obtained as:

$$\langle V_{dP}(r,\alpha_0)\rangle = \frac{1}{2}m^*\omega_0^2\left(r^2+\alpha_0^2\right) \tag{5.1}$$

$$\langle V_{dG}(r,\alpha_0)\rangle = -V_0\ exp\left(-\frac{r^2+\alpha_0^2}{d^2}\right)I_0\left(\frac{2r\alpha_0}{d^2}\right). \tag{5.2}$$

Here r contains x and y coordinates, m^* is electronic effective mass, ω_0 represents the confinement frequency. Impurity is defined with a depth of V_0 and a range of d and $I_0(x)$ stands for the modified Bessel function.

Then the Hamiltonian of the laser-driven system subjected to an uniform magnetic field can be expressed as

$$H = \frac{1}{2m^*}(\mathbf{p}+e\mathbf{A})^2 + \langle V_{dP}(r,\alpha_0)\rangle + \langle V_{dG}(r,\alpha_0)\rangle \tag{5.3}$$

where e is the electron charge and $\mathbf{A}(\hat{r},\hat{\phi},\hat{z}) = (0, Br/2, 0)$ is the vector potential corresponding to the magnetic field chosen along the z-direction.

The laser-dressed eigen energies and eigen functions are obtained from the solution of time-independent Schrödinger equation in polar coordinates:

$$\begin{aligned} -\frac{\hbar^2}{2m^*}\left[\frac{1}{r}\frac{\partial}{\partial r}\left(r\frac{\partial}{\partial r}\right)+\frac{1}{r^2}\frac{\partial^2}{\partial\phi^2}\right]\psi + \frac{eB}{2m^*}L_z\psi \\ +\frac{e^2B^2r^2}{8m^*}\psi + (\langle V_{dP}(r,\alpha_0)\rangle + \langle V_{dG}(r,\alpha_0)\rangle)\psi = E\psi\ , \end{aligned} \tag{5.4}$$

where $L_z = \frac{\hbar}{i}\frac{\partial}{\partial\phi}$ is the z-component of angular momentum. Because of the axial symmetry of the system, the wave function $\psi(r,\phi)$ can be written as follows

$$\psi(r,\phi) = R(r)\Phi(\phi) = R(r)\frac{e^{im\phi}}{\sqrt{2\pi}} \tag{5.5}$$

which leads to $L_z\Phi(\phi) = m\hbar\Phi(\phi)$ and m being the magnetic quantum number. With a choice of effective Bohr radius a_0^* and effective Hartree energy $E_H^* = \hbar^2/m^* a_0^{*2}$ as the length and energy scales, respectively, Eq. (5.15) reads to

$$\begin{aligned}&\left[-\frac{1}{2}\frac{1}{r}\frac{d}{dr}r\frac{d}{dr}+\frac{m^2}{2r^2}+\frac{m\gamma_c}{2}+\frac{1}{8}\gamma_c^2 r^2\right.\\&\left.+\langle V_{dP}(r,\alpha_0)\rangle+\langle V_{dG}(r,\alpha_0)\rangle\right]R(r)=ER(r)\,.\end{aligned} \tag{5.6}$$

Here the dimensionless magnetic field is defined by $\gamma_c = \hbar\omega_c/E_H^*$ with cyclotron frequency of $\omega_c = eB/m^*$. In order to achieve the eigen energies and corresponding wave functions, numerical calculations have been performed by using finite element method (Pask et al., 2001).

In this study, the energy levels and the wave functions participating in the transition are chosen as follow

$$E_0 = E_{00}, \qquad E_1 = E_{11}, \qquad \psi_0 = \psi_{00}, \qquad \psi_1 = \psi_{11}\ .$$

The optical characteristics for the intersubband transitions are deduced from the compact density matrix approach and iterative scheme, where the total optical absorption coefficient is written as a sum of the linear and third-order nonlinear contributions, respectively (Rezaei et al., 2010):

$$\alpha(\omega,I) = \alpha^{(1)}(\omega) + \alpha^{(3)}(\omega,I)\,, \tag{5.7}$$

$$\alpha^{(1)}(\omega) = \omega\sqrt{\frac{\mu}{\varepsilon_r}}\frac{\sigma_s|M_{10}|^2\hbar\Gamma_0}{(E_{10}-\hbar\omega)^2+(\hbar\Gamma_0)^2} \tag{5.8}$$

$$\begin{aligned}\alpha^{(3)}(\omega,I) \;&=\; -\omega\sqrt{\frac{\mu}{\epsilon_r}}\left(\frac{I}{2n_r\epsilon_0 c}\right)\frac{\sigma_s\hbar\Gamma_0|M_{10}|^2}{[(E_{10}-\hbar\omega)^2+(\hbar\Gamma_0)^2]^2}\\&\times\left\{4|M_{10}^2|-|M_{11}-M_{00}|^2\times\frac{\left[3E_{10}^2-4\varepsilon_{10}\hbar\omega+\hbar^2(\omega^2-\Gamma_0^2)\right]}{E_{10}^2+(\hbar\Gamma_0)^2}\right\}.\end{aligned} \tag{5.9}$$

Here μ is the permeability of the system, I is the intensity of the incident probe electromagnetic field, n_r is the refractive index of medium, c is the speed of the light, σ_s is the electronic density, E_{10} is the energy difference between the states, $M_{ij} = |\langle\psi_i|er\cos\phi|\psi_j\rangle|$ $(i, j = 0,1)$are the off-diagonal matrix elements of the dipole moment and $\Gamma_0 = 1/T_0$ is damping term associated with the lifetime of the electrons due to intersubband scattering (Mora-Ramos et al., 2012a).

The linear and the third-order nonlinear relative refractive index changes are expressed as, respectively (Li et al., 2012):

$$\frac{\Delta n^{(1)}(\omega)}{n_r} = \frac{1}{2n_r^2\varepsilon_0}|M_{10}|^2\sigma_s\left[\frac{E_{10}-\hbar\omega}{(E_{10}-\hbar\omega)^2+(\hbar\Gamma_0)^2}\right] \tag{5.10}$$

and

$$\begin{aligned}\frac{\Delta n^{(3)}(\omega,I)}{n_r} &= -\frac{\mu c}{4n_r^3\epsilon_0}|M_{10}|^2\frac{\sigma_s I}{[(E_{10}-\hbar\omega)^2+(\hbar\Gamma_0)^2]^2} \\ &\quad\times\Bigg[4(\varepsilon_{10}-\hbar\omega)|M_{10}|^2-\frac{(M_{11}-M_{00})^2}{E_{10}^2+(\hbar\Gamma_0)^2}\{(E_{10}-\hbar\omega) \\ &\quad\times\left[E_{10}(E_{10}-\hbar\omega)-(\hbar\Gamma_0)^2\right]-(\hbar\Gamma_0)^2(2E_{10}-\hbar\omega)\}\Bigg]\end{aligned} \tag{5.11}$$

The total magnitude of the relative change in the refractive index $\Delta n(\omega,I)/n_r$ constitutes from the contributions given in Eqs. (5.33) and (5.34).

5.1.3 Results and discussion

In this section we present our calculations for the impurity-related optical absorption and refractive index change in GaAs quantum dot described by a two-dimensional parabolic potential considering the effects of ILF and static magnetic field. The parameters used in our calculations are: $\sigma_s = 5\times10^{24}$ m^{-3}, $\Gamma_0 = 1/0.14$ ps, $\varepsilon_r = 12.53$, $m^* = 0.067m_0$ (where m_0 is the free electron mass), $\mu = 4\pi\times10^{-7}$ Hm^{-1}, $n_r = 3.2$ and $I = 1.5\times10^{10}$ W/m^2 (Duque et al., 2012a; Xie, 2013b).

The impurity binding energy is defined as $E_b = E^0 - E$, where E^0 is the ground state energy in the absence of impurity. Figure 5.1 (a) displays the binding energy of Gaussian impurity as a function of laser-dressing parameter for three values of confinement strength $\hbar\omega_0$ and impurity parameter d (inset). Applying an ILF on the system, results in widening of the effective width of the impurity potential and shallowing in its depth. Consequently, it's obviously seen that the binding energy reduces with increasing α_0 for both considered parameters. The physical origin of this behavior is the spreading of the wave function and accordingly the reduction in the probability of finding an electron in the dot. This situation leads to a lesser binding of the donor electron. Besides, it's also important to notice that the magnitude of the binding energy enhances for stronger values of $\hbar\omega_0$ and d. Figure 5.1 (b) demonstrates the dependence of confinement potential on the binding energy by considering a laser field with α_0 = 2 nm for three values of magnetic field where the inset shows the variation for the impurity range parameter d. As can be seen, as a consequence of squeezing of the wave function in a small space, the binding energy exhibits an increasing behavior for higher values of $\hbar\omega_0$. Similar to Figure 5.1 (a), the higher B or d is, the stronger binding energy is.

In an effort to understand the general behavior of optical response of system, we depict the effects of laser-dressing parameter on the absolute value of dipole matrix

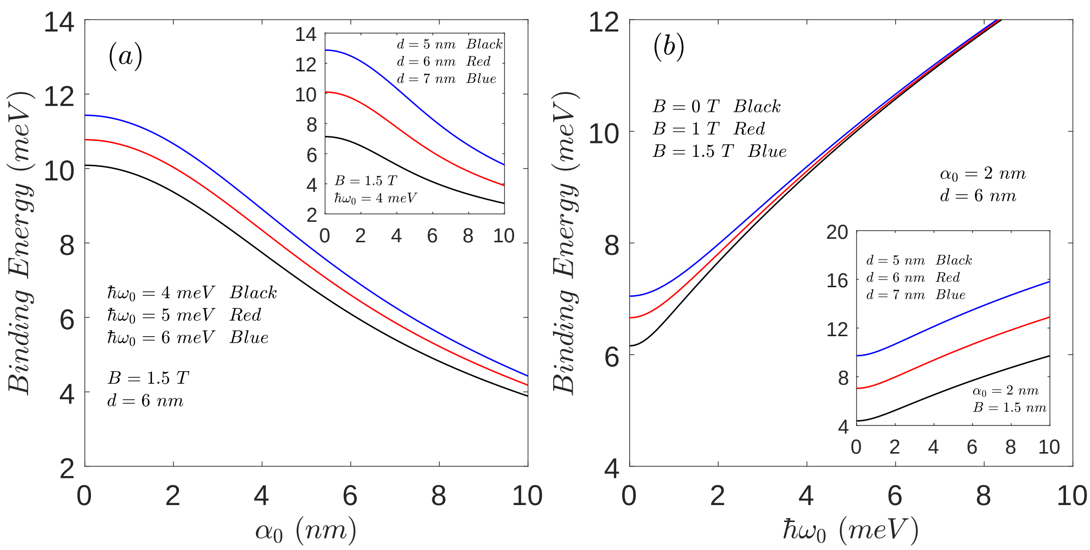

Figure 5.1 The impurity binding energy as a function of (a) α_0 for three values of $\hbar\omega_0$ and d, (b) the confinement strength $\hbar\omega_0$ for different values of and B and d

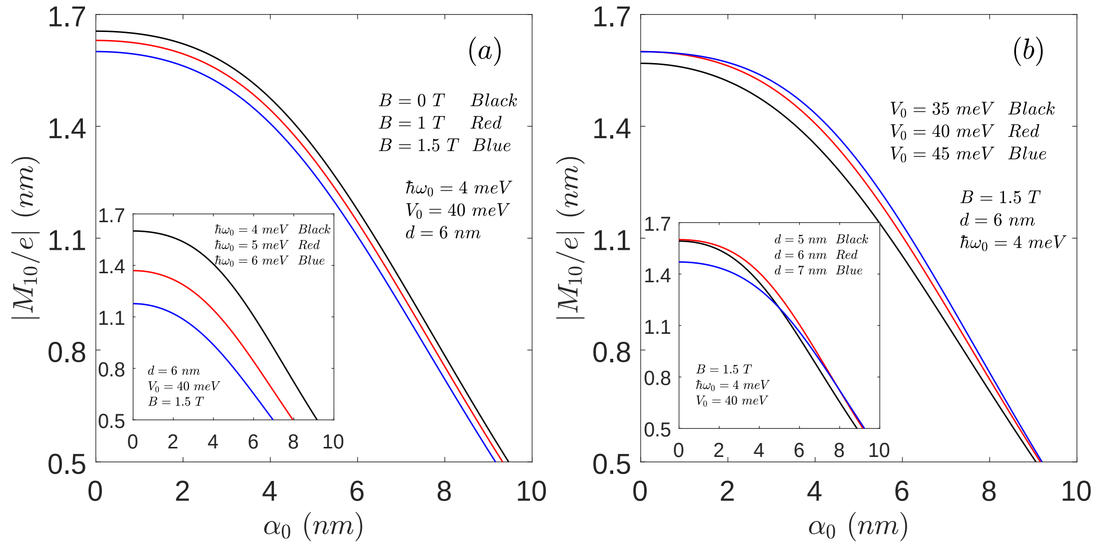

Figure 5.2 The absolute value of dipole matrix element as a function of laser-dressing parameter (a) for different values of B and $\hbar\omega_0$, (b) for three values of impurity parameters V_0 and d

element in Figure 5.2 (a) and (b). Both figures indicate a decline in the magnitude of $|M_{10}|$ for higher values of α_0-parameter. Figure 5.2 (a) reveals that the enhancement in confinement of the electron due to dot potential or magnetic field brings about a decrease in the dipole matrix elements. The effects of impurity potential parameters on the dipole matrix element are demonstrated in Figure 5.2 (b). We can clearly see that the absolute value of dipole matrix element is greater for higher V_0 value while its variation with impurity range parameter is a bit different. For the chosen parameter set (V_0 = 40 meV, B = 1.5 T, $\hbar\omega_0$ = 4 meV), we observe a greater $|M_{10}|$ for d = 6 nm (inset of Figure 5.2 (b)) for almost all laser-dressing parameter range.

Another important factor that acts on the optical coefficients is the transition energy defined as the difference between the ground and first excited states, $E_{10} = E_1 - E_0$. Therefore, we demonstrate the effects of intense laser field upon the transition energy in Figure 5.3 (a) and (b). As it can be seen from Figure 5.3 (a) and (b), higher values of B, d, V_0 and $\hbar\omega_0$ lead to higher transition energies. In addition, we evidently observe from both figures that the transition energy reduces with increasing α_0 which give cause to a weakening in confinement. We also should note that the intense laser radiation predominantly acts on the ground state energy level.

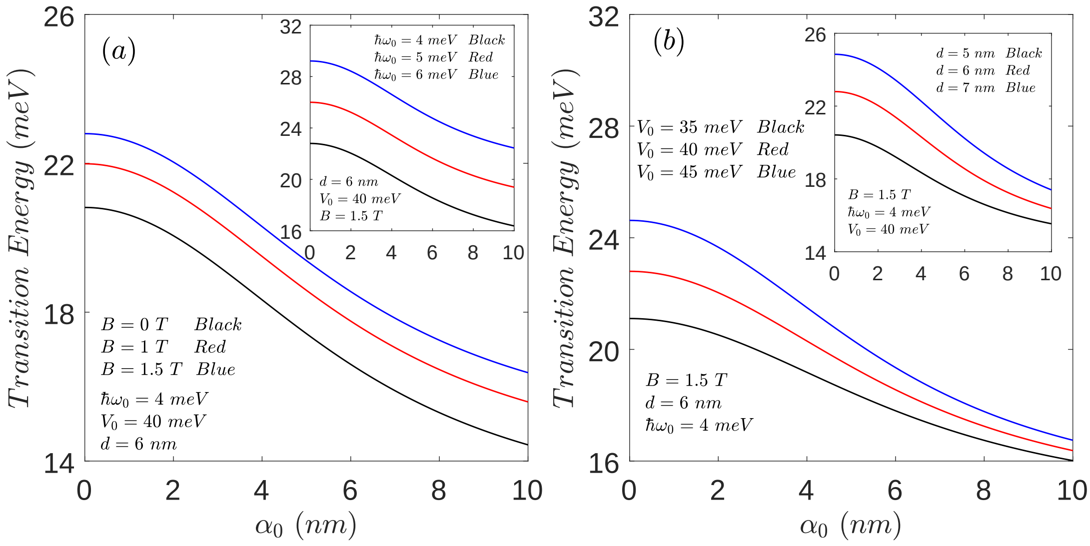

Figure 5.3 The transition energy versus laser-dressing parameter (a) for different values of B and $\hbar\omega_0$, (b) for three values of V_0 and d

Now, it is noteworthy to exhibit the effects of intense laser field on the linear and nonlinear optical absorption coefficients and refractive index changes for a system under debate. Linear, third-order nonlinear and total value of the optical coefficients are represented by dashed, dotted and solid lines, respectively. From Figure 5.4 (a) and (b), it is readily seen that as the laser-dressing parameter increases, the peaks of absorption coefficient and refractive index changes shift to the lower energy region. The underlying cause of this red-shift can be explained by the decrease in transition energy. Moreover, in both figures amplitudes of the resonance peaks decreases considerably for stronger laser field strengths in accordance with the decrease observed in matrix elements.

In order to expose the effect of external magnetic field on the optical characteristics of the system, in Figure 5.5 (a) and (b) we plot the absorption coefficients and refractive index changes as a function of incident photon energy for three values of magnetic field. Laser field-induced blue-shift in the peaks of optical coefficients is based on improvement energy difference between the E_0 and E_1. For increasing B, the magnitude of total absorption coefficient enhances while the magnitude of total refractive index change declines as seen in Figure 5.5 (a) and Figure 5.5 (b), respectively. Underlying fact of this case is the competition between the factors E_{10}

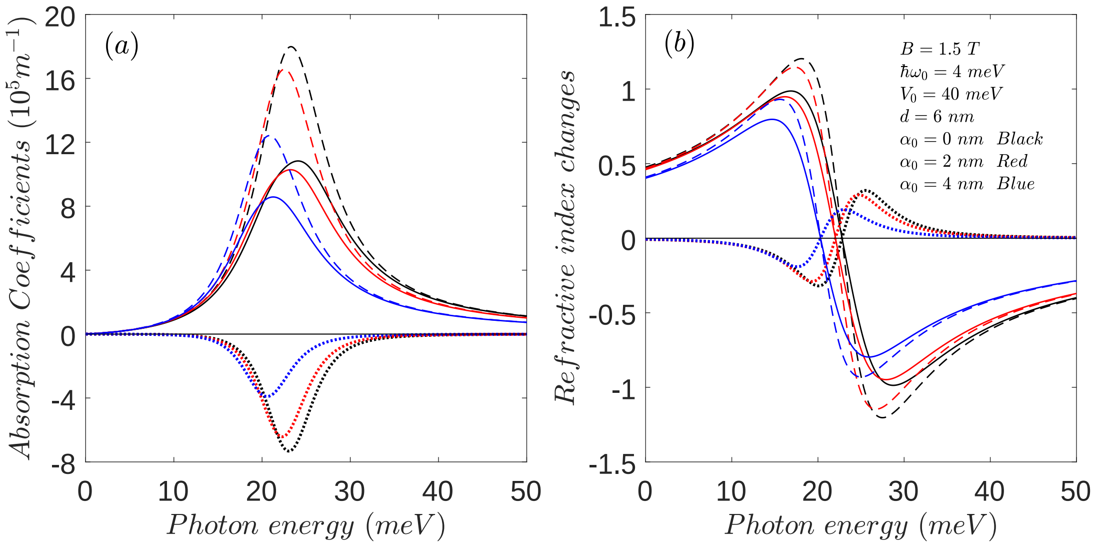

Figure 5.4 The linear, nonlinear and total (a) optical absorption coefficients and (b) refractive index changes as a function of the energy of incident photon for three values of α_0. We use V_0 = 40 meV, B = 1.5 T, $\hbar\omega_0$ = 4 meV and d = 6 nm

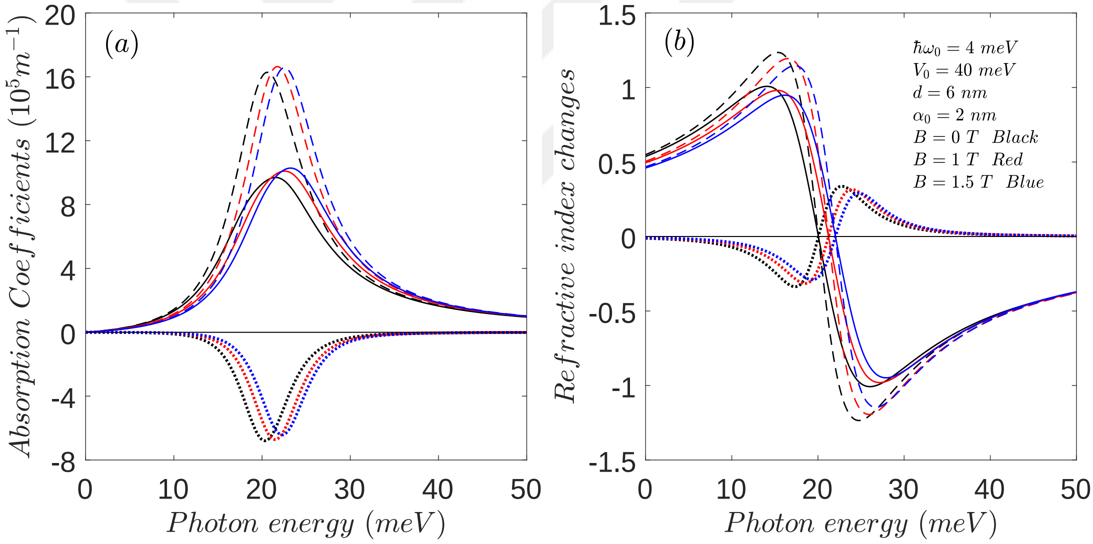

Figure 5.5 The linear, nonlinear and total (a) optical absorption coefficients and (b) refractive index changes versus the photon energy for different values of magnetic field. The system is defined by V_0 = 40 meV, $\hbar\omega_0$ = 4 meV and d = 6 nm where the laser-dressing parameter is set to α_0 = 2 nm

and M_{10} which determine behavioral act of the optical characteristics.

It's important to demonstrate how impurity-related parameters impact the optical response of the system. In line of this purpose, the linear, third-order nonlinear and the total optical absorption coefficients and refractive index changes as a function of incident photon energy are presented in Figure 5.6 (a) and (b), respectively for

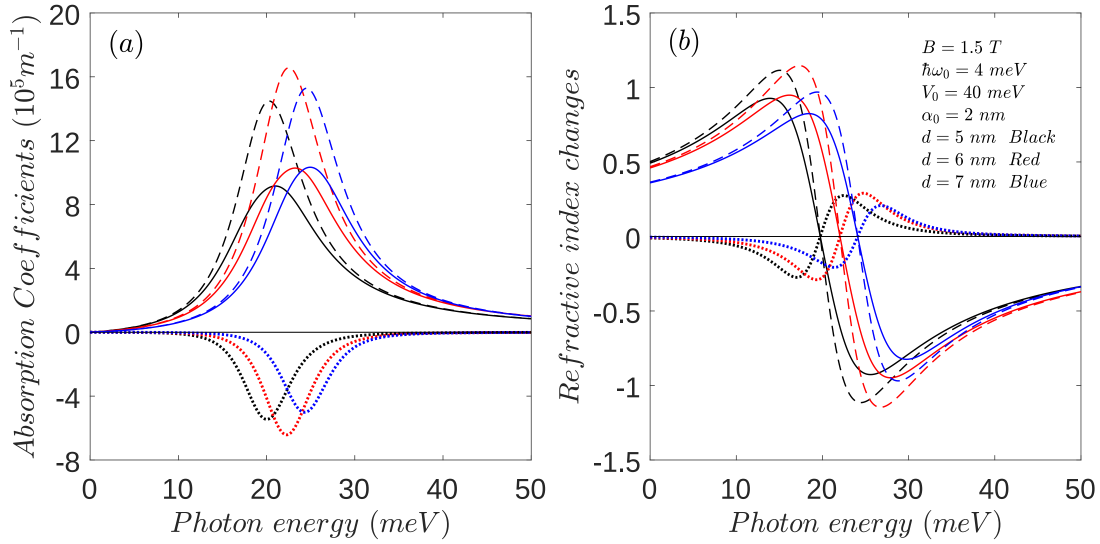

Figure 5.6 Variation of the linear, third-order nonlinear and the total (a) optical absorption coefficients and (b) refractive index changes as a function of the photon energy with varying values of d. We set V_0 = 40 meV, B = 1.5 T, $\hbar\omega_0$ = 4 meV and α_0 = 2 nm

varying values of d. Increment in range parameter leads to an increase (decrease) in the amplitude of the resonance peak of the optical absorption coefficients (the refractive index changes) while positions of the peaks are blue-shifted. It should be noted here that the maximum peaks magnitudes occur for $d =$ 6 nm which is compatible with the inset of Figure 5.2

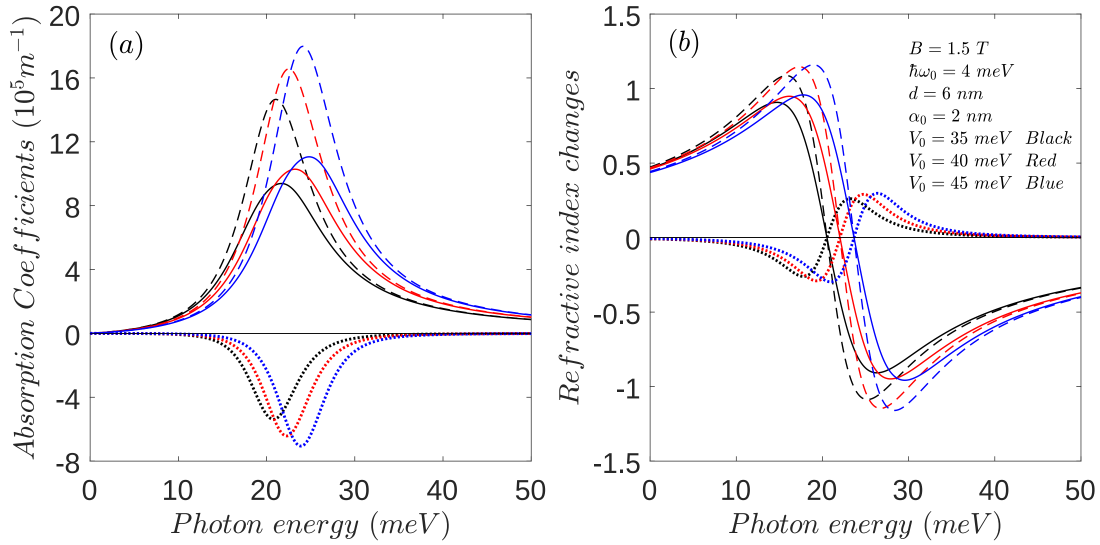

Figure 5.7 The linear, nonlinear and total (a) optical absorption coefficients and (b) refractive index changes as a function of incident photon energy for different values of V_0

Figure 5.7 (a) and (b) illustrates the dependence of the optical coefficients on the

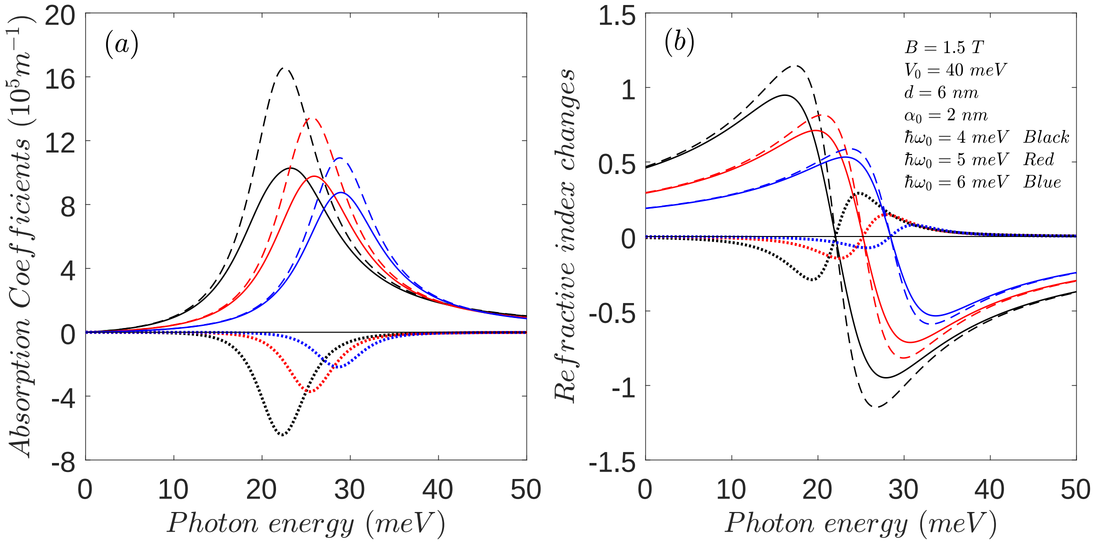

Figure 5.8 The linear, nonlinear and total (a) optical absorption coefficients and (b) refractive index changes as a function of incident photon energy for different values of $\hbar\omega_0$ with d = 6 nm, B = 1.5 T, V_0 = 40 meV and α_0 = 2 nm

depth of on-center Gaussian impurity. The peak positions of the linear and nonlinear optical absorption coefficients and refractive index changes shift to right-side and the peak magnitudes increase for the higher values of V_0. The physical reason for this important feature is that as V_0 increases, the energy difference between the first two lower-lying energy levels and the matrix element increases as seen from Figure 5.3 (b) and Figure 5.1 (b).

Another parameter that fairly affects the optical response of the system is $\hbar\omega_0$. The resonance peaks of the optical absorption coefficients and refractive index changes move to the higher energy values for increasing $\hbar\omega_0$ as seen in Figure 5.8 (a) and (b), which arises due to the ascending in transition energy. Besides, increment in $\hbar\omega_0$ gives rise to a significant reduction in peak magnitudes owing to decreasing in the absolute value of dipole matrix element.

So as to carry out the exhaustive exploration of the ILF- and structure parameters-induced changes in the peak amplitude of total optical absorption coefficient and refractive index change, we present the variations of the peak value of total optical absorption coefficient and refractive index change at resonance frequency as a function of α_0 in Figure 5.9 and Figure 5.10.

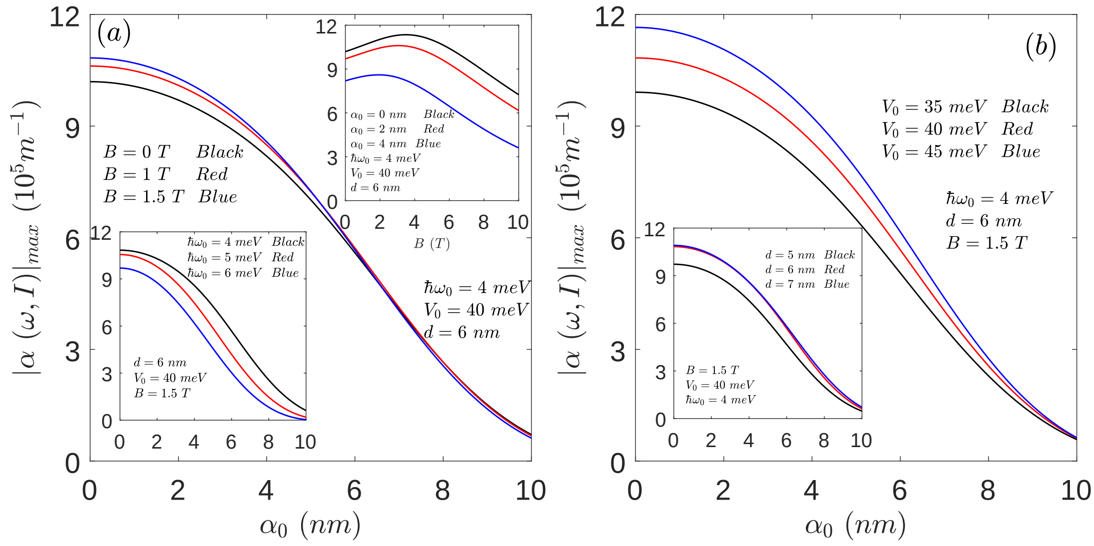

Figure 5.9 The resonant peak value of total optical absorption coefficient as a function of laser-dressing parameter for (a) different values of B and $\hbar\omega_0$, (b) for three values of V_0 and d

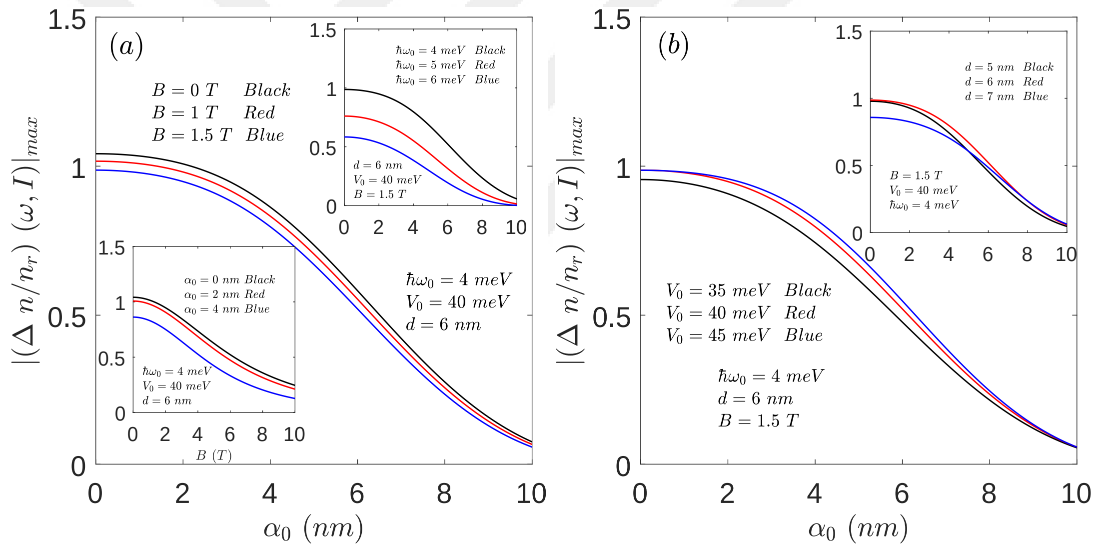

Figure 5.10 The maximum value of total refractive index change as a function of incident photon energy for (a) different values of B and $\hbar\omega_0$, (b) for three values of V_0 and d

From both figures, it is obviously seen that the maximum of total optical absorption coefficient and refractive index change decreases at higher laser field values. The resonant peak value of total optical absorption coefficient is greater for higher (smaller) values of B ($\hbar\omega_0$) as seen in Figure 5.9 (a). Besides, the upper inset of Figure 5.9 (a) shows that the initial increase in the peak amplitude of the total absorption coefficient is followed by a decrease for higher magnitudes of external magnetic field and is suppressed by the increase in the laser intensity. On the other hand, Figure 5.9 (b) exhibits that the maximum of total optical absorption coefficient is achieved for greater V_0 and d. The Figure 5.10 (a) shows that the resonant peak value of total refractive index change enhances for smaller values of B and $\hbar\omega_0$. Lower inset reveals the fact that the augmentation in magnetic field leads to lowering in the laser-induced relative refractive index changes. In Figure 5.10 (b), it can be clearly seen that the maximum value of refractive index change is greater for higher V_0 value and the highest resonant peak value refractive index change is obtained for d = 6 nm (upper inset of Figure 5.10 (b)).

5.2 Third-harmonic generation of a laser-driven quantum dot with impurity

5.2.1 Introduction

Recent advances in crystal growth technology have provide a facility for the fabrication of low-dimensional semiconductor structures such as quantum dots(QDs), quantum wires and quantum wells (Knoss, 2009). QDs, in which the motion of the electron is quantized in all three spatial directions, display phenomena reminiscent of atoms owing to resemblance of the electronic properties and so they are generally referred as artificial atoms (Tarucha et al., 1998). Furthermore, the nonlinear optical properties of QDs find a great number of applications in optoelectronic devices such as high-speed electro-optical modulators, far infrared photodetectors, semiconductor optical amplifiers (Bejan, 2016b; Chen et al., 2013). Among the nonlinear optical properties, Third-harmonic generation (THG) has gained special interest which became a subject of considerable amount of research (Sakiroglu et al. (2018) and references therein). The effect of electron-phonon interaction on THG in a double ring-shaped QD have been investigated by Khordad (Khordad, 2017). Shape effects in QDs on the third-harmonic generations have been examined by Li et al. (Li et al., 2017). Ganguly et al. have researched the electro-optic effect and third-order nonlinear optical susceptibility of impurity doped QDs under the combined influence of hydrostatic pressure and temperature. (Ganguly et al., 2017).

Since the electronic, optical and transport properties of quantum devices are strongly influenced by the presence of impurities, extensive works have been conducted on impurity-related effects in QDs ((Sakiroglu et al., 2018) and references therein). To define the potential of impurity in QDs, Gaussian-like and Hydrogenic-like potentials are generally used (Hosseinpour et al., 2016). The effects of impurities in two-dimensional QD have been studied by Räsänen et al. (Räsänen et al., 2004). Halonen et al. have researched the electron correlation effects in the QDs and rings with a repulsive scatterer (Halonen et al., 1996b). Xie has investigated the effects of repulsive Gaussian impurity on the nonlinear optical rectification coefficient in QDs and rings (Xie, 2013b). The third-harmonic generation susceptibility of QD with Gaussian impurity has been examined by Saha and Ghosh (Saha & Ghosh, 2016) considering the presence and absence of noise .

Recently, the improvement of high-power tunable laser sources has created new opportunities in attempt to research the interaction of carriers with electromagnetic radiation (Gonzalez-Santander et al., 2013; Laroze et al., 2016; Sakiroglu et al., 2017). Researches reveal that the intense laser field (ILF) considerably alters the electronic and optical properties of QDs because of its modulating effects on the potential profile (Burileanu, 2014; Safarpour et al., 2014). Niculescu has investigated the effects of electric and laser fields on the electromagnetically induced transparency mechanism in a GaAs disc-like QD with on-center hydrogenic impurity (Niculescu, 2017). The influence of intense laser and electric fields on the electronic structure and nonlinear optical properties of a GaAs asymmetric double QDs have been studied by Bejan et al. (Bejan, 2016a).

To the best of our knowledge, the effect of an on-center Gaussian impurity on the optical properties of a laser-driven parabolic QD system subjected to an uniform magnetic field has not been studied up to now. The presence of an impurity leads to alternation in the energy spectrum and the nonlinear optical properties in QDs. Therefore, the survey of the structure with adjustable optical transitions can be useful for development of optoelectronic devices. In the present work, we will focus on the third-harmonic generation of the two-dimensional QD subjected a non-resonant, high-frequency intense laser field. The rest of the paper is arranged as follows: In Sec. 5.2.2, the theoretical model is described. The numerical results of the system are presented in Sec. 5.2.3.

5.2.2 Theory

In this work, we consider one electron confined in a laser-driven QD with an on-center Gaussian impurity and subjected a static magnetic field. The intense laser field interacting with the system is considered as a right circularly polarized plane wave of frequency Ω. In the framework of the high-frequency Floquet theory, the time-averaged laser-dressed potential is given as $\langle V_d(\mathbf{r},\alpha_0)\rangle = \frac{1}{T}\int_0^T V(\mathbf{r}+\boldsymbol{\alpha}(t))dt$, where $T = 2\pi/\Omega$ is the period of a high-frequency ILF. The motion of the electron in the laser field is defined by $\boldsymbol{\alpha}(t) = \alpha_0(\hat{x}\cos\Omega t + \hat{y}\sin\Omega t)$ where the $\alpha_0 = eA_0/m^*\Omega$ is the laser-dressing intensity parameter (Lima et al., 2008; Pont & Gavrila, 1990). Then, the analytical expressions for the laser-dressed form of parabolic confinement potential and Gaussian impurity (Durak, 2015; Halonen et al., 1996b) are obtained as:

$$\langle V_{dP}(r,\alpha_0)\rangle = \frac{1}{2}m^*\omega_0^2\left(r^2+\alpha_0^2\right) \tag{5.12}$$

$$\langle V_{dG}(r,\alpha_0)\rangle = -V_0\ exp\left(-\frac{r^2+\alpha_0^2}{d^2}\right)I_0\left(\frac{2r\alpha_0}{d^2}\right), \tag{5.13}$$

where r contains x and y coordinates, m^* is electronic effective mass, ω_0 represents the confinement frequency, $I_0(x)$ is the modified Bessel function, V_0 and d are the depth and the range of impurity potential, respectively.

In the high-frequency limit, the effective mass Hamiltonian of the laser-driven system subjected to an uniform magnetic field can be described as

$$H = \frac{1}{2m^*}(\mathbf{p}+e\mathbf{A})^2 + \langle V_{dP}(r,\alpha_0)\rangle + \langle V_{dG}(r,\alpha_0)\rangle\,, \tag{5.14}$$

where e is the electron charge and $\mathbf{A}$ ($A_r = 0,\ A_\phi = Br/2,\ A_z = 0$) is the vector potential corresponding to the magnetic field chosen along the z-direction. Then time-independent Schrödinger equation in polar coordinates for the laser-dressed eigen energies and eigen functions reads to

$$
\begin{aligned}
&-\frac{\hbar^2}{2m^*}\frac{1}{r}\frac{\partial}{\partial r}\left(r\frac{\partial\psi}{\partial r}\right)+\frac{L_z^2}{2m^*r^2}\psi+\frac{eB}{2m^*}L_z\psi \\
&+\frac{1}{2}m^*\left(\frac{eB}{2m^*}\right)^2 r^2\psi+\left(\langle V_{dP}(r,\alpha_0)\rangle+\langle V_{dG}(r,\alpha_0)\rangle\right)\psi = \varepsilon\psi\ .
\end{aligned}
\tag{5.15}
$$

Here $L_z=\frac{\hbar}{i}\frac{\partial}{\partial\phi}$ is the z-component of angular momentum which satisfies the eigenvalue equation, $L_z\Phi(\phi)=m\hbar\Phi(\phi)$ (where $\Phi_m(\phi)=e^{im\phi}/\sqrt{2\pi}$, m denotes the magnetic quantum number).

In order to obtain the eigen energies (ε_{nm}) and corresponding wave functions (ψ_{nm}), numerical calculations have been carried out by using finite element method (Pask et al., 2001). In this study, the dipole transitions are allowed only between states satisfying the selection rule $\Delta m=\pm1$ which is independent from polarization direction. Consequently, we will select the energy levels and the wave functions involving in the transitions as follows:

$$
\begin{aligned}
&E_0=\varepsilon_{00}, \quad E_1=\varepsilon_{01}, \quad E_2=\varepsilon_{10}, \quad E_3=\varepsilon_{11} \\
&\psi_0=\psi_{00}, \quad \psi_1=\psi_{01}, \quad \psi_2=\psi_{10}, \quad \psi_3=\psi_{11}
\end{aligned}
$$

Based on density-matrix approach and iterative procedure, the third-harmonic-generation susceptibility is given to be (Mohammadi et al., 2016):

$$
\chi_{3\omega}^{(3)}=\frac{\rho}{\varepsilon_0}\frac{M_{01}M_{12}M_{23}M_{30}}{(\hbar\omega-E_{10}-\mathrm{i}\hbar\Gamma_0)(2\hbar\omega-E_{20}-\mathrm{i}\hbar\Gamma_0/2)(3\hbar\omega-E_{30}-\mathrm{i}\hbar\Gamma_0/3)}\ , \tag{5.16}
$$

where ρ is the electronic density. The linear polarized incident probe electromagnetic field is assumed to be along the x-axis and $M_{ij}=|\langle\psi_j|er\cos\phi|\psi_i\rangle|$(i, j = 0,1,2,3) are the off-diagonal matrix elements of the dipole moment, $E_{k0}=E_k-E_0$ (k = 1,2,3) denotes the transition energies and $\Gamma_0=1/T_0$ is the off-diagonal relaxation rate with transverse relaxation time T_0 (Duque et al., 2013).

5.2.3 Results and discussion

Numerical calculations for the impurity-related THG coefficient in typical GaAs quantum disc with an on-center Gaussian impurity are performed by using the following parameters: the carrier density is $\rho = 5 \times 10^{24}$ m^{-3}, $T_0 = 1$ ps, $\varepsilon_r = 12.53$, $m^* = 0.067 m_0$ (where m_0 is the free electron mass) (Duque et al., 2013; Xie, 2013b).

For a given electronic density and relaxation time, the general behavior of THG is determined by the geometrical factor ($|M_{01}M_{12}M_{23}M_{30}|$) and transition energies. Therefore, initially we demonstrate the laser-field dependence of the matrix elements product for varying magnetic fields, confinement strengths (Figure 5.11 (a)) and structure parameters of impurity (Figure 5.11 (b)). It's clearly seen that, up to specific value of laser-dressing parameter, the enhanced magnitude of the geometrical factor is sequenced by decreasing behavior. Presumably the underlying reason is based on the variation of Gaussian potential. Applying an ILF on the system, leads to a widening of the effective width of impurity potential and shallowing in its depth. Therefore, for greater values of laser-dressing parameter the electron predominantly feels the parabolic potential. Moreover, we can clearly see that the absolute value of matrix elements' product becomes smaller for greater values of B, $\hbar\omega_0$ and impurity parameters (d and V_0). The underlying reason for which is that the extended areas of the wave function will decrease with stronger values of the aforesaid parameters.

Figure 5.12 (a) and (b) depicts the influence of ILF on the energy difference between the ground state and first three excited states of the system. As can be seen in both figures, all the transition energies decline for greater values of α_0 which bring about a weakening in confinement. In Figure 5.12 (a), the main figure shows that the magnitudes of E_{10}, $E_{20}/2$ and $E_{30}/3$ augment with greater values of B. Also, it is monitored that the $E_{20}/2$ and $E_{30}/3$ almost equal for $B = 1.5$ T in the presence of ILF. The inset figure exhibits that the magnitudes of E_{10}, $E_{20}/2$ and $E_{30}/3$ increases for higher values of $\hbar\omega_0$. From Figure 5.12 (b) it is easily seen that the higher values of V_0 and d cause higher energy differences and the energy differences $E_{20}/2$ and $E_{30}/3$ are almost same at particular values of impurity parameters ($V_0 = 40$ meV and $d = 6$ nm).

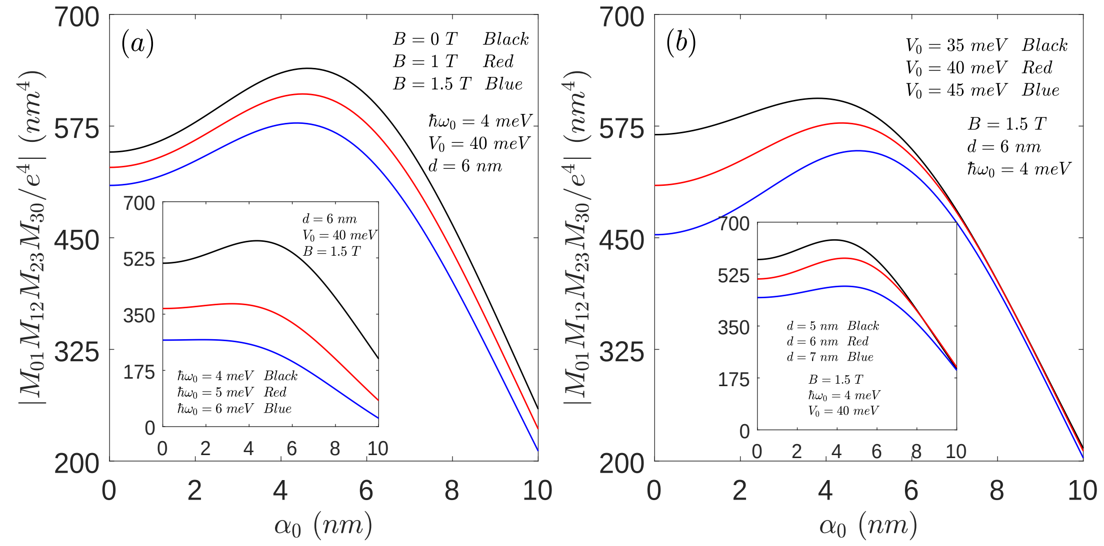

Figure 5.11 The matrix elements product $|M_{01}M_{12}M_{23}M_{30}|$ as a function α_0 for different values of (a) B and $\hbar\omega_0$, (b) impurity parameters V_0 and d

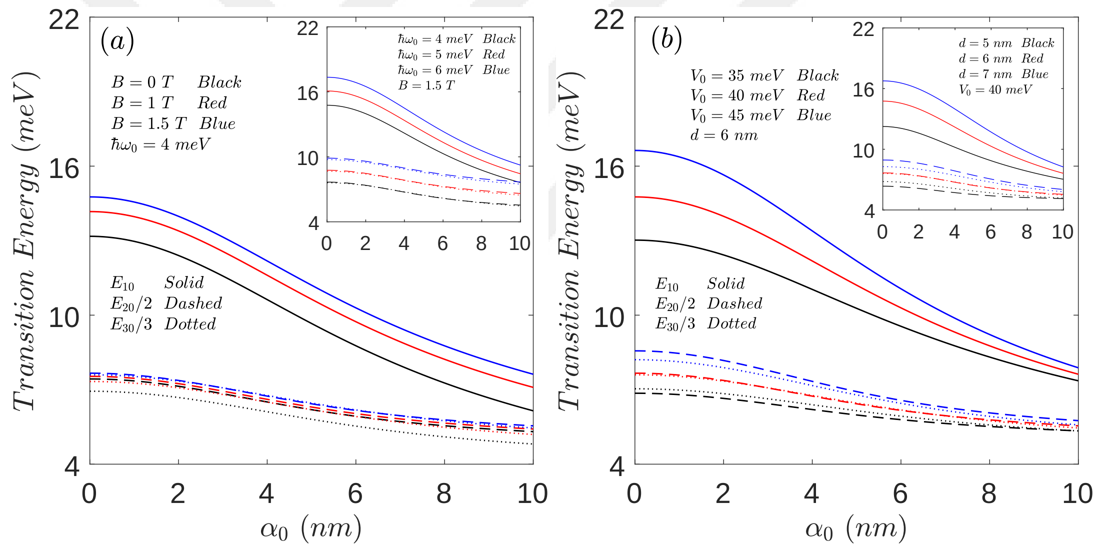

Figure 5.12 Transition energy vs laser-dressing parameter considering three values of (a) magnetic field and confinement strength with V_0 = 40 meV and d = 6 nm, (b) impurity-related parameters for B = 1.5 T and $\hbar\omega_0$ = 4 meV

In Figure 5.13, the effect of external fields on the THG coefficient is demonstrated for a system defined with $\hbar\omega_0$ = 4 meV, V_0 = 40 meV and d = 6 nm. We see that the peak magnitude enhances with higher values of B and α_0. In the absence of magnetic field, the dominant peak belonging to the frequency $\omega_{30}/3$ enhances by the application of laser radiation. By turning on the magnetic field, the energy differences $E_{20}/2$ and $E_{30}/3$ become almost the same which results in single peak of THG signal. It

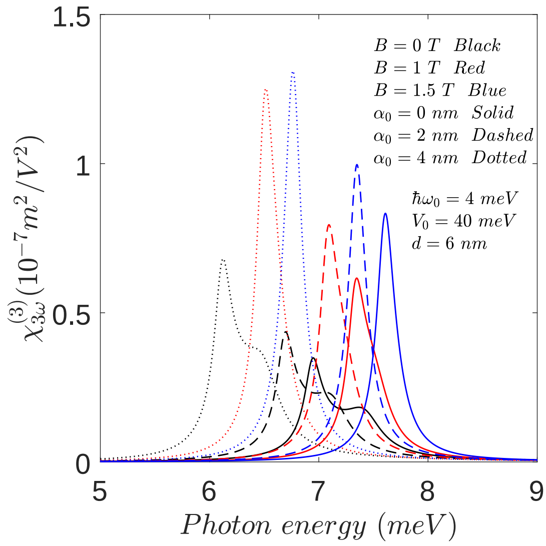

Figure 5.13 The third-harmonic generation as a function of photon energy for different values of magnetic field and laser radiation. We use $\hbar\omega_0$ = 4 meV, V_0 = 40 meV and d = 6 nm

should be noted that the peaks belonging to E_{10}, which occurs in the range 10 and 17 meV, have an imperceptible small contribution in all the THG coefficient spectra figures because of the competition between the the dipole matrix elements and the energy differences between states. Furthermore, the peak position of THG moves to the higher energies (blue-shift) with increasing B owing to increment in the transition energies whereas it shifts to lower energy region (red-shift) by augmenting laser-dressing parameter. The inferred information from the figure is that the peak amplitude and position of the THG signal could be adjusted properly by the application of ILF.

Figure 5.14 displays the effects of laser-dressing and impurity-range parameters on the variation of THG. For a particular configuration parameter set studied here, the superposition of the resonant peaks associated with $E_{20}/2$ and $E_{30}/3$ comprises of for d=6 nm. The intensity of the corresponding peak in the THG signal is much larger in comparison with the intensities of unequally spaced subband energy situations belonging to d = 5 nm and 7 nm. We can clearly see that the magnitude of THG is greater for lower values of d in accordance with an enhancement observed in matrix elements. For d = 5 and d = 7 nm, two resonance peaks are obtained due to the difference between $E_{20}/2$ and $E_{30}/3$ and here the main peak is associated with the transition $\omega_{30}/3$. In addition, turning on the laser field induces a shift in THG peaks

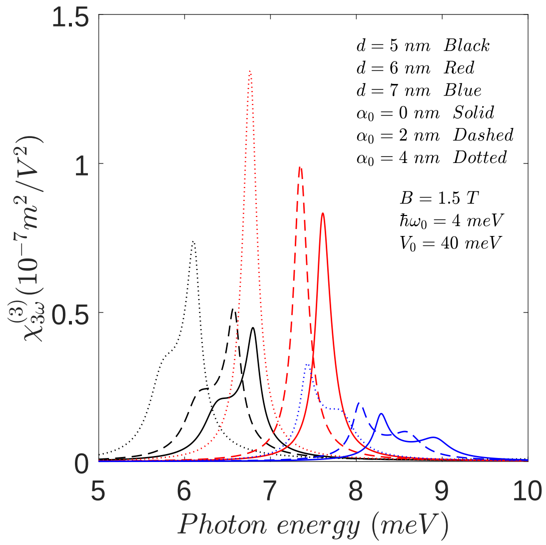

Figure 5.14 THG coefficient as a function of photon energy for varying values of d and α_0 with $B = 1.5$ T, $\hbar\omega_0 = 4$ meV and $V_0 = 40$ meV

toward the lower energies and remarkable increment in their magnitudes.

In attempt to investigate the effects of intense laser field and the depth of the on-center Gaussian impurity on the THG coefficient, in Figure 5.15 we plot the variation of THG coefficient with incident photon energy for different values of V_0 and α_0. It can be seen from figure that, in the absence of ILF for lower values of V_0 a single resonant peak of THG coefficient takes place while for $V_0 = 45$ meV a broadened peak occurs because $E_{20}/2$ and $E_{30}/3$ are not completely equal. In particular for a depth of impurity of 40 meV, the maximum peak value of THG is obtained. Moreover, increment in laser-dressing parameter gives rise to a red-shift in the peak position of THG and enhancement in its magnitude.

It's well-known that the confinement frequency crucially affects the electronic structure of nanostructures and so their optical response. Therefore, in Figure 5.16 we present the variation of the THG coefficient as a function of photon energy for three values of $\hbar\omega_0$ and α_0. From the figure, we observe a single peak for THG signal consisting of superposed $E_{20}/2$ and $E_{30}/3$ for all $\hbar\omega_0$ values considered here. Besides, the position of resonance peak moves to higher energy region and its amplitude declines for higher values of $\hbar\omega_0$ in accordance with a reduction in the absolute value

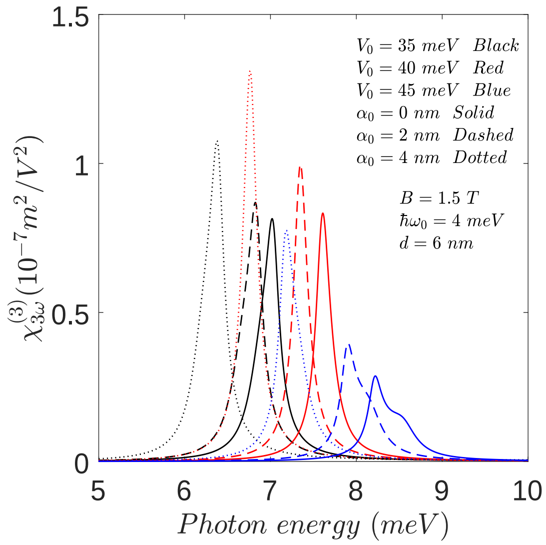

Figure 5.15 The variation of THG coefficient as a function of photon energy for different values of V_0 and α_0. The fixed parameters are B = 1.5 T, $\hbar\omega_0$ = 4 meV and d = 6 nm

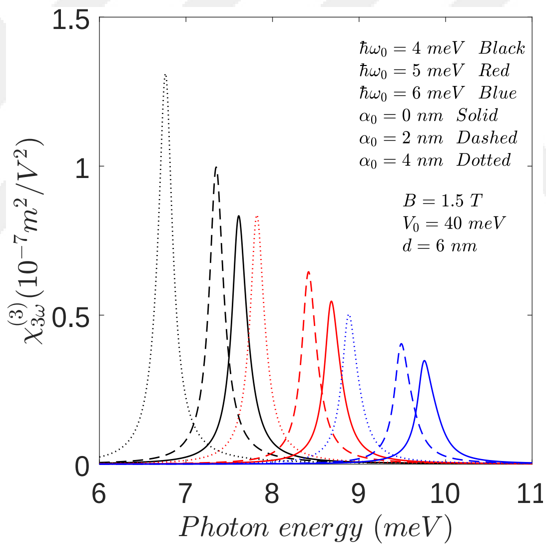

Figure 5.16 Dependence of THG coefficient on the incident photon energy for three values of confinement potential strength and laser-dressing parameter. We set B = 1.5 T, V_0 = 40 meV and d = 6 nm

of matrix elements' product. Similar to other figures, the stronger intense laser field brings about a red-shift and boosts the peak magnitude of THG.

In an attempt to make a detailed assessment of the ILF- and system parameters-induced changes in the peak amplitude of THG spectrum, we plot the variations of highest amplitude signal of THG as a function of laser-dressing parameter in Figure 5.17 (a) and (b). In both figures, we can clearly see that the maximum peak

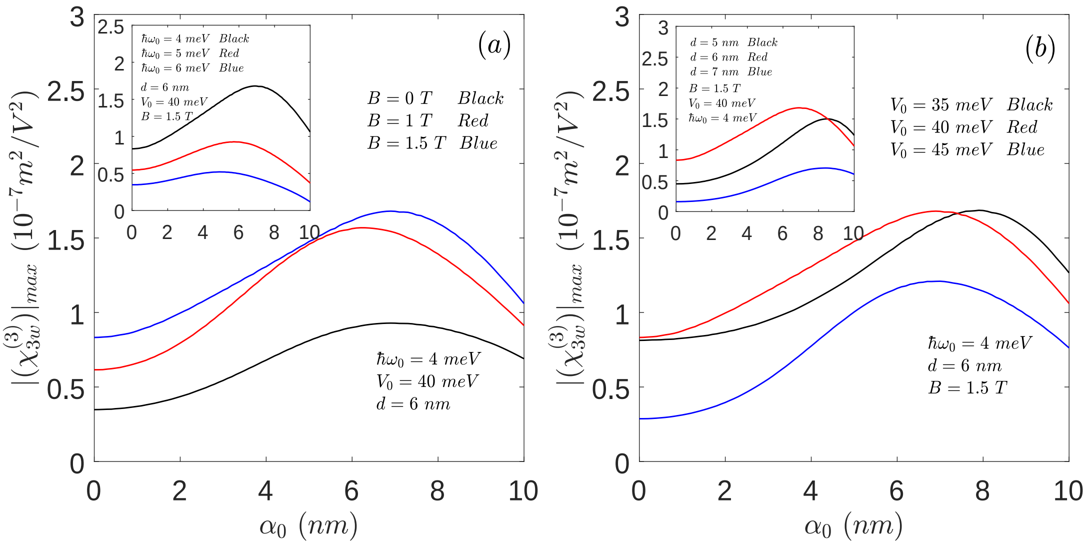

Figure 5.17 The maximum value of highest amplitude signal of THG as a function of laser-dressing parameter for (a) different values of B and $\hbar\omega_0$ (b) for three values of V_0 and d

value of THG rises until a specific value of α_0 whereas its value diminishes for greater values. This situation relies on the fact of competitive effects between geometrical factor and transition energies. Moreover, as seen in Figure 5.17 (a), the resonant peak value of THG is augmented by higher (smaller) values of B ($\hbar\omega_0$). From Figure 5.17 (b), an increment in the resonant peak value is observed for specific values of V_0 = 40 meV and d = 6 nm and this result shows that selected parameter set (as chosen in Ref (Halonen et al., 1996b)) is perfectly compatible to achieve the larger THG coefficient.

5.3 Impurity-modulated optical response of a disc-shaped quantum dot subjected to laser radiation

5.3.1 Introduction

The recent impressive advances in nanostructure technology have made it possible the control of the electronic, optical and transport properties of nanometer scale semiconductor structures via external electric/magnetic or intense laser fields (ILF) (Kilic et al. (2020)and references therein). A great deal of studies focusing on the effects of external fields in nanostructures have been carried out. For instance, Bejan conducted an investigation on the optical response of double quantum dot (QD) by applying electric field (Bejan, 2017b). Magnetic field related changes in the electronic structure and intraband quantum transitions in multishell spherical QD have been reported by Holovatsky et al. (Holovatsky et al., 2017). Xie has presented the optical response of an exciton in a disc-like QD under intense laser field (Xie, 2011b). The simultaneous presence effects of laser and magnetic fields of disc-shaped QD researched by Prasad and Silotia (Prasad & Silotia, 2011) demonstrate that the optical properties of the system strongly depend on the incident optical intensity and applied magnetic field. Furthermore, it's well known that a proper control of impurity levels in quantum systems becomes an important factor in the operating performance of the optoelectronic devices (Wei et al., 2018). This is why many theoretical and experimental researches have been devoted on the impurity effects in laser-driven QDs (Kilic et al. (2020) and references therein). Results of these studies expose that the electronic and optical properties associated with impurities can be adjusted and controlled by the laser field intensity (Barseghyan et al., 2017; Soltani-Vala & Barvestani, 2017). The action of electric field and intense laser field on the optical response in a impurity doped disc-like QD has been reported by Spandonide et al (Spandonide et al., 2016). Presented results indicate that the impurity and external fields cause a remarkable change on the electronic states and the dipole matrix elements. Sari et al. have researched the effects of non-resonant ILF and impurity on the optical properties in quantum dots modelled with a δ-doped axial potential (Sari et al., 2018). Hydrogenic donor impurity levels in two-dimensional quantum dots (2DQDs) and rings with finite square lateral confining potential and under the action of ILF have been reported by Laroze et al (Laroze et al., 2016). Very recently, Wang and coworkers discussed the magnetopolaron effect on donors in semiconductors under ILF (Wang et al., 2019). In most studies, examining interaction between laser field and low-dimensional structures, the laser beam has been considered with linear polarization. Nevertheless, the effects of circularly polarized ILF have been intensely investigated in atomic-structures. In particular, the effects of monochromatic laser field of circular polarization on the structure, dichotomy, stabilization and atomic distortion of Hydrogen atom have been reported by Pont and coworkers (Pont et al., 1988a,b; Pont, 1989; Pont & Gavrila, 1990). In addition to the application to the structures of the atomic size, less effort has been paid on the effects of the circularly polarized laser field on low-dimensional structures. The influences of ILF on the binding energy, the linear and third-order nonlinear optical properties of a hydrogenic impurity in a spherical QD have been examined by Xie (Xie, 2011a). Vaseghi et al. have researched the optical response of parabolic quantum dots with dressed impurity under the combined act of pressure, temperature and laser radiation (Vaseghi et al., 2015). However, to the best of our knowledge, the impurity-related optical properties of 2DQDs under the action of a circularly polarized laser radiation has not been studied yet.

The aim of this work is to present the electronic and optical properties of a 2DQD with hydrogenic impurity irradiated by a THz laser and then subjected to magnetic field. The remaining part of the paper is organized as follows: In Sec. 5.3.2 we outline the theoretical framework. The discussion of the obtained results is presented in Sec. 5.3.3.

5.3.2 Theory

The system we examine is an electron locating in the xy-plane experiencing a parabolic confining potential with an on-center hydrogenic impurity and subjected to a perpendicular magnetic field along the z-axis. In the absence of ILF, Hamiltonian of the system can be expressed as:

$$H = \frac{1}{2m^*}(\mathbf{p}+e\mathbf{A})^2 + \frac{1}{2}m^*\omega_0^2 r^2 - \frac{e^2}{4\pi\epsilon_0\epsilon_r r}\,. \tag{5.17}$$

Here $r = (x, y)$, m^* and e is effective mass and the charge of an electron, respectively. Magnetic field is represented by the vector potential A $(0, Br/2, 0)$, ω_0 stands for the confinement frequency and ϵ_r denotes medium's dielectric constant.

The influence of non-resonant, monochromatic, circularly polarized ILF of frequency Ω is tackled within the framework of non-perturbative theory and high-frequency Floquet approach (Lima et al., 2009a; Pont & Gavrila, 1990; Sakiroglu et al., 2018). The Schrödinger equation for a system with ILF-modulated potentials that is exposed to a static magnetic field is:

$$\left[\frac{1}{2m^*}(\mathbf{p}+e\mathbf{A})^2+\langle V_{dP}(r,\alpha_0)\rangle+\langle V_{dC}(r,\alpha_0)\rangle\right]\varphi(r)=\varepsilon\varphi(r) \tag{5.18}$$

where $\langle V_d(\mathbf{r},\alpha_0)\rangle = \frac{1}{T}\int_0^T V(\mathbf{r}+\boldsymbol{\alpha}(t))dt$ is the time-averaged potential comprising the dressing effect of the laser radiation with period $T = 2\pi/\Omega$. The electron's motion in the laser field is defined by $\boldsymbol{\alpha}(t) = \alpha_0(\hat{x}\cos\Omega t+\hat{y}\sin\Omega t)$ and the $\alpha_0 = eA_0/m^*\Omega$ is the "laser-dressing" parameter (Fanyao et al., 1996). The dressed form of parabolic confinement potential is obtained as $\langle V_{dP}(r,\alpha_0)\rangle = \frac{1}{2}m^*\omega_0^2\left(r^2+\alpha_0^2\right)$ (Kilic et al., 2018) and the laser-dressed form of Coulomb potential is carried out analytically as follows (Pont, 1989):

$$\langle V_{dC}(r,\alpha_0)\rangle = -\frac{e^2}{4\pi\epsilon_0\epsilon_r(r+\alpha_0)}\frac{2}{\pi}K(p) \tag{5.19}$$

Here $K(p)$ is the complete elliptic integral of the first kind with $p = (4r\alpha_0/(r+\alpha_0)^2)^{1/2}$ (Gradsteyn & Ryzhik, 2007; Pont & Gavrila, 1990).

In this work, the finite element method (FEM) is used to obtain numerically the eigen energies (ε_{nm}) and eigen functions (φ_{nm}) of Eq. (5.18) expressed in polar coordinates where n and m are radial and angular quantum numbers, respectively. This powerful technique, based on Galerkin approach and defined in a weak formulation is a variational expansion method where the basis functions are strictly local, piecewise polynomials in real space (Pask et al., 2001; Zienkiewicz et al., 2005). We have taken into account the dipole transitions between electronic states with $\Delta m = \pm 1$ and accordingly the chosen energy states and their wave functions are, $E_0 = \varepsilon_{00}$, $E_1 = \varepsilon_{11}$ and $\psi_0 = \varphi_{00}$, $\psi_1 = \varphi_{11}$. In the present study, we have considered two incident radiations: probe one with photon energy resonant or near-resonant with the specific transition, the other one is a monochromatic intense laser radiation with frequency different from the transition energies between the states taken into consideration. The available broad range for the intensity and the frequency of the ILF, render possible to choose a field that is far from the resonance for intersubband transitions.

The linear and third-order nonlinear optical absorption coefficients (OACs) for the related intersubband transitions obtained from compact density matrix method within a two-level system approach, are given to be (Karabulut & Baskoutas, 2008; Liu et al., 2012; Unlu et al., 2006):

$$\alpha^{(1)}(\omega) = \omega\sqrt{\frac{\mu}{\epsilon_r}}\frac{\sigma_s|M_{10}|^2\hbar\Gamma_0}{(E_{10}-\hbar\omega)^2+(\hbar\Gamma_0)^2} \tag{5.20}$$

$$\begin{aligned}\alpha^{(3)}(\omega,I) &= -\omega\sqrt{\frac{\mu}{\epsilon_r}}\left(\frac{I}{2n_r\epsilon_0 c}\right)\frac{\sigma_s\hbar\Gamma_0|M_{10}|^2}{[(E_{10}-\hbar\omega)^2+(\hbar\Gamma_0)^2]^2} \\ &\times\left\{4|M_{10}^2|-|M_{11}-M_{00}|^2\times\frac{\left[3E_{10}^2-4\varepsilon_{10}\hbar\omega+\hbar^2(\omega^2-\Gamma_0^2)\right]}{E_{10}^2+(\hbar\Gamma_0)^2}\right\}.\end{aligned} \tag{5.21}$$

and then the total OAC can be find by $\alpha(\omega,I) = \alpha^{(1)}(\omega)+\alpha^{(3)}(\omega,I)$. Here μ is the magnetic permeability, the electronic density is σ_s, I defines the optical intensity, n_r is the refractive index of material, c stands for the speed of light, the energy difference is $E_{10} = E_1 - E_0$, $M_{ij} = |\langle\psi_i|er\cos\phi|\psi_j\rangle|$ $(i, j = 0,1)$ depicts the dipole matrix elements (Kilic et al., 2018) and $\Gamma_0 = 1/T_0$ is the relaxation rate for related states (Mora-Ramos et al., 2012a).

The linear and the nonlinear contributions of the relative refractive index changes (RICs) are given by the following (Li et al., 2012):

$$\frac{\Delta n^{(1)}(\omega)}{n_r} = \frac{1}{2n_r^2\epsilon_0}|M_{10}|^2\sigma_s\left[\frac{E_{10}-\hbar\omega}{(E_{10}-\hbar\omega)^2+(\hbar\Gamma_0)^2}\right] \tag{5.22}$$

and

$$\frac{\Delta n^{(3)}(\omega,I)}{n_r} = -\frac{\mu c}{4n_r^3\epsilon_0}|M_{10}|^2\frac{\sigma_s I}{[(E_{10}-\hbar\omega)^2+(\hbar\Gamma_0)^2]^2}$$

$$\times\Bigg[4(\varepsilon_{10}-\hbar\omega)|M_{10}|^2-\frac{(M_{11}-M_{00})^2}{E_{10}^2+(\hbar\Gamma_0)^2}\{(E_{10}-\hbar\omega) \tag{5.23}$$

$$\times\Big[E_{10}(E_{10}-\hbar\omega)-(\hbar\Gamma_0)^2\Big]-(\hbar\Gamma_0)^2(2E_{10}-\hbar\omega)\Big\}\Bigg]$$

The total magnitude of RICs is the sum of Eq. (5.33) and Eq. (5.34).

5.3.3 Results and discussion

In this study, numerical results are given for a system with on-center hydrogenic impurity in a typical GaAs QD and the physical parameters are used as follows (Xie, 2010; Yuan et al., 2015): $m^* = 0.067\,m_0$ (m_0 being the free electron mass), charge density of $\rho = 5\times10^{24}$ m^{-3}, $\epsilon_r = 12.4$, $T_0 = 0.14$ ps, $\mu = 4\pi\times10^{-7}$ Hm^{-1}, $n_r = 3.2$ and $I = 1.5\times10^{10}$ W/m^2.

In order to examine the electronic properties of the system, in Figure 5.18 the energies ε_{nm} (for radial quantum numbers 0 and 1 with $|m| \leq 1$) as a function of magnetic field are exhibited for different values of laser-dressing parameter for cases with and without impurity shown by solid and dashed lines, respectively.

Presence of an impurity ends up with a crossing between Fock-Darwin states of 2DQD (dashed lines) which disappears for stronger values of α_0. Besides, as evident from the spectrum, magnetic field lifts the initial degeneracies in the energies and the inclusion of impurity leads to the serious diminution of all energies. In particular, the existence of impurity causes a more noticeable effect in the ground-state energy. The reason for this situation could be explained by the increment in the electron localization. Moreover, the figures clearly show that for the strengthening of B, the ground-state energy (E_0) is almost constant due to the increment of electron-

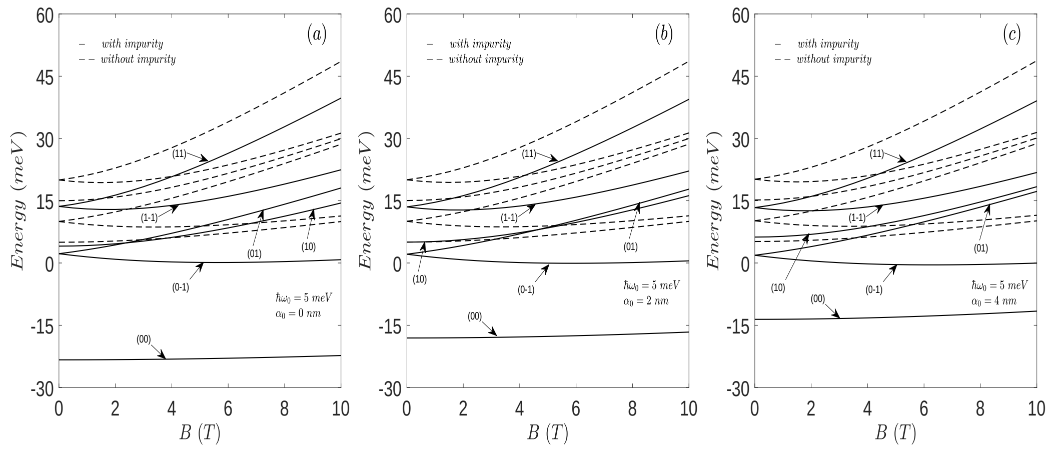

Figure 5.18 Lowest single-electron energy states as a function of magnetic field for varying values of laser-dressing parameter (a) α_0 = 0 nm, (b) α_0 = 2 nm and (c) α_0 = 4 nm. The results are given for QD defined by $\hbar\omega_0$ = 5 meV

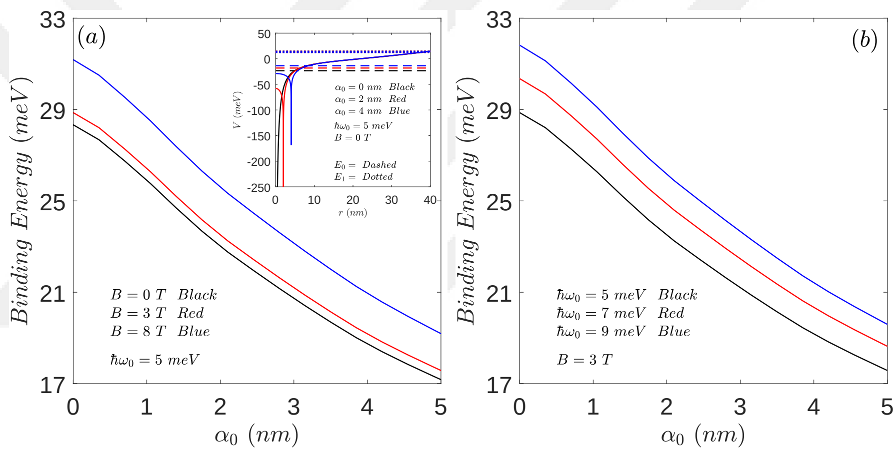

Figure 5.19 The variation of the binding energy of the ground-state versus α_0 with several values of (a) B at $\hbar\omega_0$ = 5 meV, (b) the confinement strength at B = 3 T. The inset shows of laser-dressed potential profile versus a radial coordinate and corresponding E_0 and E_1 energies for different values of α_0

localization while the energies of the excited states depict an increasing behavior. Furthermore, from Figure 5.18 (b) and (c) it is readily seen that the energy value of ground-state crucially increases with the action of ILF, yet the upper states are less affected. This situation relies on the fact that when the ILF is applied to the system, the Coulomb center shifts in the radial direction (inset of Figure 5.19(a)). In other words, the laser-dressed Coulomb potential is logarithmically singular in the vicinity of α_0 with monotonically decreasing magnitude when moving off from it (Pont et al., 1988a). Consequently, this result can be interpreted as the ground-state energy is more sensitive to ILF than the excited states.

Figure 5.19 depicts the effects of THz laser on the binding energy for particular magnetic field values and confinement strengths. Figure 5.19 (a) and (b) show that the binding energy is enhanced by increasing magnetic field and confinement strength. The physical reason can be explained by the fact that the impurity-related states become more localized for greater values of B and $\hbar\omega_0$ due to stronger quantum confinement and increment of absolute Coulomb interaction. α_0-dependence of the Coulomb potential results with an important impact on the ground state binding energy. The noticeable observation from both figures is that the binding energy decreases monotonically with α_0 which can be attributed to the radial shifting in the minimum of impurity potential as seen from Figure 5.19(a). This can be explained by the fact that increment in the electron-impurity distance which give rise to a weakening in the strength of absolute Coulomb interaction.

Before a step further toward the optical coefficients, it is important to analyze the general behavior of dipole matrix element according to the presence of ILF for better understanding of the optical characteristics of 2DQDs. Therefore, in Figure 5.20, we demonstrate the variation of dipole matrix element M_{10} as a function of α_0 for three values of magnetic field and confinement strength. The magnitude of absolute matrix

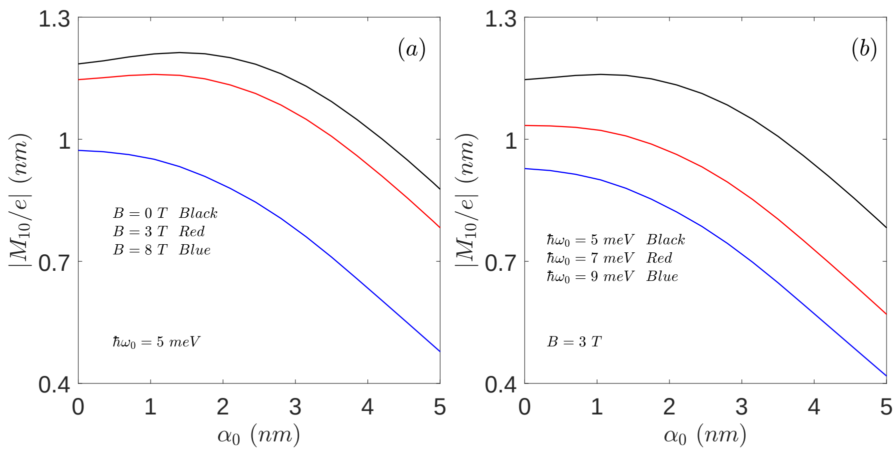

Figure 5.20 $|M_{10}|$ as a function of α_0 considering three values of (a) B at $\hbar\omega_0$ = 5 meV and (b) $\hbar\omega_0$ for fixed magnetic field of 3 T

element declines with augmentation in ILF as seen in Figure 5.20 (a) and (b), which is a consequence of the decrement of overlaps among the wave functions. Besides, both figures depict that the $|M_{10}|$ decreases with strengthening in B and $\hbar\omega_0$ owing to

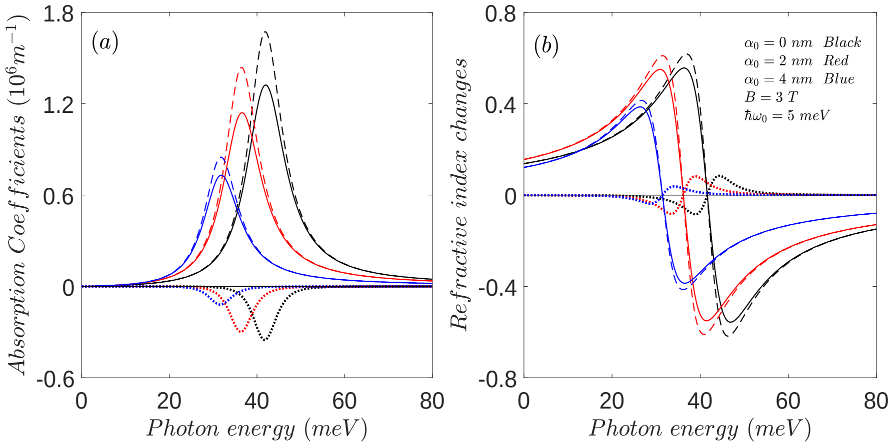

Figure 5.21 The linear, nonlinear and total parts of (a) OACs and (b) RICs as a function of photon energy for several values of laser-dressing parameter. The confinement strength and magnetic field are set to $\hbar\omega_0 = 5$ meV and $B = 3$ T, respectively

reduction in overlaps among wave functions.

So as to analyze the influence of ILF on the optical response of system, in Figure 5.21, we show the variation of the linear and third-order nonlinear OACs and relative RICs as a function of incident photon energy for varying values of laser-dressing parameter. We should note that the linear, third-order nonlinear and the total optical coefficients are typified by dashed, dotted and solid line in all figures, respectively. Increment in α_0 brings about diminishment in the height of the resonance peaks of the optical coefficients as seen in Figure 5.21 (a) and (b). The peak positions of OACs and RICs go toward the lower energy values (red-shift) with augmenting α_0 which is a result of the decrease in the transition energy. We should emphasize that ILF has profound effect on the E_0 energy level in comparison with the E_1.

In an effort to put forth the magnetic field-induced optical response, in Figure 5.22 (a) and (b) we depict the variation of the linear and third-order nonlinear optical properties as a function of incident photon energy for different strength of B. The system considered is described with confinement of 5 meV and ILF of $\alpha_0 = 2$ nm. We observe that for stronger magnetic field, reduction in the peak magnitudes of OACs and RICs is accompanied by a blue-shift in the their peak positions. Strengthening in B leads to an enhanced transition energy which is the underlying reason for the higher-energy

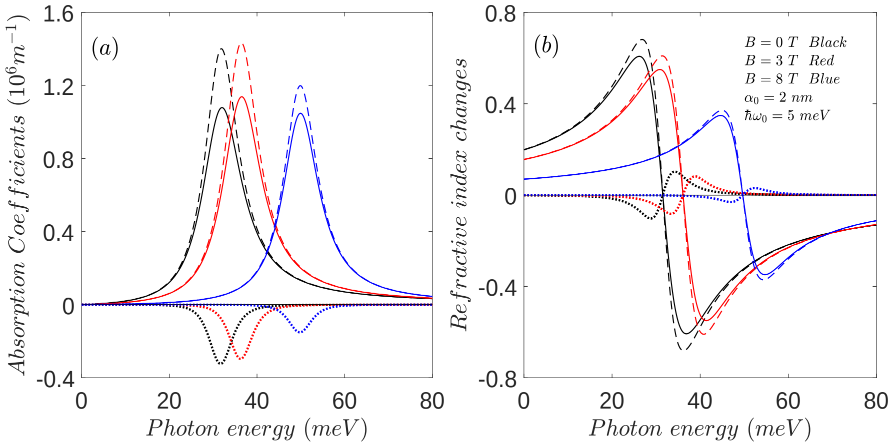

Figure 5.22 The variation of the (a) OACs and (b) RICs as a function of the photon energy for specific values of B with α_0 = 2 nm and $\hbar\omega_0$ = 5 meV

region shift in the resonant peak positions. Competitive effects between the $|M_{ij}|$ and E_{ij} determines the variation of the peak amplitudes of the optical properties (Kilic et al., 2018).

Figure 5.23 displays the dependence of the OACs and RICs on the strength of parabolic confinement potential for a laser field of α_0 = 2 nm and the system is subjected to a field of B = 3 T. From Figure 5.23 (a) and (b), we can clearly see that

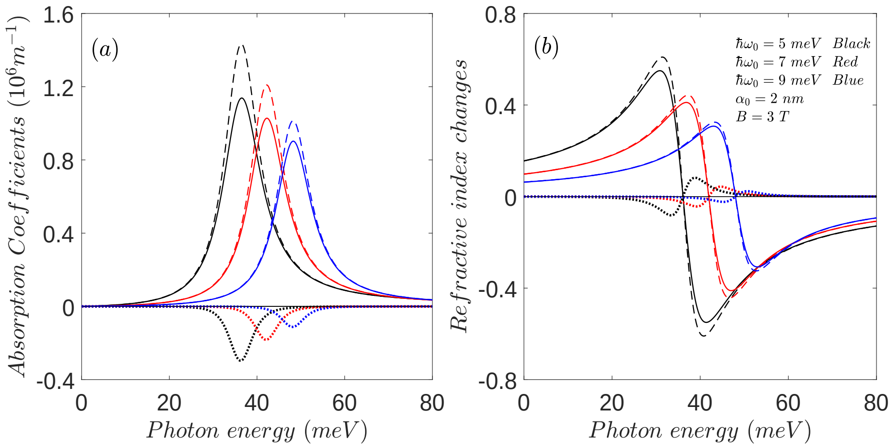

Figure 5.23 (a) OACs and (b) RICs vs photon energy for varying values of $\hbar\omega_0$

enhancement in confinement strength leads to a gradual decrease in the magnitude of OACs and RICs and blue-shift in the their peak positions. This situation can be clarified by the diminution in $|M_{10}|$ and increment in transition energy, respectively.

It would be noteworthy to point out the effects of the THz laser field, magnetic field

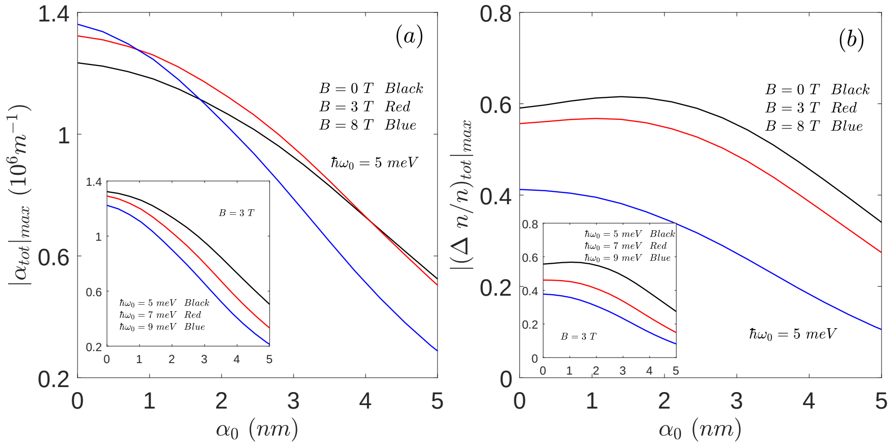

Figure 5.24 Plot of $|\alpha_{tot}|_{max}$ and $|(\Delta n/n)_{tot}|_{max}$ versus α_0 for varying values of magnetic field considering $\hbar\omega_0$ = 5 meV. The insets show the dependence on the confinement potential strength for a constant B

and confinement strength on the peak amplitudes of optical properties. Therefore, Figure 5.24 (a) and (b) expose the changes of the peak magnitude of the total OAC (RIC) at resonance frequency vs α_0. Both figures reveal that the resonant peaks of OAC and RIC significantly diminish for greater α_0-values. Particularly, as is seen from Figure 5.24 (a), increment in B leads to rise in the maximum peak value of α_{tot} for lower laser-dressing parameter while brings about decline for greater values of α_0. Moreover, the resonant peak value of $(\Delta n/n)_{tot}$ decreases with increasing B as seen from Figure 5.24 (b). From the insets in the subfigures it's readily seen that higher confinement frequencies yield diminishing in the resonant peak values of the optical properties.

5.4 Screened donor impurity in a two-dimensional quantum dot under THz laser field

5.4.1 Introduction

In recent years, the study of two-dimensional quantum dots (2DQDs), which possess extraordinary electronic and optical properties, has become important not only from the aspect of fundamental science but also for device applications (Huang, 2013; Li et al., 2008; Mikhail & Shafee, 2017; Shojaei & Vala, 2015). In particular, the physics of impurity states in QDs has been dramatically studied due to the modification of electronic and optical properties associated with impurity (Wang et al., 2019). Therefore, many researchers have focused on the intriguing impurity-related properties of QDs and have broadcasted a number of publications (Bera et al., 2016; Saha & Ghosh, 2015; Soltani-Vala & Barvestani, 2017; Zeng et al., 2014). Xie have investigated both the electric field and confinement effects on the impurity-related states and nonlinear optical rectification of a parabolic disc-like QD (Xie, 2009). Al-Hayek and Sandouqa have obtained the hydrogenic-like impurity binding energy of a Gaussian QD by using the method of the shifted 1/N expansion (Al-Hayek & Sandouqa, 2015). The controllability of electronic properties and optical characteristics in an impurity doped quantum disc by magnetic field has been demonstrated by Niculescu and co-workers (Niculescu et al., 2017).

In most of the studies, the impurity potential in QDs is usually described by Coulomb potential (CP) (Chen, 2011; Dehyar et al., 2016; Sheng et al., 2016; Yun et al., 2015) or Gaussian impurity (Ganguly et al., 2017; Halonen et al., 1996b; Hosseinpour et al., 2016; Sarkar et al., 2016), while the Screened Coulomb (or the Debye-Yukawa) potential (SCP) (Varshni, 2001a) is less preferred for impurity modeling. Although less studied in QDs, the SCP, which is a short-range potential and tends faster to zero than CP at $|\mathbf{r}| \to \infty$ limit (Mizutani, 2001; Poszwa, 2014), has been widely implemented in different areas such as atomic physics, nuclear physics, plasma physics, semiconductors, and quantum chemistry (Brum et al., 1984; Soylu & Boztosun, 2008; Taseli & Eid, 1996). For instance, Ping and Jiang have investigated the effects of the charge screening on the exciton binding energy in GaAs-Al_xGa_{1-x} quantum wells (Ping & Jiang, 1993). Villalba and Pino have presented the energy levels of a two-dimensional screened hydrogenic donor under a constant magnetic field (Ping & Jiang, 2002). They showed that the strength of screening parameter is largely effective in consisting of the bounded states in 2D-screened hydrogen atom.

On the other hand, another important topic that is studied extensively is the effect of intense THz laser field (ITLF) on the behavior of impurity states in nanostructures. Due to the ability of ITLF on adjusting and controlling electronic and optical properties of nanostructures, a great number of works have been done by researchers (Chakraborty et al., 2018; Varshni, 2001b; Vaseghi et al., 2015; Vinasco et al., 2019; Wang et al., 2018; Wei et al., 2018). Bejan and Niculescu have researched the influence of ITLF on the electronic and optical properties asymmetric double quantum dots (Bejan & Niculescu, 2016b). Theoretical results given in Reference (Brandi et al., 2004) show that the binding energies of donor impurities are affected by the intensity of the laser. The research of photoionization cross-section and impurity binding energy in GaAs-GaAlAs spherical quantum dots under electric and intense laser fields have been investigated by Burileanu and he found that increment in the electric and laser field intensities leads to diminishment in the magnitude of impurity binding energy (Burileanu, 2014).

As can be seen from the literature, many studies have been conducted on the optical and electronic properties of laser-driven QDs which include hydrogenic or Gaussian impurity. However, the effect of ITLF on the optical response of a 2DQD with an on-center screened Coulomb impurity has been not examined so far. The goal of this work is to investigate the electronic and optical properties of a 2DQD with impurity defined by SCP and irradiated by a THz laser. The structure of this paper is as follows: The theoretical framework is described in Sec. 5.4.2 and Sec. 5.4.3 is dedicated to discuss of the obtained results.

5.4.2 Theory

In this paper, we investigate the THz laser effect of on-center donor impurity on a two-dimensional parabolic QD system. Presence of an impurity is described with SCP given as $V_{SC} = -e^{-\lambda r}/r$ where λ is screening parameter characterizing the shielding of the impurity ions (Varshni, 2001a). We assume that the system is irradiated by a non-resonant, monochromatic, circularly polarized ITLF of frequency Ω. Within the framework of non-perturbative theory, in the high-frequency regime the motion of electron is specified by the time-averaged dressed potential $\langle V_d(\mathbf{r}, \alpha_0)\rangle = \frac{1}{T}\int_0^T V(\mathbf{r} + \boldsymbol{\alpha}(t))dt$ where $T = 2\pi/\Omega$ is the period of ITLF. $\boldsymbol{\alpha}(t) = \alpha_0(\hat{x}\cos\Omega t + \hat{y}\sin\Omega t)$ corresponds to the motion of the electron in the ITLF and the $\alpha_0 = eA_0/m^*\Omega$ is the laser-dressing intensity parameter (Fanyao et al., 1996). Time-independent Schrödinger equation governing the effects of high-frequency radiation for the zeroth Floquet component (φ_{nm}) with corresponding quasienergy (ε_{nm}) is given (Pont & Gavrila, 1990):

$$\left[\frac{\mathbf{p}^2}{2m^*} + \langle V_{dP}(r,\alpha_0)\rangle + \langle V_{dSC}(r,\alpha_0)\rangle\right]\varphi_{nm}(r) = \varepsilon_{nm}\varphi_{nm}(r)\ . \tag{5.24}$$

Here the radial and magnetic quantum numbers are depicted by n and m, V_{dP} and V_{dSC} corresponds to the laser-dressed form of parabolic confinement (Kilic et al., 2018) and screened Coulomb impurity potentials, respectively. In this study, we have numerically carried out the calculation of eigen energies with corresponding eigen functions by using one-dimensional finite element method based on Galerkin approach. This approach identified in a weak formulation is a variational expansion method and the basis functions are local, piecewise polynomials in real space. For the survey of the optical response of the system, we have considered the dipole transitions allowed only between states satisfying the selection rule $\Delta m = \pm 1$. Therefore, we have selected the energy levels and the wave functions participating in the transitions to be $E_0 = \varepsilon_{00}$, $E_1 = \varepsilon_{11}$ and $\psi_0 = \varphi_{00}$, $\psi_1 = \varphi_{11}$.

The linear and third-order nonlinear optical absorption coefficients (OACs) for intersubband transitions are obtained by means of the compact density matrix approach and iterative scheme (Liu et al., 2012):

$$\alpha^{(1)}(\omega) = \omega\sqrt{\frac{\mu}{\epsilon_r}}\frac{\sigma_s|M_{10}|^2\hbar\Gamma_0}{(E_{10}-\hbar\omega)^2+(\hbar\Gamma_0)^2} \tag{5.25}$$

$$\begin{aligned}\alpha^{(3)}(\omega,I) &= -\omega\sqrt{\frac{\mu}{\epsilon_r}}\left(\frac{I}{2n_r\epsilon_0 c}\right)\frac{\sigma_s\hbar\Gamma_0|M_{10}|^2}{[(E_{10}-\hbar\omega)^2+(\hbar\Gamma_0)^2]^2} \\ &\quad\times\left\{4|M_{10}^2| - |M_{11}-M_{00}|^2\times\frac{\left[3E_{10}^2-4\varepsilon_{10}\hbar\omega+\hbar^2(\omega^2-\Gamma_0^2)\right]}{E_{10}^2+(\hbar\Gamma_0)^2}\right\}.\end{aligned} \tag{5.26}$$

and the total OAC can be written as $\alpha(\omega,I) = \alpha^{(1)}(\omega) + \alpha^{(3)}(\omega,I)$. Here ϵ_0 and μ are the electric and magnetic permeability, σ_s is the carrier density, I is the intensity of the the incident light with x-polarization, n_r is the refractive index of medium, c is the vacuum speed of light, E_{10} denotes the transition energy between the states, $M_{ij} = |\langle\psi_i|er\cos\phi|\psi_j\rangle|$ $(i, j = 0, 1)$ are the off-diagonal matrix elements of the dipole moment and $\Gamma_0 = 1/T_0$ is phenomenological operator (Kilic et al., 2017).

The expressions of linear and the third-order nonlinear relative refractive index changes (RICs) are given by, respectively (Li et al., 2012):

$$\frac{\Delta n^{(1)}(\omega)}{n_r} = \frac{1}{2n_r^2\epsilon_0}|M_{10}|^2\sigma_s\left[\frac{E_{10}-\hbar\omega}{(E_{10}-\hbar\omega)^2+(\hbar\Gamma_0)^2}\right] \tag{5.27}$$

and

$$\begin{aligned}\frac{\Delta n^{(3)}(\omega, I)}{n_r} &= -\frac{\mu c}{4n_r^3\epsilon_0}|M_{10}|^2\frac{\sigma_s I}{[(E_{10}-\hbar\omega)^2+(\hbar\Gamma_0)^2]^2}\\ &\times\left[4(\varepsilon_{10}-\hbar\omega)|M_{10}|^2-\frac{(M_{11}-M_{00})^2}{E_{10}^2+(\hbar\Gamma_0)^2}\{(E_{10}-\hbar\omega)\right.\\ &\left.\times\left[E_{10}(E_{10}-\hbar\omega)-(\hbar\Gamma_0)^2\right]-(\hbar\Gamma_0)^2(2E_{10}-\hbar\omega)\}\right]\end{aligned} \tag{5.28}$$

The total magnitude of the RIC is written as $\Delta n(\omega, I)/n_r = \Delta n^{(1)}(\omega)/n_r + \Delta n^{(3)}(\omega, I)/n_r$.

5.4.3 Results and discussion

In this section, we present and discuss the numerical results concerning the influence of THz laser field on a typical GaAs quantum dot structure with an on-center screened impurity. The physical parameters used in our calculations are (Xie, 2010; Yuan et al., 2015): $m^* = 0.067m_0$ (m_0 being the free electron mass), charge density of $\sigma_s = 5\times10^{24}$ m^{-3}, $T_0 = 0.14$ ps, $\mu = 4\pi\times10^{-7}$ $\mathrm{Hm^{-1}}$, $n_r = 3.2$ and $I = 1.5\times10^{10}$ $\mathrm{W/m^2}$.

Before discussing the optical response of the system, it would be beneficial to investigate the effect of screening parameter on energy states. Hence, the dependence of energies of E_0 and E_1 on $\lambda-$parameter for several values of laser-dressing parameter and confinement strength is presented in Figure 5.25. As is apparent from Figure 5.25 (a), the increase of α_0 leads to a significant rise in the E_0 whereas E_1 is less affected. In Figure 5.25 (b), we can clearly see that augmentation in $\hbar\omega_0$ gives cause for a remarkable increase in E_1 while inducing relatively less increase in the ground-state energy. As is seen from both figures, the greater values of $\lambda-$screening parameter bring about a notably enhancement in the energies.

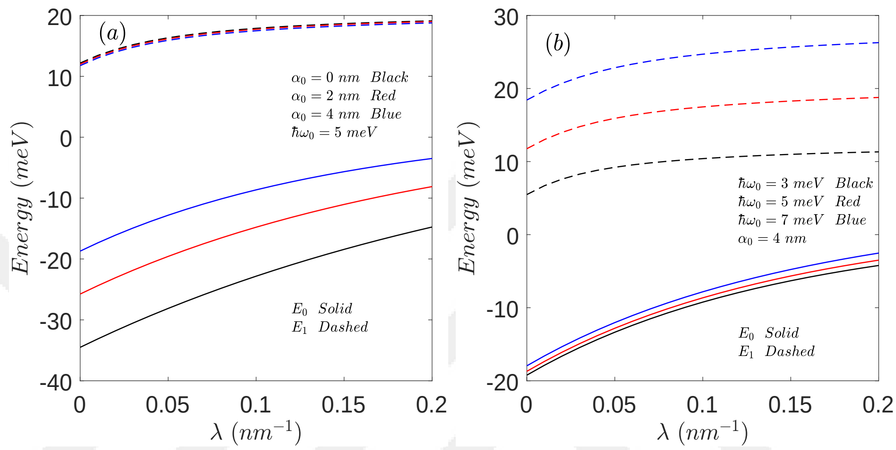

Figure 5.25 Variation of energies of E_0 and E_1 as a function of the screening parameter for different values of (a) laser-dressing parameter and (b) confinement strength

In attempt to understand the behavior of the ground-state binding energy of the laser-dressed system with screened Coulomb impurity, in Figure 5.26 we present the variation of binding energy as a function of laser-dressing parameter for three values of λ and $\hbar\omega_0$. Binding energy is defined by $E_b = E_0^0 - E_0$ where E_0^0 states the ground state energy in the absence of impurity. Figure 5.26 (a) displays clearly an appreciable diminishment in the magnitude of binding energy for higher values of λ. Increment of screening effect brings about weakening interaction between impurity and electron which explains the behavior in Figure 5.26 (a). On the other hand, strengthening in confinement potential brings about an increase in the binding energy as seen from Figure 5.26 (b). The physical reason can be explained by the fact that the greater values of $\hbar\omega_0$ give rise to more localized impurity-related states because of stronger quantum confinement and increment of absolute Coulomb interaction. Moreover, from Figure 5.26 (a) and (b) we observe that the magnitude of impurity binding energy

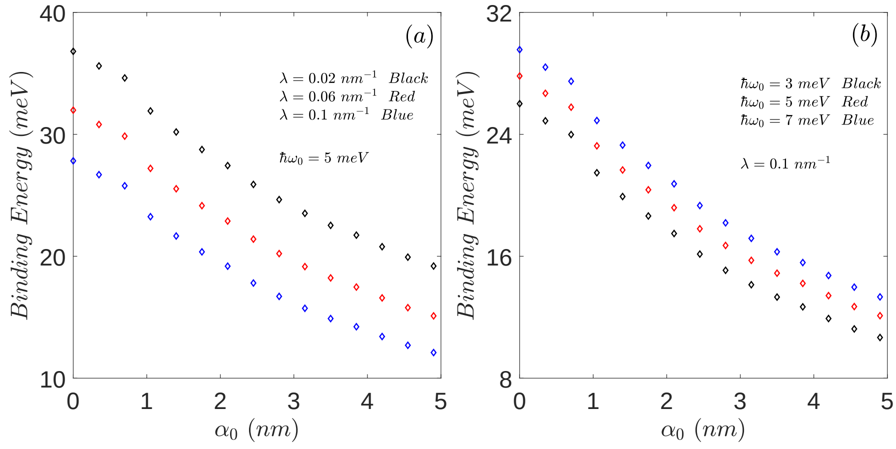

Figure 5.26 Binding energy as a function of laser-dressing parameter for different values of (a) $\lambda-$parameter for confinement of 5 meV, (b) the confinement strength for a fixed $\lambda = 0.1$ nm^{-1}

demonstrates a remarkable decline with increasing laser-dressing parameter owing to increment in the electron-impurity distance, which causes weakening in the strength of the Coulomb interaction.

The investigation of the influences of λ and $\hbar\omega_0$ on the dipole matrix element ($|M_{10}|$) is important for better understanding of the optical response of the system under ITLF. Therefore, in Figure 5.27 we exhibit the change of magnitude of $|M_{10}|$ as a function of α_0 for different values of λ and $\hbar\omega_0$. It is clear from Figure 5.27 (a) that the magnitude

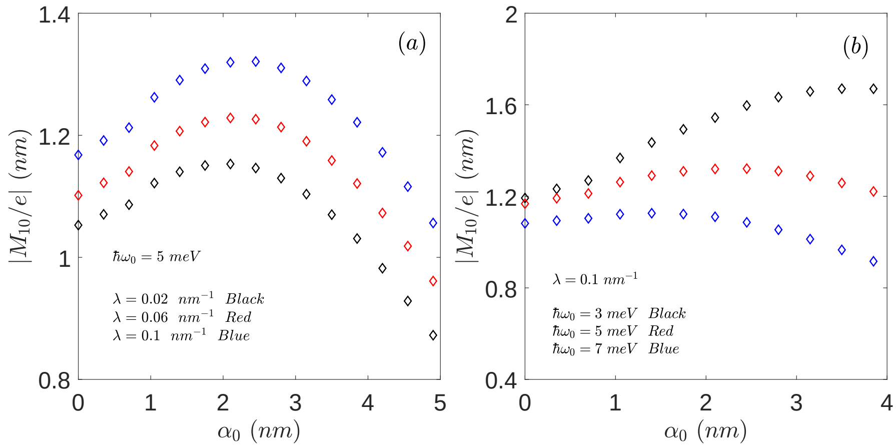

Figure 5.27 Plot of $|M_{10}|$ as a function of the laser-dressing parameter for three values of (a) screening parameter and (b) confinement strength

of $|M_{10}|$ showing an increasing behavior up to specific value of α_0 is followed by a decrease. In addition, the augmentation of $\lambda-$parameter leads to an increment in the absolute value of $|M_{10}|$. Figure 5.27 (b) depicts that the dipole matrix element declines considering higher values of $\hbar\omega_0$. In this figure, remarkable observation is that the magnitude of $|M_{10}|$ enhances with increasing α_0 at the lowest value of $\hbar\omega_0$. However, for the greater values of $\hbar\omega_0$, the variation of $|M_{10}|$ depicts a similar behavior as Figure 5.27 (a).

To investigate the effect of intense laser field on the optical response of system, we display the variation of the OACs and RICs as a function of incident photon energy for $\lambda = 0.1$ nm^{-1} with $\hbar\omega_0 = 5$ meV in Figure 5.28. It would be important to remark that the dashed, dotted and solid lines indicate the linear, third-order nonlinear and the total optical characteristics, respectively. The greater values of α_0 lead to a diminishment in the height of the resonance peaks of the OACs whereas cause an increment in the magnitude of RICs except the value of $\alpha_0 = 2$ nm in both figures. The physical interpretation of Figure 5.28 can be explained by the change in the absolute value of dipole matrix element by the increase in the α_0−parameter and this result is consonant with Figure 5.27. The peak positions of OACs and RICs move to the lower energy values (red-shift) with increasing α_0 owing to diminishment in the energy interval between states E_0 and E_1, which could be easily seen in Figure 5.25 (a).

Another important examination on the optical characteristics of the system is the effect of screening. Therefore, the variations of the optical coefficients as a function of

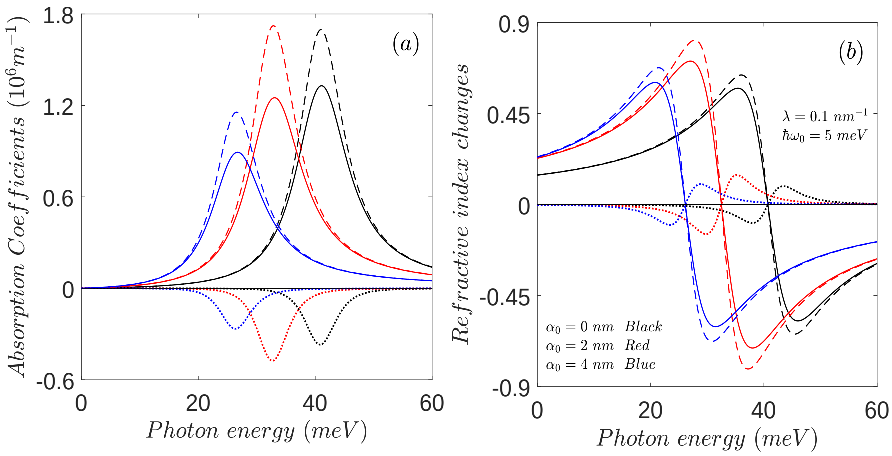

Figure 5.28 The change in the linear, third-order nonlinear and total (a) OACs and (b) RICs as a function of the photon energy for three values of α_0 with $\lambda = 0.1$ nm^{-1} and $\hbar\omega_0 = 5\ meV$

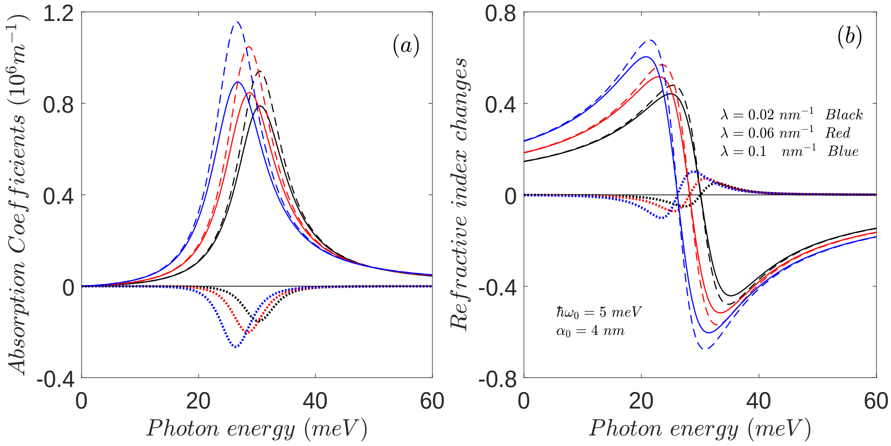

Figure 5.29 (a) Optical absorption coefficients and (b) refractive index changes versus incident photon energy for different values of $\lambda-$screening parameter

incident photon energy for several values of $\lambda-$secreening parameter considering the fixed values α_0 = 4 nm and $\hbar\omega_0$ = 5 meV are shown in Figure 5.29 (a) and (b). It can be clearly observed that in compliance with the previously presented energy and $|M_{10}|$ data, increment in $\lambda-$parameter leads to an increase in the peak heights of the linear, third-order nonlinear and total OACs and RICs while the peak positions of OACs and RICs shift toward to the lower energy region.

Figure 5.30 demonstrates the variation of optical absorption coefficients and refractive index changes versus the photon energy for different confinement strength for laser-dressing parameter of 4 nm. From both figures, we evidently observe that augmentation of confinement strength brings about a considerable reduction in the amplitudes of OACs and RICs. Besides, strengthening in confinement causes a blue-shift in the optical response on account of enhancement in the transition energy.

It may be significant also to examine the effects of the screening parameter and confinement frequency in the magnitude of resonant peak values of total OAC and RIC. Hence, Figure 5.31 (a) and (b) depict the changes in the peak values of OAC and RIC at resonance frequency as a function of α_0 for different values of λ and $\hbar\omega_0$.

The main figures of Figure 5.31 (a) and (b) shows that the resonant peak values of OAC and RIC increase for greater values of λ and exhibit a decreasing behavior for stronger laser field. It should be pointed out that the intriguing behavior of the

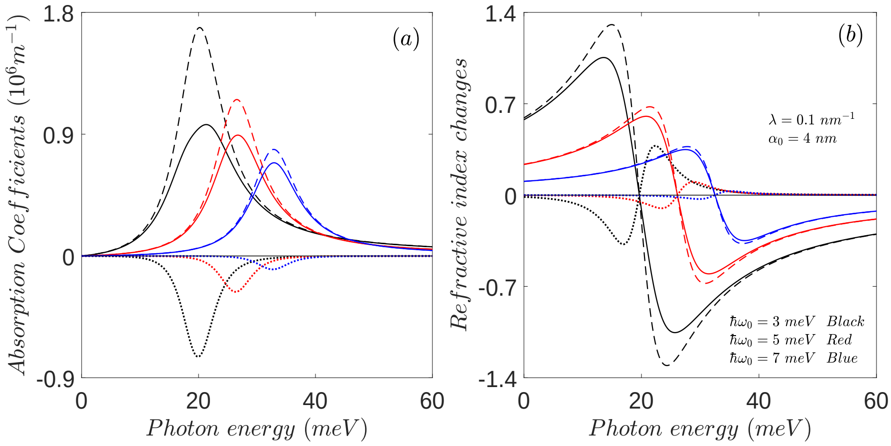

Figure 5.30 (a) OACs and (b) RICs vs the photon energy for different values of $\hbar\omega_0$. We set $\alpha_0 = 4$ nm and $\lambda = 0.1$ nm^{-1}

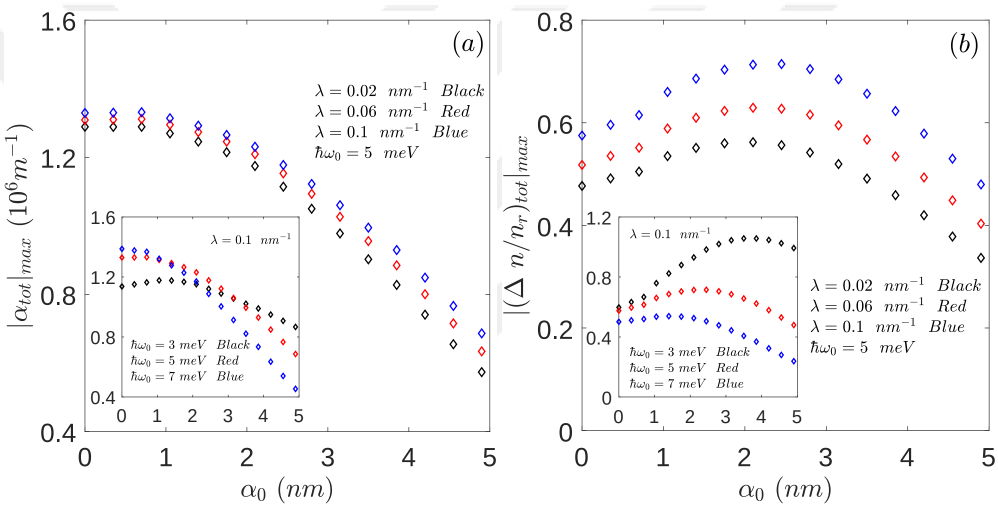

Figure 5.31 The maximum values of OACs and RICs versus α_0 for varying values of λ and $\hbar\omega_0$

maximum value of total absorption coefficient in the inset figure of Figure 5.31 (a). The highest value of $|\alpha_{tot}|_{max}$ is obtained for a specific confinement strength value ($\hbar\omega_0$ = 7 meV) at lower laser dressing parameters whereas it is highest for $\hbar\omega_0$ = 3 meV at greater values of α_0. From the inset figure of Figure 5.31 (b), it can be readily seen that the maximum value of total RIC decrease for higher values of $\hbar\omega_0$. Further, the resonant peak of RIC increases for lower values of α_0 value but this magnitude starts to decline with the strengthening in the ILF.

5.5 Tailoring the optical properties of quantum ring irradiated by THz laser

5.5.1 Introduction

Recent years have witnessed the exhaustive attention paid on quasi-zero-dimensional semiconductor nanostructures, both from theoretical and experimental perspectives (Kilic et al. (2019) and references therein). This enormous interest is triggered by their prospective application potential in the development of novel optoelectronic devices, like terahertz detectors, solar cells, memory devices etc. (Chakraborty et al., 2018; Ganguly et al., 2017; Li et al., 2017; Mohammadi et al., 2016; Martinez-Orozco et al., 2017). Specifically, owing to their atom-like properties as well as high flexibility in size and shape, structures with a ring-geometry stand as a suitable basis for the study of quantum interference effects (Kilic et al. (2019) and references therein). By the proper adjustment of the radius and width of quantum ring (QR), the energy levels of charge carriers can be well controlled.

On the other hand, it is also feasible to externally manipulate the system so as to obtain nanostructures with desired operating frequency (Duque et al., 2012b; Salehani et al., 2015). Several efforts have been devoted to examine the electronic and optical characteristics of QR structures (Vinasco et al., 2019). Räsänen and Aichinger have researched the electronic properties of relatively large QRs under magnetic fields (Räsänen & Aichinger, 2009). Exciton related optical properties of a two-dimensional (2D) ring under the exposure of magnetic flux have been investigated by Santander et al. (Gonzalez-Santander et al., 2011). Acosta and coworkers reported the effects of electric field and donor impurity on optical absorption and refractive index changes in a semiconductor QR (Acosta et al., 2016). Duque et al. have researched the properties of some donor-impurity-induced changes in the nonlinear optical properties of coupled dot-ring nanostructure (Duque et al., 2015). The effects of eccentricity and electric field on the optical properties of a GaAs/AlGaAs elliptic QR have been studied by Bejan et al. (Bejan et al., 2018). A detailed work on the impurity-related absorption, second- and third-harmonic generation of a 2D QR subjected to external

B-field has been conducted by Niculescu et al. (Niculescu & Bejan, 2017). It also has been reported that laser and magnetic fields can be used to drive nanostructures towards modulating the electronic and optical characteristics in a controllable way (Bejan, 2016a; Safarpour et al., 2014; Vaseghi et al., 2015). A magnetic field causes an oscillatory behavior of carriers's energy levels (Xie et al., 2008) while high-frequency laser field modifies the confinement potential ending up with substantial changes in the energy spectrum and optical response (Barseghyan et al., 2017; Laroze et al., 2016).

Recently, several works reported the effects of intense laser field (ILF) on the electronic spectra and optical properties of nanoscale systems (Kilic et al. (2019) and references therein). Quantum structure-laser radiation interaction, giving rise to a diversity nonlinear phenomena, was generally examined within the dressed-atom approach, which is valid in the non-resonant region (Eseanu, 2011; Wang et al., 2018). Radu and coworkers investigated the one-electron energy states and intraband optical absorption coefficients in QR under linearly polarized ILF by discussing the influence of the light polarization (Radu et al., 2014). Intraband optical absorption in a laser-driven GaAs/GaAlAs 2D quantum dot and QR with hydrogenic donor impurity is studied by Barseghyan et al. (Barseghyan et al., 2017). Theoretical results given in Reference (Barseghyan, 2016a) point out the well-controlled optical spectrum of ring-like nanostructure by simultaneous act of hydrostatic pressure and laser radiation. The effect of the presence of ILF and external lateral electric field on the single-electron states in impurity doped semiconductor nanorings was exposed by Barseghyan (Barseghyan, 2016b). Results of Reference (Baghramyan et al., 2017) reveal the evolution of molecular states and intraband absorption in coupled QRs structure subjected to intense THz radiation and electric fields. Reference (Chakraborty et al., 2018) presents the ILF-induced changes in the electronic and optical properties in an isotropic and anisotropic QRs modeled by a finite square-well type potential. Lately, Vinasco et al. discussed the how the electronic energies and accordingly the dipole matrix elements in 2D circular QR respond to applied magnetic field and polarization of ILF (Vinasco et al., 2019).

Even though, many works studied the ILF-induced changes in the electronic energy spectra and nonlinear optical properties in single QRs, to the best of our knowledge, a research on the circularly polarized ILF-induced optical properties in QRs with more realistic confinement potential other than the square-well type has not been performed up to now. The purpose of the present work is to address the dependence of total optical absorption coefficient (TOAC), total relative refractive index changes (TRIC) and third-harmonic generation (THG) of THz laser-driven 2D QRs. Theoretical survey is conducted to get insight of the optical response in QR system with respect to ring parameters and influence of external magnetic and laser fields.

The layout of the paper is organized as follows: Brief presentation of the theoretical outline given in Section 5.5.2 is followed by the numerical results in Section 5.5.3.

5.5.2 Theoretical outline

We focus on a single 2D QR irradiated by THz laser radiation where the electrons localized to a 2D plane $(x-y)$ are under the influence of external static magnetic field $\vec{B} = B\hat{e}_z$ in the growth direction. For the lateral confinement of charge carriers we chose a parabolic potential with a centrally-localized Gaussian peak with a form $V(r) = V_0\, e^{-r^2/d^2}$ (Räsänen et al., 2007). Interaction of QR with a non-resonant, monochromatic, right-hand circularly polarized ILF of frequency Ω is tackled within the high-frequency Floquet approach. In this regime, the motion of electron is designated by the potential dressing the time-average of the THz radiation field: $\langle V_d(\mathbf{r},\alpha_0)\rangle = 1/T\int_0^T V(\mathbf{r}+\boldsymbol{\alpha}(t))dt$. Here $T = 2\pi/\Omega$ denotes the period of the incident high-frequency laser light and the electron motion in THz radiation is defined by $\boldsymbol{\alpha}(t) = \alpha_0(\hat{x}\cos\Omega t + \hat{y}\sin\Omega t)$. $\hat{x}$ and $\hat{y}$ represent the unit vectors orthogonal to the direction of propagation of the laser light and $\alpha_0 = eA_0/m^*\Omega$, called the "laser-dressing intensity parameter", comprises both the intensity and frequency of the laser field (Pont & Gavrila, 1990). For a comprehensive overview regarding this approach, the reader may refer to Reference (Lima et al., 2008, 2009b). Then the Hamiltonian of QR system with ILF-modulated potentials is written as follows:

$$H = \frac{1}{2m^*}(\mathbf{p}+e\mathbf{A})^2 + \frac{1}{2}m^*\omega_0^2\left(r^2+\alpha_0^2\right) + V_0\ exp\left(-\frac{r^2+\alpha_0^2}{d^2}\right)I_0\left(\frac{2r\alpha_0}{d^2}\right), \tag{5.29}$$

where r is the radial coordinate, m^* is electronic effective mass and e elementary charge. The vector potential $\mathbf{A}(\hat{r},\hat{\phi},\hat{z}) = (0, Br/2, 0)$ is associated with the external uniform magnetic field applied along the z-direction. Second and third terms appearing in Eq. (5.29) are the analytical expressions of the laser-dressed parabolic potential of confining frequency ω_0 and Gaussian peak of depth of V_0 and range of d (Kilic et al., 2018). $I_0(x)$ appearing in the last term is the modified Bessel function.

The axial symmetry of the system allows one to express the wave function as $\psi_{nm} = R_{nm}e^{im\phi}/\sqrt{2\pi}$ and then the Eq. (5.29) in dimensionless form reads to

$$\begin{aligned} &- \frac{1}{2}\frac{d^2R_{nm}(r)}{dr^2} + \left[\frac{m^2}{2r^2} + \frac{m\gamma_c}{2} + \frac{1}{2}\left(\frac{\gamma_c}{2}\right)r^2\right. \\ &+ \left.\frac{1}{2}\gamma_0^2\left(r^2+\alpha_0^2\right) + V_0\ exp\left(-\frac{r^2+\alpha_0^2}{d^2}\right)I_0\left(\frac{2r\alpha_0}{d^2}\right)\right]R_{nm}(r) = \varepsilon_{nm}R_{nm}(r) \end{aligned} \tag{5.30}$$

with n and m being the radial and magnetic quantum numbers, respectively. Here we define $\gamma_c = \hbar\omega_c/E_h^*$ and $\gamma_0 = \hbar\omega_0/E_h^*$ with cyclotron frequency $\omega_c = eB/m^*$ and the effective Hartree energy $E_h^* = \hbar^2/m^*a_0^{*2}$ used as energy scale. In this work, the calculation of eigen energies with corresponding eigen functions is accomplished numerically by means of the finite element method in one dimension which is based on the Galerkin approach and described in a weak formulation (Pask et al., 2001; Zienkiewicz et al., 2005). In this variational expansion method, the basis functions are strictly local, piecewise polynomials in real space. Note that to obtain the optically active states considered in the investigation of TOAC, TRIC and THG, the numerical solution of the Eq. (5.30) is done at least twice.

5.5.3 Results and discussion

In this work, we carried out calculations for a laser-driven GaAs-based QR structure with the following chosen parameters: $m^* = 0.067m_e$ (m_e is the free-electron mass), $\varepsilon_r = 10.24$, $\mu = 4\pi\times10^{-7}$ Hm^{-1}, $n_r = 3.2$, $\sigma_s = 5\times10^{24}$ m^{-3}, $I = 5\times10^{9}$ W/m^2, and $\Gamma_0 = 0.14$ ps^{-1}. Initially, we analyze the behavior of the TOAC and TRIC against to incident photon energy which is followed by the variation of the THG coefficient. We should note that, throughout the first and second part of the presented results, notations for the eigen energies (eigen functions) differ from each other.

5.5.3.1 Absorption coefficients and relative refractive index changes

Within the scheme of the compact density-matrix approach, linear and third-order nonlinear contributions to the TOAC are given to be (Mora-Ramos et al., 2012a; Rezaei et al., 2010; Gambhir et al., 2013):

$$\alpha^{(1)}(\omega) = \omega\sqrt{\frac{\mu}{\epsilon_r}}\frac{\sigma_s|M_{10}|^2\hbar\Gamma_0}{(E_{10}-\hbar\omega)^2+(\hbar\Gamma_0)^2} \tag{5.31}$$

$$\begin{aligned}\alpha^{(3)}(\omega,I) &= -\omega\sqrt{\frac{\mu}{\epsilon_r}}\left(\frac{I}{2n_r\epsilon_0 c}\right)\frac{\sigma_s\hbar\Gamma_0|M_{10}|^2}{[(E_{10}-\hbar\omega)^2+(\hbar\Gamma_0)^2]^2}\\ &\times\left\{4|M_{10}^2|-|M_{11}-M_{00}|^2\times\frac{\left[3E_{10}^2-4\varepsilon_{10}\hbar\omega+\hbar^2(\omega^2-\Gamma_0^2)\right]}{E_{10}^2+(\hbar\Gamma_0)^2}\right\}.\end{aligned} \tag{5.32}$$

TOAC is a sum of $\alpha^{(1)}(\omega)$ and $\alpha^{(3)}(\omega,I)$. Withal, the TRIC consist of the following linear and nonlinear terms, respectively (Li et al., 2012; Liu et al., 2012):

$$\frac{\Delta n^{(1)}(\omega)}{n_r} = \frac{1}{2n_r^2\epsilon_0}|M_{10}|^2\sigma_s\left[\frac{\varepsilon_{10}-\hbar\omega}{(\varepsilon_{10}-\hbar\omega)^2+(\hbar\Gamma_0)^2}\right] \tag{5.33}$$

$$\frac{\Delta n^{(3)}(\omega,I)}{n_r} = -\frac{\mu c}{4n_r^3\epsilon_0}|M_{10}|^2\frac{\sigma_s I}{[(E_{10}-\hbar\omega)^2+(\hbar\Gamma_0)^2]^2}$$

$$\times\Bigg[4(\varepsilon_{10}-\hbar\omega)|M_{10}|^2-\frac{(M_{11}-M_{00})^2}{E_{10}^2+(\hbar\Gamma_0)^2}\{(E_{10}-\hbar\omega) \tag{5.34}$$

$$\times\Big[E_{10}(E_{10}-\hbar\omega)-(\hbar\Gamma_0)^2\Big]-(\hbar\Gamma_0)^2(2E_{10}-\hbar\omega)\Big\}\Bigg]$$

Here μ refer to the permeability of the system, I is the incident optical intensity of probe field, n_r is the material refractive index, c is the light speed in vacuum, σ_s signifies the carrier density, Γ_0 is the phenomenological relaxation rate (Kilic et al., 2018). For the examination of the optical coefficients, the energy levels and wave functions taking part in the transitions are selected to be $E_0 = \varepsilon_{00}$, $E_1 = \varepsilon_{11}$, $\varphi_0 = \psi_{00}$, $\varphi_1 = \psi_{11}$ where $E_{ij} = E_j - E_i$ defines the transition energy. The incident probe light is presumed throughout the x-axis so $\mu_{ij} = | < \varphi_j | r\cos\theta | \varphi_i > |$ $(i, j = 0, 1)$ are the matrix elements of the dipole moment (Kilic et al., 2018).

For proper understanding of the nonlinear optical characteristics, it is essential to examine the modification of the confining potential arising from ILF-QR interaction and the evolution of the electronic energy spectrum of the structure (Vinasco et al., 2019). Therefore, initially in Figure 5.32(a) and (b) (insets) we illustrate the ILF-induced changes on the QR potential for two values of B-field strength (confining frequency) and V_0-parameter ($d-$parameter) of Gaussian peak, respectively. The worth considering feature of the ILF-effect is the reduction of the Gaussian peak depth accompanied by an upward shift in the bottom of QR. Besides, the point to stress is that ILF yields to a slight rise in the effective ring radius. Another interesting observation is seen from the inset of Figure 5.32(b) for the $d-$parameter which accounts for the spatial extension of Gaussian peak. In case of ILF-parameter of 7 nm, even though the preserved axial symmetry of the ring a disruption from the Gaussian form takes place for $d = 6$ nm.

In Figure 5.33 we exhibit the energy-level structure in QR as a function of magnetic field considering two values of laser-dressing parameter and confinement frequency.

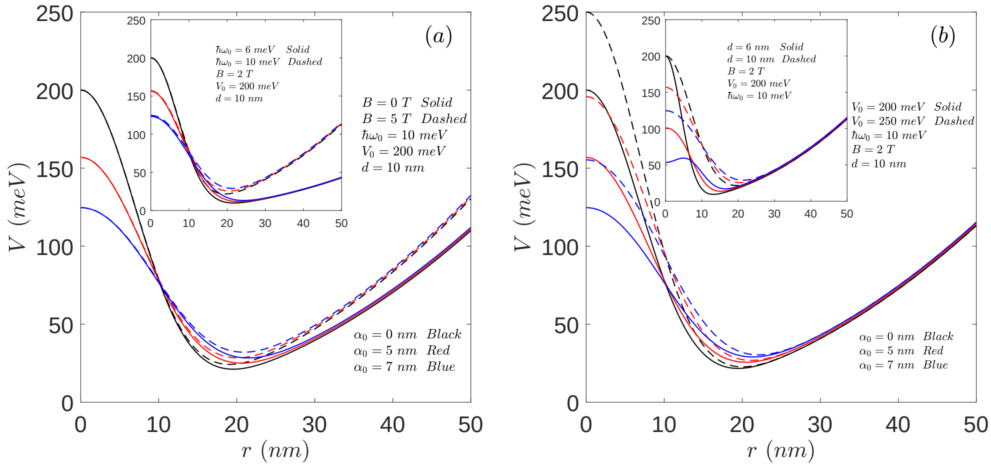

Figure 5.32 Schematic representation of the 2D QR model along the radial direction, considering several values of laser radiation parameter and (a) B and $\hbar\omega_0$, (b) V_0- and d- parameters

Noticeable characteristic of the lowest few energy levels for a radial quantum numbers

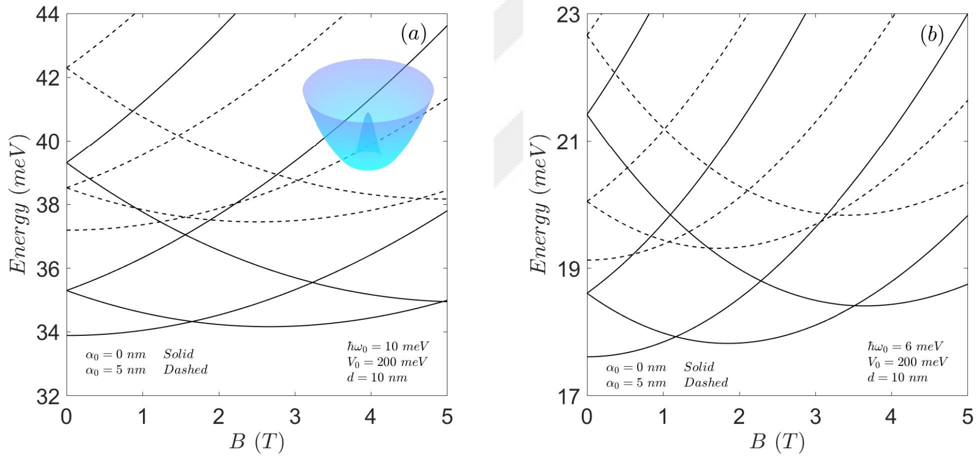

Figure 5.33 Single-electron energy states of a 2D QR as a function of magnetic field for the cases without/with ILF-effect for confinement strengths at (a) $\hbar\omega_0$ = 10 meV, (b) $\hbar\omega_0$ = 6 meV. The inset shows the schematic representation of the potential model of laser-driven system

$n = 0, 1$ and five angular quantum numbers ($m = 0, \pm 1, \pm 2$) seen from Figure 5.33(a) and (b) is the upward shift in the energies. Under the modulation of magnetic field the ground state changes to one of $m \neq 0$ while this alternation emerges at comparatively diminutive strength of magnetic field in a laser-driven system. Changes induced in the amplitude of Gaussian peak by the ILF give rise to a weakening in confining potential which brings about the crossing point between the energies to occur at more lower values of B. For the parabolic confinement of $\hbar\omega_0 = 6$ meV, further diminution of the

B-value for energy level crossings is apparent. Similar accidental degeneracies have been reported recently by Vinasco et al. for circular 2D QRs modeled with a finite square well type potential (Vinasco et al., 2019). We have to remark that, in case of the action of linearly polarized ILF, electronic structure evolution would be affected as a result of the loss in the system's symmetry (Vinasco et al., 2019).

To ascertain the magnetic field-dependence of the optical properties, in Figure 5.34 we present the TOAC and TRIC in QR considering the absence/presence of ILF by taking into account the energy levels participating in the transitions to be ε_{00} and ε_{11}. Increment in the laser-dressing parameter results in a slight red-shift in the resonant

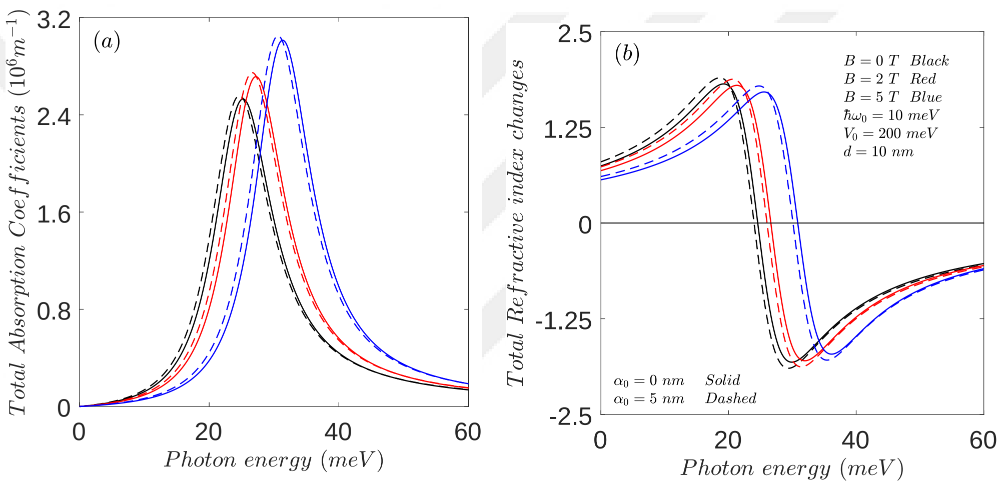

Figure 5.34 Variation of the TOAC and TRIC in QR as a function of incident photon energy for varying magnetic fields

peak energies for which the underlying reason is the decrement in the transition energies. In spite of that peak magnitudes of the optical coefficients are less affected by radiation field. Moreover, stronger magnetic field causes a strengthening in the effective confinement potential which leads to an increase in the energy intervals and consequently the resonant peaks move to higher energy region. Besides, it can noticed that $B-$induced considerable augmentation in the absorption coefficients takes place while $\Delta n^{(T)}(\omega, I)/n_r$ shows a minor decrease. The interplay between the dipole matrix elements and transition energies determine the behavior of the optical properties of QR.

Dependence of the optical characteristics of the laser-driven QR on the strength of parabolic potential is depicted in Figure 5.35. Weakening in confinement potential

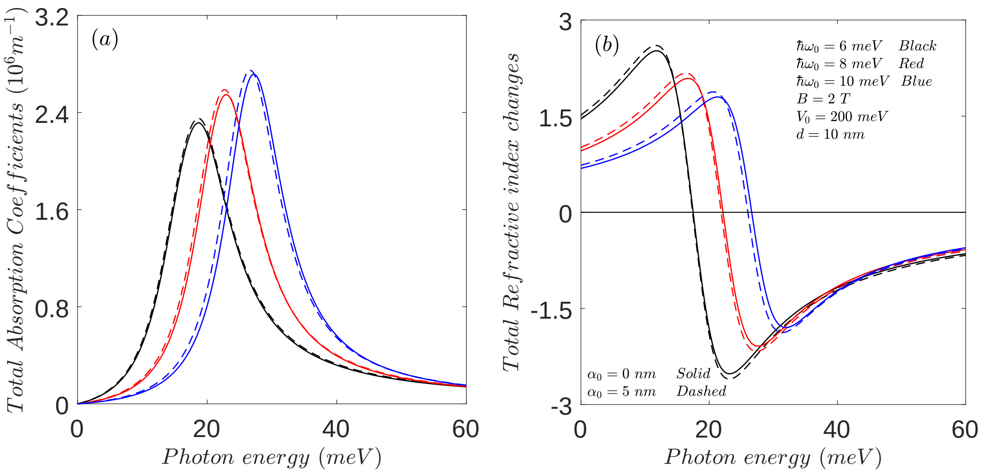

Figure 5.35 Optical properties towards photon energy for particular values of confining potential in QR with α_0 = 0 nm and 5 nm

causes a decrease in the energy intervals between the optically allowed intersubband levels. Therefore the peak position of optical characteristics shift to lower energies while the peak magnitude of TOAC (TRIC) decreases (augments significantly). Peak amplitudes of the optical response are less sensitive to the THz radiation.

To find out the effect of the structure parameters of the ring, Figure 5.36 illustrates the variation of the optical characteristics for the range parameter of Gaussian peak. With an increment in d-parameter, the peak positions of $\alpha^{(T)}(\omega,I)$ and $\Delta n^{(T)}(\omega,I)/n_r$

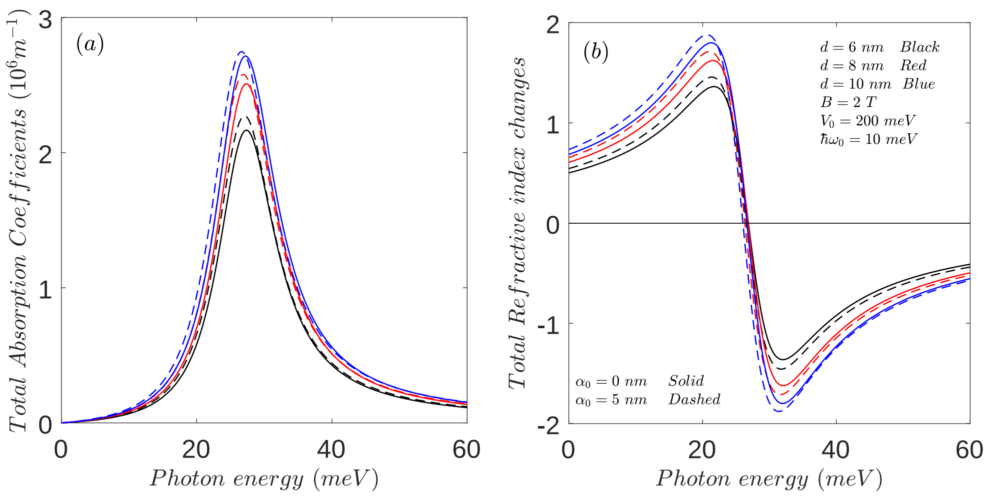

Figure 5.36 Optical response of the system for varying range parameters of Gaussian potential considering two values of laser-dressing parameter

remain almost unchanged however the peak magnitudes enhance considerably. The effect of ILF is more pronounced for a system with smaller $d-$values, comparatively. On the other hand, variation in the depth of the Gaussian potential on the optical response of the system is seen in Figure 5.37. The effects in the increment of V_0

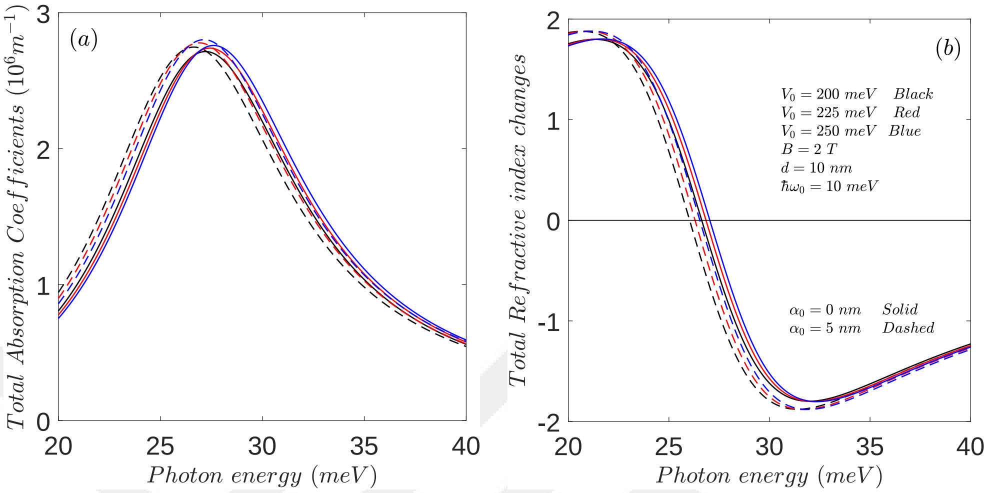

Figure 5.37 Optical coefficients with respect to the photon energy at several values of V_0-parameter and laser-dressing parameter

parameter are further evident on the peak amplitudes of TOACs accompanied by the nearly close positions whereas ILF-introduced small boosts in the magnitudes of the optical characteristics is also standing out.

5.5.3.2 Third-harmonic generation

To analyze the THG coefficient, we take into account the dipole transitions only between levels with $\Delta m = \pm 1$. Therefore, the energy states and the wave functions are chosen as follows: $E_0 = \varepsilon_{00}$, $E_1 = \varepsilon_{01}$, $E_2 = \varepsilon_{10}$, $E_3 = \varepsilon_{11}$, $\varphi_0 = \psi_{00}$, $\varphi_1 = \psi_{01}$, $\varphi_2 = \psi_{10}$, $\varphi_3 = \psi_{11}$. By the virtue of the compact density matrix scheme, THG susceptibility for intersubband transitions is obtained as (Duque et al., 2013; Mohammadi et al., 2016; Yu & Wang, 2011):

$$\chi_{3\omega}^{(3)} = \frac{\sigma_s}{\varepsilon_0} \frac{M_{01} M_{12} M_{23} M_{30}}{(\hbar\omega - E_{10} - i\hbar\Gamma_0)(2\hbar\omega - E_{20} - i\hbar\Gamma_0/2)(3\hbar\omega - E_{30} - i\hbar\Gamma_0/3)} .$$

Here σ_s is the electronic density designated to be 5×10^{24} m^{-3}. By assuming the linearly polarized incident probe electromagnetic field along x-axis, $M_{ij} = |\langle\varphi_j|er\cos\phi|\varphi_i\rangle|$ $(i, j = 0, 1, 2, 3)$ are the matrix elements of the dipole moment, $E_{k0} = E_k - E_0$ $(k = 1, 2, 3)$ depicts the transition energies and $\Gamma_0 = 1/T_0$ (chosen T_0 is 1 ps) is the interstate damping rate.

It is important to see the general behavior of ILF-dependent dipole matrix element product for better understanding of the optical response of system. Therefore, in Figure 5.38 we present the absolute value of dipole matrix element product as a function of magnetic field, confinement strength, the range and depth of Gaussian potential for three different values of laser-dressing parameter. As is clearly seen from

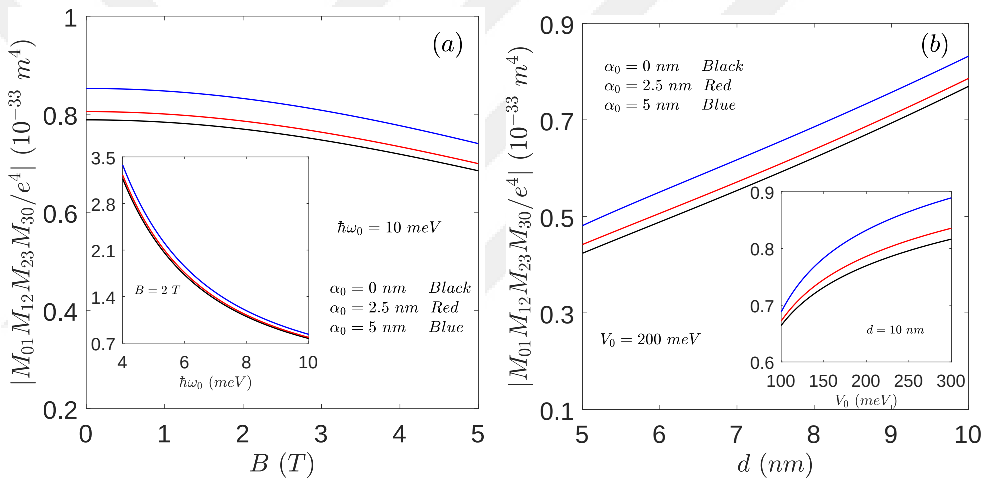

Figure 5.38 $|M_{01}M_{12}M_{23}M_{30}|$ with respect to (a) B and $\hbar\omega_0$, (b) d and V_0 for different values of laser-dressing parameter

Figure 5.38 (a) and (b), the matrix element product increases with augmentation of ILF as a consequence of the increment of overlaps among wave functions. As is apparent from Figure 5.38(a), the $|M_{01}M_{12}M_{23}M_{30}|$ decreases with strengthening in confinement potential and less slightly with magnetic field. Contrary to Figure 5.38 (a), for the higher values of Gaussian peak parameters (d and V_0) the $|M_{01}M_{12}M_{23}M_{30}|$ it shows a gradual enhancement.

In an effort to analyze the impact of magnetic field on single-electron energy spectra, a few low energy states (ε_{nm}) are exhibited in Figure 5.39 as a function of magnetic field considering different parameters representing the system under debate. As is

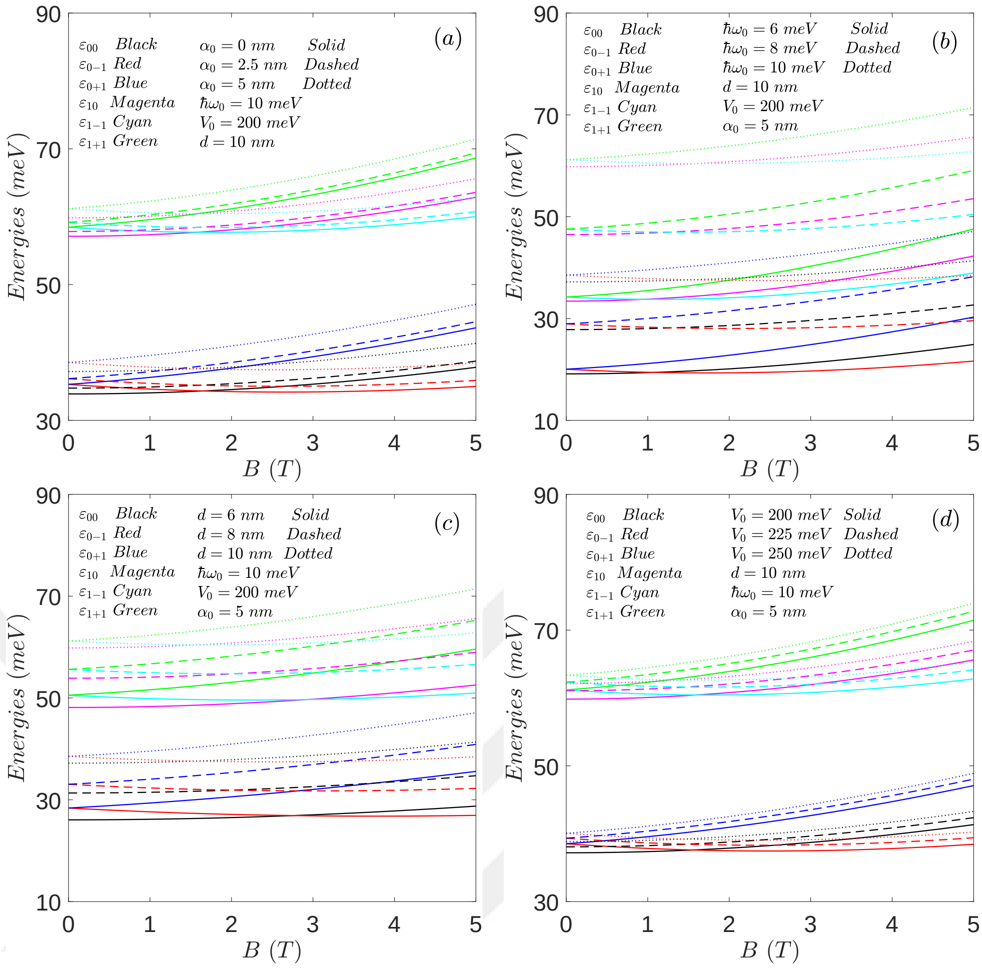

Figure 5.39 Magnetic field dependence of energies for different values of (a) laser-dressing parameter, (b) confinement strength, (c) the range and (d) depth parameters of Gaussian potential

seen from the figure, when the magnetic field is turned-on, the energy levels are significantly affected and a typical Aharonov-Bohm like oscillations are observed. In Figure 5.39 (a), the energies increase with greater values of laser-dressing parameter and the position of crossing point, which occurs between ε_{00} (ε_{10}) and ε_{0-1} (ε_{1-1}), moves to lower magnetic field values. From Figure 5.39 (b), we can clearly see that enhancement in confinement strength leads not only an increase the energies but also a shift in the position of crossing point toward higher magnetic field values. The effects of range and depth parameters on the energy spectra are demonstrated in Figure 5.39 (c) and (d). The energies shows more rise with the augmentation of d values while less increment for greater values of V_0. In addition, the position of crossing point moves to lower magnetic field values due to increase in d or V_0.

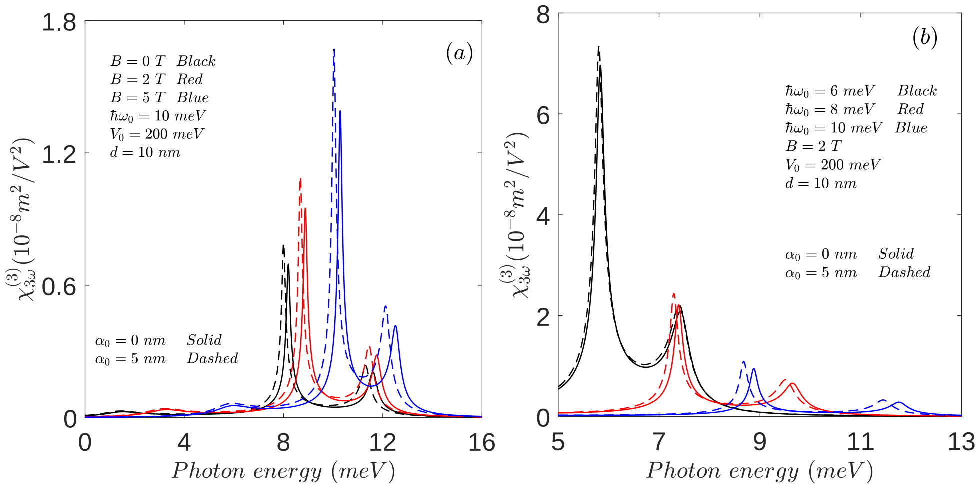

Figure 5.40 (a) Plot of THG against the photon energy for several values of (a) B, (b) $\hbar\omega_0$ considering α_0 of 0 and 5 nm. We use V_0 = 200 meV and d = 10 nm

In Figure 5.40(a), the variation of $\chi^{(3)}_{3\omega}$ against the photon energy for different values of α_0 and magnetic field is shown. We evidently observe that there are three resonance peaks each corresponding to ω_{10}, $\omega_{30}/3$ and $\omega_{20}/2$, respectively. The notable point is that the dominant peak belonging to $\omega_{30}/3$ identifies the THG coefficient for the system discussed. It is seen that the THG coefficient peaks augment with the increasing external field intensities. Moreover, as is to be expected, the increment in laser (magnetic) field causes a shift in the low-energy (high-energy) region due to the decrease (increase) in the transition energies. In addition, ILF-modulated variation in THG prevails at higher B-field values, imparting to a strong impact of ILF in narrower QRs (Chakraborty et al., 2018). Note that in Figure 5.40(b) and subsequent figures, the resonant peak associated with ω_{10} is not displayed due to its diminutive contribution to the THG coefficient. Figure 5.40(b) demonstrates the THG versus photon energy considering different laser-dressing parameters and confinement frequency. It seems that ILF induces relatively small change in the THG amplitudes for higher values of confinement strength while causes a respectable increment at its smallest value, which relies on the competition between $\hbar\omega_0$ and α_0. On the other hand the augmentation in $\hbar\omega_0$ leads to a significant decrease in the peak amplitude of $\chi^{(3)}_{3\omega}$. The underlying cause of this can be understood by the remarkable reduction in the absolute value of dipole matrix elements for stronger confinements. In addition, the peak of THG shifts toward the lower-energy region for increasing α_0 whereas its peak goes towards higher-energy region with increasing $\hbar\omega_0$.

To ascertain whether the THG is sensitive to the range parameter of Gaussian peak, in Figure 5.41(a) we exhibit the THG as a function of photon energy for different α_0- and d-values. Increment in these parameters brings about a rise in the main peaks of

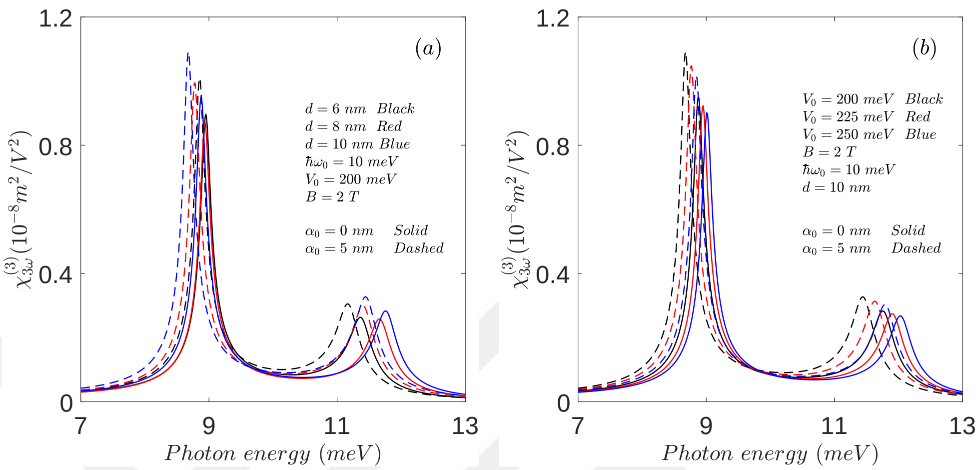

Figure 5.41 The THG coefficient as function of the incident probe field energy with different values of (a) α_0 and d, (b) α_0 and V_0. We set B = 2 T, $\hbar\omega_0$ = 10 meV

THG in compliance with the augmentation monitored in matrix elements. Besides, related with the change in the transition energies, the dominant peak position of THG shifts to lower-energy (higher-energy) values with increasing (decreasing) α_0 (d). Variations of THG with respect to photon energy for varying values of α_0 and V_0 are shown in Figure 5.41(b). The main peak amplitude of THG declines for increasing V_0 while boosts with augmentation in α_0. Moreover, its peak position undergoes a red-shift (blue-shift) for increasing α_0 (V_0) depending on reduction (increment) in transition energies.

It can be beneficial to analyze the influences of the ILF-associated and structure parameters on the main peak height of THG coefficient. Therefore, in Figure 5.42 we plot the dependence of the $|\chi^{(3)}_{3\omega}|_{\max}$ on B, $\hbar\omega_0$, d and V_0 for particular values of α_0.

From Figure 5.42 (a) and (b), we obviously see that the magnitude of resonant peak value of THG enhances when the ILF is turned-on. Figure 5.42 (a) illustrates that the $|\chi^{(3)}_{3\omega}|_{\max}$ improves for greater values of B whereas increment in $\hbar\omega_0$ brings about a

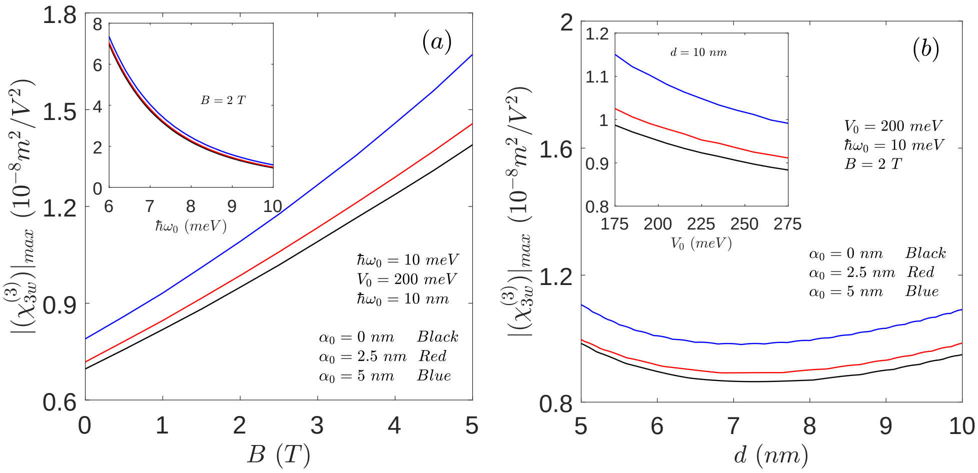

Figure 5.42 The maximum value of THG signal against (a) B and $\hbar\omega_0$, (b) d and V_0 with different values of α_0

crucial reduction. The main figure of Figure 5.42 (b) depicts that the highest resonant peak value decreases up to a specific d-value (about 7.5 nm), while enhances fairly smooth for larger values. The inset of Figure 5.42 (b) reveals stronger confinement potential strengths act in such a way that cause a reduction in the resonant peak value.

Information from the presented results highlight that the peak magnitude/location of the optical coefficients could be tuned properly via the external fields and structural parameters of a QR.

Publications derived from the results of the thesis can be listed as follows:

- Sakiroglu, S., Kilic, D. G., Yesilgul, U., Ungan, F., Kasapoglu, E., Sari, H., & Sokmen, I. (2018). Third-harmonic generation of a laser-driven quantum dot with impurity. *Physica B*, 539, 101-105.

- Kilic, D. G., Sakiroglu, S., & Sokmen, I. (2018). Impurity-related optical properties of a laser-driven quantum dot. *Physica E*, 102, 50-57.

- Kilic, D. G., Sakiroglu, S., Ungan, F., Yesilgul, U., Kasapoglu, E., Sari, H., & Sokmen, I. (2019). Tailoring the optical properties of quantum ring irradiated by Thz laser. *Philosophical Magazine*, 99, 3116-3132.

- Kilic, D. G., Sakiroglu, S., Kasapoglu, E., Sari, H., & Sokmen, I. (2020). Impurity modulated optical response of a disc-shaped quantum dot subjected to laser radiation. *Photonics and Nanostructures - Fundamentals and Applications*, 38, 100748.

- Kilic, D. G., Sakiroglu, S., & Sokmen, I. Screened donor impurity in a two-dimensional quantum dot under THz laser field (in the production process).

CHAPTER SIX
CONCLUSION

This thesis aimed to examine the effects of non-resonant, circularly polarized THz ILF on the impurity-related electronic and optical properties of a 2DQD subjected to an uniform magnetic field. Circularly polarized laser field has been taken within the framework of high-frequency Floquet theory and the analytical expressions of optical properties have been obtained within the compact-density matrix approach. In this study, we have chosen different impurity potentials such as Gaussian, Hydrogenic and screened Coulomb for modelling the presence of impurity. The impurity-related energy eigenvalues and wave functions are obtained numerically by FEM in one dimension which is based on the Galerkin approach and described in a weak formulation. The main results of thesis will be presented in more detail below.

Firstly, we have theoretically investigated the effect of on-center Gaussian impurity on the linear, nonlinear and total optical absorption coefficients (OACs) and refractive index changes (RICs) and third-harmonic generation (THG) of a laser-driven quantum disc subjected to an uniform magnetic field. The results display that not only the position of resonant peak of the linear, third-order nonlinear and total absorption coefficients and refractive index changes but also its magnitude is crucially affected by the strength of intense laser field, parabolic confinement potential, the depth and range of impurity and magnetic field. The peak positions exhibit a red-shift with increasing α_0 whereas show a blue-shift for the higher values of $\hbar\omega_0$, V_0, d and B. On the other hand, it is clearly seen that the magnitudes of impurity binding energy, transition energy, dipole moment matrix elements and consequently the optical coefficients are considerably affected by the laser-dressing parameter. Besides, the presence of on-center impurity substantially affects the peak amplitude and position of THG coefficient. The greater values of $\hbar\omega_0$, V_0, d and B lead to a blue-shift in the peak position of THG while a red-shift is obtained with the higher values of α_0. Furthermore, the results reveal that the THG coefficient with designated values can be obtained by using a properly adjusted parameters. Consequently, the magnitudes of transition energies and geometrical factor exhibit a remarkable sensitivity to the strength of intense laser field, magnetic field, confinement strength and structure parameters of Gaussian impurity.

Afterwards, the influence of non-resonant, circularly polarized THz ILF on the hydrogenic impurity-related electronic and optical properties of a 2DQD has been researched. Also, we have considered the influences of static magnetic field and confinement frequency on the optical spectra of the system. The acquired numerical results indicate that the presence of ILF and impurity causes considerable influence on the ground-state energy whereas the action of magnetic field affects to the excited state energies. The magnitudes of binding energy and $|M_{10}|$ have been remarkably affected by α_0, external uniform magnetic field and confinement strength. Further, the magnitude and position of resonant peak of the OACs and RICs are strongly affected by the presence of ILF. For greater values of α_0, the position of optical coefficients are red-shifted whereas blue-shift is observed with the increment of B and $\hbar\omega_0$.

Subsequently, investigation on the electronic and optical properties of a laser-driven 2DQD including a screened Coulomb impurity has been performed. The numerical results demonstrate that exposing an ILF onto a 2DQD system results in remarkable changes in the impurity binding energy, dipole moment matrix elements and the optical characteristics of the system. By altering the magnitude of confinement frequency, laser-dressing and $\lambda-$screening parameter, shifts in the resonant peak positions of OACs and RICs are observed. On the other hand, enhancement in the peak amplitudes of OACs and RICs is observed for the lower values of α_0 and $\hbar\omega_0$ while this increment is seen with increasing the screening effect.

In addition, the optical response of a 2DQR consisting of parabolic potential and center-located Gaussian peak by considering the effects of laser and magnetic fields is investigated. Numerically calculated energy states have been utilized to examine the features of total OAC, total RIC and THG coefficient in the QR system. The acquired results indicate that the action of magnetic field causes considerable influence on the energy levels and the crossings between them are affected by ILF and structure parameters. The positions (blue- or red-shift) and amplitudes of the resonant peaks of total OAC and total RIC can be modulated by the intensity of laser radiation, magnetic field and confinement potential strengths. Moreover, the dominant peak amplitude of THG increases with the augmentation of α_0, B and d whereas enhancement in $\hbar\omega_0$ and V_0 leads to a decline. For greater values of B, $\hbar\omega_0$ and V_0, the main peak positions of THG are blue-shifted but red-shift is observed with the increment of α_0 and d.

To sum up, the intensity of the laser field and changing the system parameters can be used to tune the electronic structure, the binding energy of the impurity and the optical response of the system. We hope that the present results could be utilized to improve the design of optoelectronic devices and control of their optical properties.

REFERENCES

A. Lorke, R. L., Govorov, A. O., Kotthaus, J. P., Garcia, J. M., & Petroff, P. M. (2000). Spectroscopy of nanoscopic semiconductor rings. *Physical Review Letters*, *84*, 2223 – 2226.

Abbasi, E., Kafshdooz, T., Bakhtiary, M., Nikzamir, N., Nikzamir, N., & Nikzamir, M. (2016). Biomedical and biological applications of quantum dots. *Artificial Cells, Nanomedicine, and Biotechnology*, *44*, 885 – 891.

Acosta, R. E., Morales, A. L., Duque, C. M., Mora-Ramos, M. E., & Duque, C. A. (2016). Optical absorption and refractive index changes in a semiconductor quantum ring: Electric field and donor impurity effects. *Physica Status Solidi B*, *253*, 744 – 754.

Adamowski, J., Sobkowicz, M., Szafran, B., & Bednarek, S. (2000). Electron pair in a gaussian confining potential. *Physical Review B*, *62*, 4234 – 4237.

Adams, F., & Barbante, C. (2015). Particle-based imaging techniques. In Adams, F., & Barbante, C. (Eds.), *Chemical Imaging Analysis* (1st ed.) (315 – 337). Amsterdam : Elsevier.

Agrawal, A., & Rahman, B. M. A. (2013). *Finite Element Modeling Methods for Photonics*. (1st ed.). Norwood: Artech.

Aharonov, Y., & Bohm, D. (1959). Significance of electromagnetic potentials in the quantum theory. *Physical Review*, *115*, 485 – 491.

Al-Hayek, I., & Sandouqa, A. S. (2015). Energy and binding energy of donor impurity in quantum dot with gaussian confinement. *Superlattices and Microstructures*, *85*, 216 – 225.

Anisimov, S. I., & Khokhlov, V. A. (2001). *Instabilities in laser-matter interaction*. (1st ed.). New York: Springer.

Ashkin, A., Boyd, G. D., Dziedzic, J. M., Smith, R. G., Ballman, A. A., Levinstein,

J. J., et al. (1966). Optically-induced refractive index inhomogeneities in $LiNbO_3$ and $LiTaO_3$. *Applied Physics Letters*, *9*, 72 – 74.

Baghramyan, H. M., Barseghyan, M. G., & Laroze, D. (2017). Molecular spectrum of laterally coupled quantum rings under intense terahertz radiation. *Scientific Reports*, *7*, 10485.

Baghramyan, H. M., Barseghyan, M. G., Laroze, D., & Kirakosyan, A. A. (2016). Influence of lateral electric field on intraband optical absorption in concentric double quantum rings. *Physica E*, *77*, 81 – 89.

Banyai, L., & Koch, S. W. (1993). *Semiconductor quantum dots*. (1st ed.). Singapore: World Scientific.

Barseghyan, M., Manaselyan, A. K., Laroze, D., & Kirakosyan, A. A. (2016). Impurity-modulated aharonov-bohm oscillations and intraband optical absorption in quantum dot-ring nanostructures. *Physica E*, *81*, 31 – 36.

Barseghyan, M. G. (2015). Electronic states of coupled quantum dot-ring structure under lateral electric field with and without a hydrogenic donor impurity. *Physica E*, *69*, 219 – 223.

Barseghyan, M. G. (2016a). Donor impurity-related intraband optical absorption in a single quantum ring: hydrostatic pressure and intense laser field effects. *The European Physical Journal B*, *131*, 361.

Barseghyan, M. G. (2016b). Energy levels and far-infrared optical absorption of impurity doped semiconductor nanorings: intense laser and electric fields effects. *Chemical Physics*, *479*, 1 – 4.

Barseghyan, M. G., Kirakosyan, A. A., & Laroze, D. (2017). Laser driven intraband optical transitions in two-dimensional quantum dots and quantum rings. *Optics Communications*, *383*, 571 – 576.

Baskoutas, S., Paspalakis, E., & Terzis, A. F. (2007). Electronic structure and nonlinear optical rectification in a quantum dot: effects of impurities and external electric field. *Journal of Physics Condensed Matter*, *19*, 395024.

Bass, M., Franken, P. A., & Weinreich, G. (1692). Optical rectification. *Physics Review Letters*, *9*, 446 – 449.

Bastard, G. (1981). Hydrogenic impurity states in a quantum well: A simple model. *Physical Review B*, *24*, 4714 – 4722.

Batani, D., Joachain, C. J., Martellucci, S., & Chester, A. N. (Eds.) (2001). *Atoms, solids, and plasmas in super-intense laser fields*. (1st ed.). New York: Springer.

Bednarek, S., Szafran, B., Lis, K., & Adamowski, J. (2003). Modeling of electronic properties of electrostatic quantum dots. *Physical Review B*, *68*, 155333.

Bejan, D. (2016a). Effects of the structure asymmetry on optical responses in gaas double quantum dots under intense laser and electric fields. *Modern Physics Letters B*, *30*, 1650361.

Bejan, D. (2016b). Impurity-related nonlinear optical rectification in double quantum dot under electric field. *Physics Letters A*, *380*, 3836 – 3842.

Bejan, D. (2017a). Donor impurity-related nonlinear optical rectification in a two-dimensional quantum ring under magnetic field. *Physical Letters A*, *381*, 3307 – 3313.

Bejan, D. (2017b). Effects of electric field and structure on the electromagnetically induced transparency in double quantum dot. *Optical Materials*, *67*, 145 – 154.

Bejan, D., & Niculescu, E. C. (2016a). Electronic and optical properties of asymmetric gaas double quantum dots in intense laser fields. *Philosophical Magazine*, *96*, 1131 – 1149.

Bejan, D., & Niculescu, E. C. (2016b). Intense laser effects on the optical properties of asymmetric gaas double quantum dots under applied electric field. *The European Physical Journal B*, *89*, 138.

Bejan, D., Stan, C., & Niculescu, E. C. (2018). Optical properties of an elliptic quantum ring: eccentricity and electric field effects. *Optical Materials*, *78*, 207 – 219.

Bera, A., Ganguly, J., Saha, S., & Ghosh, M. (2016). Interplay between noise and position-dependent dielectric screening function in modulating nonlinear optical properties of impurity doped quantum dots. *Optik*, *127*, 6771 – 6778.

Bhatti, S., Sbiaa, R., Hirohata, A., Ohno, H., Fukami, S., & Piramanayagam, S. N. (2017). Spintronics based random access memory: a review. *Materials Today*, *20*, 530 – 548.

Bimberg, D., Grundmann, M., & Ledentsov, N. N. (1999). *Quantum dot heterostructures*. (1st ed.). Chichester: John Wiley & Son.

Boda, A. (2019). Magnetic moment and susceptibility of an impurity in a parabolic quantum dot. *Journal of Magnetism and Magnetic Materials*, *483*, 83 – 88.

Borovitskaya, E., & Shur, M. S. (2002). *Quantum dots*. (1st ed.). Singapore: World Scientific.

Bose, C. (1998). Binding energy of impurity states in spherical quantum dots with parabolic confinement. *Journal of Applied Physics*, *83*, 3089 – 3091.

Boyd, R. W. (2008). *Nonlinear optics*. (3rd ed.). New York: Academic Press.

Brandi, H. S., Latge, A., & Oliveira, L. E. (2001). Dressed-band approach to laser-field effects in semiconductors and quantum-confined heterostructures. *Physical Review B*, *64*, 035323.

Brandi, H. S., Latge, A., & Oliveira, L. E. (2004). Laser effects on donor states in low-dimensional semiconductor heterostructures. *Physical Review B*, *70*, 153303.

Brenner, S. C., & Scott, L. R. (2007). *The mathematical theory of finite element methods*. (3rd ed.). New York: Springer.

Brum, J. A., Bastard, G., & Guillemot, C. (1984). Screened coulombic impurity bound states in semiconductor quantum wells. *Physical Review B*, *30*, 905 – 908.

Burileanu, L. M. (2014). Photoionization cross-section of donor impurity in spherical quantum dots under electric and intense laser fields. *Journal of Luminescence*, *145*, 684 – 689.

Cakir, B., Yakar, Y., & Ozmen, A. (2017). Linear and nonlinear absorption coefficients of spherical quantum dot inside external magnetic field. *Physica B*, *510*, 86 – 91.

Chakraborty, T. (1999). *Quantum dots*. (1st ed.). Amsterdam: North-Holland.

Chakraborty, T., Manaselyan, A., Barseghyan, M., & Laroze, D. (2018). Controllable continuous evolution of electronic states in a single quantum ring. *Physical Review B*, *97*, 041304.

Chakraborty, T., & Pietiläinen, P. (1994). Electron-electron interaction and the persistent current in a quantum ring. *Physical Review B*, *50*, 8460 – 8468.

Charrour, R., Bouhassoune, M., Fliyou, M., Bria, D., & Nougaoui, A. (2000). Magnetopolaron effect in cdte cylindrical quantum dot. *Journal of Applied Physics*, *88*, 3514 – 3521.

Chen, S. (2011). Hydrogenic impurity bound polaron in a parabolic quantumdot with arbitrary electron-phonon coupling strength. *Physica B*, *406*, 2033 – 2037.

Chen, T., Xie, W., & Liang, S. (2013). Optical and electronic properties of a two-dimensional quantumdot with an impurity. *Journal of Luminescence*, *139*, 64 – 68.

Chowdhury, A. D., Ganganboina, A. B., Tsai, Y., Chiu, H., & Doong, R. (2018). Multifunctional GQDs-Concanavalin A@Fe_3O_4 nanocomposites for cancer cells detection and targeted drug delivery. *Analytica Chimica Acta*, *1027*, 109 – 120.

Cibert, J., Petroff, P. M., Dolan, G. J., Pearton, S. J., Gossard, A. C., & English, J. H. (1986). Optically detected carrier confinement to one and zero dimension in gaas quantum well wires and boxes. *Applied Physics Letters*, *49*, 1275 – 1277.

Ciftja, O. (2013). Understanding electronic systems in semiconductor quantum dots. *Physica Scripta*, *88*, 058302.

Colton, D., & Kress, R. (2010). *Inverse Acoustic and Electromagnetic Scattering Theory*. (3rd ed.). Berlin: Springer.

D'Amico, I. (2006). Quantum dot-based quantum buses for quantum computer hardware architecture. *Microelectronics Journal*, *37*, 1440 – 1441.

Damiri, H., & Askari, H. R. (2017). The effect of impurities on linear and nonlinear absorption coefficient and refractive index of the spherical quantum dot four-level m-model the phenomenon of electromagnetically induced transparency. *Superlattices and Microstructures*, *101*, 271 – 284.

Damodaran, V., & Ghosh, K. (2016). Choice of quantum dot materials for fabricating memory devices with longer storage and faster writing of information. *Superlattices and Microstructures*, *100*, 1042 – 1056.

Datta, N. K., & Ghosh, M. (2011). Impurity modulated excitation profile of doped quantum dot subject to oscillatory magnetic field. *Materials Chemistry and Physics*, *126*, 693 – 699.

Datta, N. K., Ghosh, S., & Ghosh, M. (2010). Excitations in doped quantum dot driven by discontinuously and randomly reversing electric field: Influence of impurity. *Chemical Physics*, *378*, 66 – 72.

Deb, N. C. (1994). Fourier transform technique to calculate matrix elements in the basis of hydrogenic wave functions. *Physica Scripta*, *49*, 550 – 552.

Dehyar, A., Rezaei, G., & Zamani, A. (2016). Electronic structure of a spherical quantum dot: effects of the kratzer potential, hydrogenic impurity, external electric and magnetic fields. *Physica E*, *84*, 175 – 181.

Dimitrakis, P., Normand, P., Ioannou-Sougleridis, V., Bonafos, C., Schamm-Chardon, S., BenAssayag, G., et al. (2013). Quantumdots for memory applications. *Physica Status Solidi A*, *210*, 1490 – 1504.

Dingle, R., Wiegmann, W., & Henry, C. H. (1974). Quantum states of confined carriers in very thin $Al_xGa_{1-x}As$-gaas-$Al_xGa_{1-x}As$. *Physical Review Letters*, *33*, 827 – 830.

Duque, C. A., Mora-Ramos, M. E., & Correa, J. D. (2015). Donor-impurity-related second and third harmonic generation and optical absorption in gaas-(ga,al)as 3d coupled quantum dot-rings under applied electric field. *Superlattices Microstructures*, *87*, 25 – 31.

Duque, C. M., Mora-Ramos, M. E., & Duque, C. (2012a). Quantum disc plus inverse square potential. an analytical model for two-dimensional quantum rings: study of nonlinear optical properties. *Annalen der Physik*, *524*, 327 – 337.

Duque, C. M., Mora-Ramos, M. E., & Duque, C. A. (2012b). On-center donor impurity-related nonlinear corrections to optical absorption and refractive index in a two-dimensional quantum ring. *Optics Communications*, *285*, 5456 – 5461.

Duque, C. M., Mora-Ramos, M. E., & Duque, C. A. (2013). Properties of the second and third harmonics generation in a quantum disc with inverse square potential. a modeling for nonlinear optical responses of a quantum ring. *Journal of Luminescence*, *138*, 53 – 60.

Durak, S. (2015). *Laser field effect on the nonlinear optical properties of quantum dots*. Master's Thesis, Dokuz Eylul University, İzmir.

Edvinsson, T. (2018). Asymptotic iteration method solution of the energy spectrum of two-dimensional screened donor in a magnetic field. *Royal Society Open Science*, *5*, 180387.

Ekimov, A. I., & Onushchenko, A. A. (1981). Quantum siz effect in three-dimensional microscopic semiconductor crystals. *Journal of Experimental and Theoretical Physics Letters*, *34*, 345 – 348.

Enders, B. G., Lima, F. M. S., Nunes, O. A. C., Fonseca, A. L. A., Agrello, D. A., Qu, F., Silva, E. F. D., & Freire, V. N. (2004). Electronic properties of a quasi-two-dimensional electron gas in semiconductor quantum wells under intense laser fields. *Physical Review B*, *70*, 035307.

Ermolaev, A. M., & Rashba, G. I. (2008). Impurity states of electrons in quantum dots in external magnetic fields. *The European Physical Journal B*, *66*, 223 – 226.

Eseanu, N. (2011). 14- intersubband and interband absorptions in near-surface quantum wells under intense laser field. In Adams, F., & Barbante, C. (Eds.), *Optoelectronics: Devices and Applications*, pp. (315 – 337), IntechOpen.

Fanyao, Q., Fonseca, A. L. A., & Nunes, O. A. C. (1996). Hydrogenic impurities in a quantum well wire in intense, high-frequency laser fields. *Physical Review B*, *197*, 349 – 357.

Ferreyra, J. M., Bosshard, P., & Proetto, C. R. (1997). Strong-confinement approach for impurities in parabolic quantum dots. *Physical Review B*, *55*, 13682 – 13688.

Fert, A. (2008). Nobel lecture: Origin, development, and future of spintronics. *Reviews of Modern Physics*, *80*, 1517 – 1530.

Fomin, V. M. (Ed.) (2018). *Physics of quantum rings*. (2nd ed.). Cham: Springer.

Franken, P. A., Hill, C. W., & Weinreich, G. (1961). Generation of optical harmonics. *Physics Review Letters*, *7*, 118 – 120.

Fuhrer, A., Lücher, S., Ihn, T., Heinzel, T., Ensslin, K., Wegscheider, W., & Bichler, M. (2001). Energy spectra of quantum rings. *Nature*, *413*, 822 – 825.

G. Liu, H. H. L. L., K. Guo (2012). Linear and nonlinear optical properties in a disk-shaped quantum dot with a parabolic potential plus a hyperbolic potential in a static magnetic field. *Physica B*, *407*, 3676 – 3682.

Gambhir, M., Kumar, M., Jha, P. K., & Mohan, M. (2013). Linear and nonlinear optical absorption coefficients and refractive index changes associated with intersubband transitions in a quantum disk with flat cylindrical geometry. *Journal of Luminescence*, *143*, 361 – 367.

Ganguly, J., & Ghosh, M. (2016). Modulating optical second harmonic generation of impurity-doped quantum dots in presence of gaussian white noise. *Physica Status Solidi B*, *253*, 1093 – 1103.

Ganguly, J., Saha, S., Bera, A., & Ghosh, M. (2017). Exploring electro-optic effect and third-order nonlinear optical susceptibility of impurity doped quantum dots: Interplay between hydrostatic pressure, temperature and noise. *Optics Communications*, *387*, 166 – 173.

Gavrila, M. (1992). *Atoms in intense laser fields*. (0th ed.). Londom: Academic Press, Inc.

Ghosh, A., Arif, S. M., Bera, A., & Ghosh, M. (2020). Profiles of static quadrupole polarizability of impurity-doped quantum dots driven by gaussian white noise. *Physica Status Solidi B*, *257*, 1900766.

Ghosh, A., & Frota, H. O. (2013). Spintronics in a magnetic quantum dot. *Journal of Applied Physics*, *114*, 073707.

Gonzalez-Santander, C., Apostolova, T., & Dominguez-Adame, F. (2013). Binding energy of hydrogenic impurities in quantum dots under intense laser radiation. *Journal of Physics : Condensed Matter*, *25*, 335802.

Gonzalez-Santander, C., Dominguez-Adame, F., & Romer, R. A. (2011). Excitonic aharonov-bohm effect in a two-dimensional quantum ring. *Physics Review B*, *84*, 235103.

Gradsteyn, I. S., & Ryzhik, I. M. (2007). *Table of integrals, series, and products*. (7th ed.). California: Academic Press.

Halonen, V., Hyvönen, P., Pietiläinen, P., & Chakraborty, T. (1996a). Effects of scattering centers on the energy spectrum of a quantum dot. *Physical Review B*, *53*, 6971 – 6974.

Halonen, V., Hyvönen, P., Pietiläinen, P., & Chakraborty, T. (1996b). Optical-absorption spectra of quantum dots and rings with a repulsive scattering centre. *Europhysics Letters*, *33*, 377 – 382.

Hanna, J. R., & Rowland, J. H. (2008). *Fourier series, transforms, and boundary value problems*. (2nd ed.). New York: Dover Publications.

Harrison, P. (2005). *Quantum wells, wires and dots*. (2nd ed.). England: Wiley.

Hecht, E. (2001). *Optics*. (4th ed.). San Francisco: Addison-Wesley.

Hennebergers, W. C. (1968). Perturbation method for atoms in intense light beams. *Physical Review Letters*, *21*, 838 – 841.

Hirohata, A., Yamada, K., Nakatani, Y., Prejbeanu, I., Dieny, B., Pirroe, P., et al. (2020). Review on spintronics: Principles and device applications. *Journal of Magnetism and Magnetic Materials*, *509*, 166711.

Holovatsky, V. A., Voitsekhivska, O. M., & Yakhnevych, M. Y. (2017). Effect of magnetic field on an electronic structure and intraband quantum transitions in multishell quantum dots. *Physica E*, *93*, 295 – 300.

Holtz, P. O., & Zhao, Q. X. (2004). *Impurities Confined in Quantum Structures*. (1st ed.). Berlin: Springer.

Hosseinpour, P., Soltani-Vala, A., & Barvestani, J. (2016). Effect of impurity on the absorption of a parabolic quantum dot with including rashba spin-orbit interaction. *Physica E*, *80*, 48 – 52.

Huang, J. (2013). Effect of the charges of impurity on the refractive index changes in parabolic quantum dot. *Physica B*, *409*, 16 – 20.

Hutton, D. V. (2003). *Fundamentals of finite element analysis*. (1st ed.). New York: McGraw-Hill.

Imamoglu, A. (2003). Are quantum dots useful for quantum computation? *Physica E*, *16*, 47 – 50.

Ishikawa, H. (1999). Chapter 7 - applications of quantum dot to optical devices. In Sugawara, M. (Ed.), *Self-Assembled InGaAs/GaAs Quantum Dots*, Semiconductors and Semimetals, pp. (287 – 323), Elsevier.

Jacak, L., Hawrylak, P., & Wójs, A. (1998). *Quantum dots*. (1st ed.). Berlin: Springer.

Jin, M., Xie, W., & Chen, T. (2013). Photoionization cross section in a two-dimensional quantum ring with a donor impurity. *Superlattices and Microstructures*, *62*, 59 – 67.

Joachain, C. J. (2014). High-intensity laser-atom interactions. *Europhysics Letters*, *108*, 44001.

Kaiser, W., & Garrett, C. G. B. (1961). Two-photon excitation in caf_2:Eu^{2+}. *Physics Review Letters*, *7*, 229 – 232.

Kajdos, A., & Stemmer, S. (2015). 3 - hybrid molecular beam epitaxy for the growth of complex oxide materials. In Koster, G., Huijben, M., & Rijnders, G. (Eds.), *Epitaxial Growth of Complex Metal Oxides*, Woodhead Publishing Series in Electronic and Optical Materials, pp. (47 – 68), Woodhead Publishing.

Kandemir, B. S., & Cetin, A. (2002). Ground- and first-excited state energies of impurity magnetopolaron in an anisotropic quantum dot. *Physical Review B*, *65*, 054303.

Karabulut, I. (2008). *Asimetrik Kuantum kuyu yapılarının lineer olmayan optik özelliklerinn incelenmesi*. Ph.D. Thesis, Selçuk University, Konya.

Karabulut, I., & Baskoutas, S. (2008). Linear and nonlinear optical absorption coefficients and refractive index changes in spherical quantum dots: Effects of impurities, electric field, size, and optical intensity. *Journal of Applied Physics*, *103*, 073512.

Kasapoglu, E., Duque, C., Sakiroglu, S., Sari, H., & Sokmen, I. (2011). The effects of the intense laser field on donor impurities in a cylindrical $Ga_xIn_{1-x}N_yAs_{1-y}/GaAs$ quantum dot under the electric field. *Physica E*, *43*, 1427 – 1432.

Kasapoglu, E., Duque, C., Sakiroglu, S., Sari, H., & Sokmen, I. (2015). The effects of the intense laser field on the nonlinear optical properties of a cylindrical $Ga_{1-x}Al_xAs/GaAs$ quantum dot under applied electric field. *Physica B*, *474*, 15 – 20.

Khordad, K. (2017). Third-harmonic generation in a double ring-shaped quantum dot under electron-phonon interaction. *Optics Communications*, *391*, 121 – 127.

Khordad, R., & Bahramiyan, H. (2014). The second and third-harmonic generation of modified gaussian quantum dots under influence of polaron effects. *Superlattices and Microstructures*, *76*, 163 – 173.

Kilic, D. G., Sakiroglu, S., Kasapoglu, E., Sari, H., & Sokmen, I. (2020). Impurity-modulated optical response of a disc-shaped quantum dot subjected to laser radiation. *Photonics and Nanostructures - Fundamentals and Applications*, *38*, 100748.

Kilic, D. G., Sakiroglu, S., & Sokmen, I. (2018). Impurity-related optical properties of a laser-driven quantum dot. *Physica E*, *102*, 50 – 57.

Kilic, D. G., Sakiroglu, S., Ungan, F., Yesilgul, U., Kasapoglu, E., Sari, H., & Sokmen, I. (2017). Optical response in a laser-driven quantum pseudodot system. *Physica B*, *509*, 10 – 15.

Kilic, D. G., Sakiroglu, S., Ungan, F., Yesilgul, U., Kasapoglu, E., Sari, H., & Sokmen, I. (2019). Tailoring the optical properties of quantum ring irradiated by thz laser. *Philosophical Magazine*, *99*, 3116 – 3132.

Knoss, R. W. (2009). *Quantum dots: research, technology and applications*. (3rd ed.). New York: Nova Science.

Kouwenhoven, L. P., Austing, D. G., & Tarucha, S. (2001). Few-electron quantum dots. *Reports on Progress in Physics*, *64*, 701 – 736.

Kshevetsky, S., & Shapilov, A. (2017). Regularization of coulomb potential for calculating electron density in quantum mechanical system. *TASK Quarterly*, *21*, 177 – 184.

Kwon, Y. W., & Bang, H. (1997). *The finite element method using MATLAB*. (2nd ed.). United States of America: CRC Press.

Laroze, D., Barseghyan, M., Radu, A., & Kirakosyan, A. A. (2016). Laser driven impurity states in two-dimensional quantum dots and quantum rings. *Physica B*, *501*, 1 – 4.

Li, B., Guo, K., Liu, Z., & Zheng, Y. (2008). Nonlinear optical rectification in parabolic quantum dots in the presence of electric and magnetic fields. *Physics Letters A*, *372*, 1337 – 1340.

Li, K., Guo, K., & Liang, L. (2016). Effect of the shape of quantum dots on the refractive index changes. *Physica B*, *502*, 146 – 152.

Li, K., Guo, K., & Liang, L. (2017). Effect of the shape of quantum dots on the third-harmonic generations. *Superlattices and Microstructures*, *102*, 300 – 306.

Li, N., Guo, K. X., Shao, S., & Liu, G. H. (2012). Polaron effects on the optical absorption coefficients and refractive index changes in a two-dimensional quantum pseudodot system. *Optical Materials*, *34*, 1459 – 1463.

Liang, S., Xie, W., Li, X., & Shen, H. (2011). Photoionization and binding energy of a donor impurity in a quantum dot under an electric field: Effects of the hydrostatic pressure and temperature. *Superlattices and Microstructures*, *49*, 623 – 631.

Liao, G., & Xie, W. (2015). Linear and nonlinear susceptibilities of a d^- system in a semiconductor quantum ring. *Superlattices and Microstructures*, *82*, 82 – 89.

Lima, F. M. S., Amato, M. A., Nunes, O. A. C., Fonseca, A. L. A., & da Silva Jr, E. F. (2009a). Increase of the positronium lifetime under high-frequency, intense laser fields. *Journal of Physics B: Atomic Molecular and Optical Physics*, *42*, 055601.

Lima, F. M. S., Amato, M. A., Nunes, O. A. C., Fonseca, A. L. A., & Enders, B. G. (2009b). Unexpected transition from single to double quantum well potential induced by intense laser fields in a semiconductor quantum well. *Journal of Applied Physics*, *105*, 123111.

Lima, F. M. S., Nunes, O. A. C., Amato, M. A., Fonseca, A. L. A., & da Silva Jr, E. F. (2008). Dichotomy of the exciton wave function in semiconductors under intense laser fields. *Journal of Applied Physics*, *103*, 113112.

Lin, S., Xie, X., Patel, M. R., Yang, Y., Li, Z., Cao, F., et al. (2007). Quantum dot imaging for embryonic stem cells. *BMC Biotechnology*, *7*(67), 1 – 10.

Liu, G., Guo, K., & Wang, C. (2012). Linear and nonlinear intersubband optical absorption in a disk-shaped quantum dot with a parabolic potential plus an inverse squared potential in a static magnetic field. *Physica B*, *407*, 2334 – 2339.

Loss, D., & DiVincenzo, D. P. (1998). Quantum computation with quantum dots. *Physical Review A*, *57*, 120 – 126.

Lu, L., & Xie, W. (2011). Impurity and exciton effects on the nonlinear optical properties of a disc-like quantum dot under a magnetic field. *Superlattices and Microstructures*, *50*, 40 – 49.

Lu, L., Xie, W., Hassanabadi, H., & Zhong, Q. (2011). The effect of intense laser field on the electronic raman scattering of shallow donor impurities in quantum dots. *Superlattices and Microstructures*, *50*, 501 – 510.

Madhav, A. V., & Chakraborty, T. (1994). Electronic properties of anisotropic quantum dots in a magnetic field. *Physical Review B*, *49*, 8163 – 8168.

Maikhuri, D., Purohit, S. P., & Mathur, K. C. (2015). Third harmonic and sum-frequency generation in zno quantum dots. *Superlattices Microstructures*, *85*, 206 – 215.

Martinez-Orozco, J., Rojas-Briseno, J. G., Rodriguez-Magdaleno, K. A., Rodriguez-Vargas, I., Mora-Ramos, M. E., Restrepo, R. L., et al. (2017). Effect of the magnetic field on the nonlinear optical rectification and second and third harmonic generation in double δ-doped gaas quantum wells,. *Physica B*, *525*, 30 – 35.

Mikhail, I. F. I., & Shafee, A. M. (2017). Optical absorption in a disk-shaped quantum dot in the presence of an impurity. *Physica B*, *507*, 142 – 146.

Mittleman, M. H. (1982). *Theory of Laser-Atom Interactions*. (1st ed.). New York: Plenum Press.

Mizutani, U. (2001). *Introduction to the Electron Theory of Metals*. (1st ed.). Cambridge: Cambridge University Press.

Mohammadi, S. A., Khordad, R., & Rezaei, G. (2016). Optical properties of a semispherical quantum dot placed at the center of a cubic quantum box: Optical rectification, second and third-harmonic generations. *Physica E*, *76*, 203 – 208.

Mora-Ramos, M. E., Duque, C. A., Kasapoglu, E., Sari, H., & Sokmen, I. (2012a). Linear and nonlinear optical properties in a semiconductor quantum well under intense laser radiation: Effects of applied electromagnetic fields. *Journal of Luminescence*, *132*, 901 – 903.

Mora-Ramos, M. E., Duque, C. A., Kasapoglu, E., Sari, H., & Sokmen, I. (2012b). Study of direct and indirect exciton states in $GaAs$-$Ga_{1-x}Al_xAs$ quantum dots under the effects of intense laser field and applied electric field. *The European Physical Jorunal B*, *85*, 312.

Mukhopadhyay, S., & Chatterjee, A. (1998). Polaronic correction to the first excited electronic energy level in semiconductor quantum dots with parabolic confinement. *Physics Letters A*, *240*, 100 – 104.

Mulser, P., & Bauer, D. (2010). *High power laser-matter interaction*. (1st ed.). Berlin: Springer.

Niculescu, E. C. (2017). Electric field effect on the impurity-related electromagnetically induced transparency in a quantum disk under non-resonant, intense laser radiation. *Chemical Physics*, *487*, 16 – 22.

Niculescu, E. C., & Bejan, D. (2017). Off-centre impurity-related nonlinear optical absorption, second and third harmonic generation in a two-dimensional quantum ring under magnetic field. *Philosophical Magazine*, *97*, 2089 – 2107.

Niculescu, E. C., Stan, C., Tiriba, G., & Trusca, C. (2017). Magnetic field control of absorption coefficient and group indexin an impurity doped quantum disc. *European Physical Journal B*, *90*, 100.

Nifontova, G., Ramos-Gomes, F., Baryshnikova, M., Alves, F., Nabiev, I., & Sukhanova, A. (2019). Cancer cell targeting with functionalized quantum dot-encoded polyelectrolyte microcapsules. *Frontiers in Chemistry*, *7*, 1 – 34.

Nowozin, T., Bimberg, D., Daqrouq, K., Ajour, M. N., & Awedh, M. (2013). Materials for future quantum dot-based memories. *Journal of Nanomaterials*, *2013*(215613), 1 – 6.

Pan, J., Liu, L., & Liu, M. (2011). Hydrogenic-donor impurity states in gaas/al$_x$ga$_{1-x}$as quantum dots in the presence of an electric field. *Chinese Physics Letters*, *28*, 086201.

Pask, J. E., Klein, B. M., Sterne, P. A., & Fong, C. Y. (2001). Finite-element methods in electronic-structure theory. *Computer Physics Communications*, *135*, 1–34.

Paspalakis, E., Boviatsis, J., & Baskoutas, S. (2013). Effects of probe field intensity in nonlinear optical processes in asymmetric semiconductor quantum dots. *Journal of Applied Physics*, *114*, 153107.

Peng, C., & Li, Y. (2010). Application of quantum dots-based biotechnology in cancer diagnosis: Current status and future perspectives. *Journal of Nanomaterials*, *2010*(676839), 1 – 11.

Ping, E. X., & Jiang, H. X. (1993). Effect of charge-carrier screening on the exciton binding energy in GaAs/$Al_xGa_{1-x}As$ quantum wells. *Physical Review B*, *47*, 2101 – 2106.

Ping, E. X., & Jiang, H. X. (2002). Energy spectrum of a two-dimensional screened donor in a constant magnetic field of arbitrary strength. *Physica B*, *315*, 289 – 296.

Pont, M. (1989). Atomic distortion and ac-stark shifts of h under extreme radiation conditions. *Physical Review A*, *40*, 5659 – 5672.

Pont, M., & Gavrila, M. (1990). Stabilization of atomic hydrogen in superintense, high-frequency laser fields of circular polarization. *Physical Review Letters*, *65*, 2362 – 2365.

Pont, M., Offerhaus, M. J., & Gavrila, M. (1988a). Stabilization of atomic hydrogen in superintense, high-frequency laser fields of circular polarization. *Z. Phys. D- Atoms, Molecules and Clusters*, *9*, 297 – 306.

Pont, M., Walet, N. R., Gavrila, M., & McCurdy, C. W. (1988b). Dichotomy of the hydrogen atom in superintense, high-frequency laser fields. *Physical Review Letters*, *61*, 939 – 942.

Porras-Montenegro, N., & Perez-Merchancano, S. T. (1992). Hydrogenic impurities in gaas-(ga, al)as quantum dots. *Physical Review B*, *46*, 9780 – 9783.

Poszwa, A. (2014). Dirac electron in the two-dimensional debye-yukawa potential. *Physica Scripta*, *89*, 065401.

Powers, P. E. (2013). *Field guide to nonlinear optics*. (1st ed.). Washington: Spie Press.

Prasad, V., & Silotia, P. (2011). Effect of laser radiation on optical properties of disk shaped quantum dot in magnetic fields. *Physics Letters A*, *375*, 3910 – 3915.

Radu, A., Kirakosyan, A. A., Laroze, D., Baghramyan, H. M., & Barseghyan, M. G. (2014). Electronic and intraband optical properties of single quantum rings under intense laser field radiation. *Journal Of Applied Physics*, *116*, 093101.

Ram-Mohan, L. R. (2002). *Finite element and boundary element applications in quantum mechanics*. (1st ed.). Oxford: Oxford University Press.

Räsänen, E., & Aichinger, M. (2009). Large quantum rings in the $\nu > 1$ quantum hall regime. *Journal of Physics Condensed Matter*, *21*, 025301.

Räsänen, E., Castro, A., Werschnik, J., Rubio, A., & Gross, E. K. U. (2007). Optimal control of quantum rings by terahertz laser pulses. *Physical Review Letters*, *98*, 157404.

Räsänen, E., Könemann, J., Haug, R. J., Puska, M. J., & Nieminen, R. M. (2004). Impurity effects in quantum dots: Toward quantitative modeling. *Physical Review B*, *70*, 115308.

Reddy, J. N. (1993). *An introduction to the finite element method*. (2nd ed.). Singapore: McGraw-Hill.

Reed, M. A., Bate, R. T., Bradshaw, K., Duncan, W. M., Frensley, W. R., Lee, J. W., et al. (1986). Spatial quantization in gaas-algaas multiple quantum dots. *Journal of Vacuum Science & Technology B: Microelectronics Processing and Phenomena*, *4*, 358 – 360.

Reed, M. A., Randall, J. N., Aggarwal, R. J., Matyi, R. J., Moore, T. M., & Wetsel, A. E. (1988). Observation of discrete electronic states in a zero-dimensional semiconductor nanostructure. *Physical Review Letters*, *60*, 535 – 537.

Rezaei, G., Vaseghi, B., & Ebrahimi, J. (2011). External electric field effects on the electronic and hydrogenic impurity states in ellipsoidal and semi-ellipsoidal quantum dots. *Superlattices and Microstructures*, *49*, 591 – 598.

Rezaei, G., Vaseghi, B., Taghizadeha, F., Vahdani, M. R. K., & Karimi, M. J. (2010). Intersubband optical absorption coefficient changes and refractive index changes in a two-dimensional quantum pseudodot system. *Superlattices and Microstructures*, *48*, 450 – 457.

Rezaei, G., & Vaseghi, Z. M. B. (2010). Nonlinear optical properties of a two-dimensional elliptic quantum dot. *Physica E*, *42*, 1477 – 141.

Sadeghi, E. (2009). Impurity binding energy of excited states in spherical quantum dot. *Physica E*, *41*, 1319 – 1322.

Safarpour, G., Zamani, A., Izadi, M. A., & Ganjipour, H. (2014). Laser radiation effect on the optical properties of a spherical quantum dot confined in a cylindrical nanowire. *Journal of Luminescence*, *147*, 295 – 303.

Saha, S., & Ghosh, M. (2015). Polarizabilities of impurity doped quantum dots under pulsed field: Role of additive white noise. *Open Journal of Microphysics*, *5*, 1 – 10.

Saha, S., & Ghosh, M. (2016). Tuning third harmonic generation of impurity doped quantum dots in the presence of gaussian white noise. *Journal of Physics and Chemistry of Solids*, *90*, 69 – 79.

Sakiroglu, S., Kilic, D. G., Yesilgul, U., Ungan, F., Kasapoglu, E., Sari, H., & Sokmen, I. (2017). Intense laser field effects on the third-harmonic generation in a quantum pseudodot system. *Physica B*, *521*, 215 – 220.

Sakiroglu, S., Kilic, D. G., Yesilgul, U., Ungan, F., Kasapoglu, E., Sari, H., & Sokmen, I. (2018). Third-harmonic generation of a laser-driven quantum dot with impurity. *Physica B*, *539*, 101 – 105.

Saleh, B. E. A., & Teich, M. C. (1991). *Fundamentals of photonics*. (1st ed.). Canada: John Wiley & Sons.

Salehani, H. K., Shakouri, K., & Esmaeilzadeh, M. (2015). Effect of donor impurity dislocation in elliptical quantum rings. *Physica B*, *459*, 36 – 40.

Sari, H., Kasapoglu, E., Sakiroglu, S., Sokmen, I., & Duque, C. A. (2020). Impurity-related optical response in a 2d and 3d quantum dot with gaussian confinement under intense laser field. *Philosophical Magazine*, *100*, 619 – 641.

Sari, H., Ungan, F., Sakiroglu, S., Yesilgul, U., & Sokmen, I. (2018). Impurity-related optical response in cylindrical quantum dots with a δ-doped axial potential under an intense laser field. *Journal of Physics and Chemistry of Solids*, *120*, 279 – 286.

Sarkar, S., Ghosh, A. P., Mandal, A., & Ghosh, M. (2016). Modulating nonlinear optical properties of impurity doped quantum dots via the interplay between anisotropy and gaussian white noise. *Superlattices and Microstructures*, *90*, 297 – 307.

Shao, S., Guo, K., Zhang, Z., Li, N., & Peng, C. (2010). Studies on the third-harmonic generations in cylindrical quantum dots with an applied electric field. *Superlattices and Microstructures*, *48*, 541 – 549.

Shao, S., Guo, K., Zhang, Z., Li, N., & Peng, C. (2011). Third-harmonic generation in cylindrical quantum dots in a static magnetic field. *Solid State Communications*, *151*, 289 – 292.

Sheng, W., Yun, K., & Xianli, L. (2016). Donor impurity-related optical absorption coefficients and refractive index changes in a rectangular gaas quantum dot in the presence of electric field. *Journal of Semiconductors*, *37*, 112001.

Shi, D., Guo, Z., & Bedford, N. (2015). 8 - superconducting nanomaterials. In Shi, D., Guo, Z., & Bedford, N. (Eds.), *Nanomaterials and Devices*, Micro and Nano Technologies, pp. (191 – 213), William Andrew Publishing.

Shinoj, V. K. (2016). *Vapour Growth and Epitaxial Growth: Epitaxial Growth Techniques*. Retrieved November 29, 2020, from https://shinojvk.uccollege.edu.in/wp-content/uploads/sites/196/2016/11/Epitaxial-growth2-1.pdf.

Shojaei, S., & Vala, A. S. (2015). Nonlinear optical rectification of hydrogenic impurity in a disk-like parabolic quantum dot: the role of applied magnetic field. *Physica E*, *70*, 108 – 112.

Solaimani, M. (2020). Binding energy and diamagnetic susceptibility of donor impurities in quantum dots with different geometries and potentials. *Materials Science & Engineering B*, *262*, 114694.

Soltani-Vala, A., & Barvestani, J. (2017). Effects of anisotropy on the optical rectification of a disk-like quantum dot with donor impurity in external electric and magnetic fields. *Physica B*, *518*, 88 – 93.

Soylu, A., & Boztosun, I. (2008). Asymptotic iteration method solution of the energy spectrum of two-dimensional screened donor in a magnetic field. *Physica E*, *40*, 443 – 448.

Spandonide, A., Tiriba, G., & Niculescu, E. C. (2016). Simultaneous effects of intense laser and static electric fields on the oscillator strength in an impurity doped disc-like quantum dot. *UPB Scientific Bulletin, Series A: Applied Mathematics and Physics*, *78*, 307 – 320.

Stern, A. (2000). Quantum-logical computer. In Stern, A. (Ed.), *Quantum Theoretic Machines*, pp. (495 – 544), North-Holland.

Tarucha, S., Honda, T., Austing, D. G., Tokura, Y., Muraki, K., Oosterkamp, T. H., et al. (1998). Electronic states in quantum dot atoms and molecules. *Physica E*, *3*, 112 – 120.

Tas, H., & Sahin, M. (2012). The electronic properties of a core/shell/well/shell spherical quantum dot with and without a hydrogenic impurity. *Journal of Applied Physics*, *111*, 083702.

Taseli, J. A., & Eid, R. (1996). Eigenvalues of the two-dimensional schrödinger equation with nonseparable potentials. *International Journal of Quantum Chemistry*, *59*, 183 – 201.

Temkin, H., Dolan, G. J., Panish, M. B., & Chu, S. N. G. (1987). Low-temperature photoluminescence from ingaas/inp quantum wires and boxes. *Applied Physics Letters*, *50*, 413 – 415.

Terhune, R. W., Maker, P. D., & Savage, J. M. (1692). Optical harmonic generation in calcite. *Physics Review Letters*, *8*, 404 – 406.

Terzis, A. F., & Baskoutas, S. (2005). Binding energy of donor states in a gaas quantum dot: effect of electric and magnetic field. *Journal of Physics: Conference Series*, *10*, 77 – 80.

Tran, K. T. M., & Nguyen, T. D. (2017). Lithography-based methods to manufacture biomaterials at small scales. *Journal of Science: Advanced Materials and Devices*, *2*, 1 – 14.

Triki, M., Elmaghraoui, D., Jaziri, S., & Bennaceur, R. (2010). The effects of geometrical parameters on carrier states and optical transitions in a quantum ring. *Solid State Communications*, *150*, 2197 – 2200.

Ungan, F., Bahar, M. K., Pal, S., & Mora-Ramos, M. E. (2020). Electron-related nonlinear optical properties of cylindrical quantum dot with the rosen-morse axial potential. *Communications in Theoretical Physics*, *72*, 075505.

Unlu, S., Karabulut, I., & Safak, H. (2006). Linear and nonlinear intersubband optical absorption coefficients and refractive index changes in a quantum box with finite confining potential. *Physica E*, *33*, 319 – 324.

Vahdani, M. R. K., & Rezaei, G. (2009). Linear and nonlinear optical properties of a hydrogenic donor in lens-shaped quantum dots. *Physics Letters A*, *373*, 3079 – 3084.

Vahdani, M. R. K., & Rezaei, G. (2010). Intersubband optical absorption coefficients and refractive index changes in a parabolic cylinder quantum dot. *Physics Letters A*, *374*, 637 – 643.

Varshni, Y. P. (2001a). Binding energy of a screened donor in a spherical quantum dot with a parabolic potential. *Superlattices and Microstructures*, *29*, 233 – 238.

Varshni, Y. P. (2001b). Effect of an intense laser field on donor impurities in spherical quantum dots. *Superlattices and Microstructures*, *30*, 45 – 52.

Vaseghi, B., Rezaei, G., & Sajadi, T. (2015). Optical properties of parabolic quantum dots with dressed impurity: Combined effects of pressure,temperature and laser intensity. *Physica B*, *456*, 171 – 175.

Vinasco, J. A., Radu, A., Restrepo, R. L., Morales, A. L., Mora-Ramos, M. E., & Duque, C. A. (2019). Magnetic field effects on intraband transitions in elliptically polarized laser-dressed quantum rings. *Optical Materials*, *91*, 309 – 320.

Wang, G. (2015). Highly efficient third-harmonic generation from resonant intersubband transitions in core/shells pherical quantum dots. *Optics Communications*, *355*, 1 – 5.

Wang, S., Kang, Y., & Li, X. (2014). Binding energy of the ground and first few excited states of hydrogenic donor impurity in a rectangular gaas quantum dot in the presence of electric field. *Superlattices and Microstructures*, *76*, 221 – 233.

Wang, W., Duppen, B. V., Donck, M. V., & Peeters, F. M. (2018). Magnetopolaron effect on shallow-impurity states in the presence of magnetic and intense terahertz laser fields in the faraday configuration. *Physical Review B*, *97*, 064108.

Wang, W., Duppen, B. V., & Peeters, F. M. (2019). Intense-terahertz-laser-modulated magnetopolaron effect on shallow-donor states in the presence of magnetic field in the voigt configuration. *Physical Review B*, *99*, 014114.

Wei, X., Wang, W., Xu, L., Zhang, S., & Tan, R. B. (2018). The effects of intense terahertz laser and magnetic fields on optical properties of a shallow impurity in semiconductors in the faraday configuration. *Physica Status Solidi B*, *255*, 1800211.

Wilson, J., & Hawkes, J. (1998). *Optoelectronics: An introduction*. (3rd ed.). Great Britain: Prentice Hall.

Xie, W. (2009). Nonlinear optical rectification of a hydrogenic impurity in a disc-like quantum dot. *Physica B*, *404*, 4142 – 4145.

Xie, W. (2010). Laser radiation effects on optical absorptions and refractive index in a quantum dot. *Optics Communications*, *283*, 3703 – 3706.

Xie, W. (2011a). Laser radiation effects on impurity states in a spherical quantum dot. *Physica E*, *43*, 1411 – 1414.

Xie, W. (2011b). Optical absorption and refractive index of an exciton quantum dot under intense laser radiation. *Physica E*, *93*, 1704 – 1707.

Xie, W. (2013a). Aharonov-bohm oscillation of photoionization cross section in a quantum ring with a repulsive scattering center. *Physics Letters A*, *377*, 903 – 906.

Xie, W. (2013b). The nonlinear optical rectification coefficient of quantum dots and rings with a repulsive scattering center. *Journal of Luminescence*, *143*, 27 – 30.

Xie, W. (2014). Aharonov-bohm oscillation of raman scattering in a quantum ring. *Physica B*, *438*, 88 – 90.

Xie, Y., Chu, W., & Duan, S. (2008). Magnetic-field-modulated terahertz absorption spectra of aquantum ring. *Applied Physics Letters*, *93*, 023104.

Xu, T., Yuan, L., & Fang, J. (2009). The laser-dressed potential binding energy of a hydrogenic impurity in a spherical quantum dot by the analytical transfer matrix method. *Physica B*, *404*, 3445 – 3447.

Yu, Y. B., & Wang, H. J. (2011). Third-harmonic generation in two-dimensional pseudodot system with an applied magnetic field. *Superlattices and Microstructures*, *50*, 252 – 260.

Yuan, J., Zhang, Y., Guo, X., Zhang, J., & Mon, H. (2015). The low-lying states and optical absorption properties of a hydrogenic impurity in a parabolic quantum dot modulation by applied electric field. *Physica E*, *68*, 232 – 238.

Yuan, J. H., Zhang, Y., Li, M., Wu, Z. H., & Mo, H. (2014). Hydrogenic impurity states in a parabolic quantum dot: hydrostatic pressure and electric field effects. *Superlattices and Microstructures*, *74*, 1 – 10.

Yun, K., Sheng, W., & Xianli, L. (2015). Electron energy states in a two-dimensional gaas quantum ring with hydrogenic donor impurity in the presence of magnetic field. *Journal of Semiconductors*, *36*, 032003.

Zeng, Z., Garoufalis, C. S., & Baskoutas, S. (2014). Linear and nonlinear optical susceptibilities in a laterally coupled quantum-dot-quantum-ring system. *Physics Letters A*, *378*, 2713 – 2718.

Zhang, Z., Guo, K., Chen, B., Wang, R., & Kang, M. (2009). Third-harmonic generation in cubical quantum dots. *Superlattices and Microstructures*, *46*, 672 – 678.

Zienkiewicz, O. C., Taylor, R. L., & Zhu, J. Z. (2005). *Finite element method: Its basis and fundamentals*. (6th ed.). Burlington: Butterworth-Heinemann.